Robotic Assembly of Weatherstrips

Bart Bastings
ID: 472619

D&C 2016.017

Master's thesis

Coach(es): dr. D. Kostić, Segula Technologies, TU/e
ing. P. Smulders, Segula Technologies

Supervisor: prof. dr. H. Nijmeijer, TU/e

Eindhoven University of Technology
Department of Mechanical Engineering
Dynamics & Control

Eindhoven, May, 2016

Contents

Chapter 1

Introduction

1.1 Background

The automotive industry is one of the largest users of industrial robots for manufacturing and assembly of cars. There are however still some areas in the process of car manufacturing where robots have not replaced human workers. One of these areas is the mounting of weatherstrip sealing onto the car chassis. This is generally performed by skillful workers that apply the weatherstrips manually, which means that the throughput of the entire manufacturing line is dependent on these workers. For successful sealing, the weatherstrip must be accurately applied on a substrate with contact forces that are high enough to guarantee good bonding. Both position and application force performances are gained by the worker trough training and years of experience. Hence, the process of weatherstrip application is very much sensitive to the availability of skilled workers which implies that the quality of the end product may vary from worker to worker. To ensure uniform quality and predictive throughput, the process of weatherstrip assembly should be automated by means of robots that mount the weatherstrips onto the car chassis.

To achieve robotized sealing, besides a good understanding of the robotics, it is eminent that the process of weatherstrip assembly itself is well understood and captured in the control design of the robot.

1.2 Problem Description

The process of weatherstrip assembly as being currently performed by human workers involves the positioning of the weatherstrip with respect to the substrate, aligning the weatherstrip with the edge of the mounting surface while keeping the correct tension force in the weatherstrip, and applying the correct force of contact between the weatherstrip and substrate. In Figure 1.1 the assembly of a weatherstrip into a car door opening is shown. In this specific case the weatherstrip has a special groove which slides over a dedicated flange in the car door opening. The weatherstrip needs to be positioned correctly to slide over the flange, and the application force needs to be high enough to correctly place the strip. An alternative assembly method is glueing the weatherstrip onto a substrate, such as an edge of a sunroof panel. In that case, the worker needs to position the weatherstrip correctly and apply the right mounting force for a given glue used to bond the weatherstrip onto the substrate. In this project the case where the weatherstrip is glued to a (curved) substrate is investigated, while the groove-flange system is not taken into consideration.

The problem of designing a robotic solution for automated weatherstrip sealing starts with the

Figure 1.1: Assembly of a weatherstrip into a car door opening.

identification of the process of weatherstrip assembly. A model of that process is needed to correctly predict the deformations in the weatherstrip during assembly and to correctly predict the application force on the bottom of the weatherstrip during assembly. Moreover, it has to be investigated how the rubber weatherstrip behaves under the application forces since rubber generally exhibits different behavior than more common engineering materials such as metals, ceramics and fiber reinforced composites. Therefore it is needed to qualify which rubber specific behaviors need to be captured in a model of the weatherstrip and which effects can safely be ignored. A model of the weatherstrip needs to be created in a suitable finite element software package capable of capturing all effects of importance for the weatherstrip assembly process. Simulations with this finite element model have to be performed to gain insight into the specific behavior of a rubber weatherstrip under application loads. It is generally not straightforward to include a general finite element model into a robot simulation, implemented, for instance, in the numerical software package Matlab. This means that the finite element model of the weatherstrip has to be converted into a form which is compatible with Matlab, moreover, it has to be compatible with the specific implementation of a robot in Matlab. A robot suited for the task of weatherstrip assembly has to be chosen and implemented as a model in Matlab. Both the robot model and the model of the weatherstrip have to be combined functionally to be able to simulate the entire weatherstrip assembly process. Control laws for the robot motion and for the force that the robot exerts onto the weatherstrip need to be developed, and the motion and application force performances of the controlled system have to be evaluated.

Consequently, the goals of this project can be stated as follows:

- Investigate rubber behavior and different rubber models
- Decide which rubber model to use and which rubber specific effects to include in the finite element model of the weatherstrip
- Create a finite element model of the weatherstrip
- Simulate the weatherstrip application process
- Create a model of the weatherstrip compatible with Matlab
- Design a 1 DOF force controller for the weatherstrip model, to evaluate its performance before implementing it on a six degree of freedom robot
- Implement in Matlab a model of a robot suitable for weatherstrip assembly

- Functionally combine models of the weatherstrip and the robot
- Design and implement control laws for the motion and application force of the robot
- Evaluate the performance of the robotized system

1.3 Thesis Outline

Chapter 2 is an overview of literature about robotic assembly and specific behaviors of rubber materials. It shows which mathematical models are available to model the behavior of the rubber weatherstrips and explains some of the more promising models in detail. Also some material effects specific to rubber are explained there. This knowledge about modeling of rubber and specific effects is needed to investigate the behavior of a weatherstrip and to create a model of the weatherstrip. In Chapter 3 various models are implemented and simulations are performed to investigate which properties of the rubber weatherstrip are of concern for the process of weatherstrip assembly. A nonlinear finite element model is used to simulate the behavior of the weatherstrip under assembly in Chapter 4. A linear finite element model is created and compared to the nonlinear model. This linear finite element model is used in Chapter 5, which is devoted to creation of a linear state-space model of the weatherstrip. In this chapter, the knowledge of rubber modeling, developed in previous chapters is used to create a model which is compatible with Matlab. This means that a relatively high dimensional finite element model of the weatherstrip, including non-linear material behavior, is used as a basis for a lower order and computationally lighter linear state-space model which still captures the most important properties of the weatherstrip. The design of the force control for the automated sealing process is the topic of Chapter 6. Here, a hybrid impedance force controller is designed for the one-dimensional case where the application force on the weatherstrip is controlled only in one degree of freedom. The designed controller is analyzed in the frequency domain by inspection of the characteristic transfer functions of the closed-loop system (e.g. sensitivity and complementary sensitivity), but also by servo control simulations in the time domain. In Chapter 7 the dynamics of a six degrees of freedom robot are modeled. Also, an inverse dynamics controller is designed which linearizes the inherently non-linear robot dynamics. The control law described in Chapter 6 can then be used to control the application force for this six degrees of freedom system. The performance of the entire system is analyzed in time domain servo simulations.

Chapter 2

Literature Overview

When designing a robot control scheme, for a robot applying weatherstrips to a surface, it is important to have a reliable model of the process under control. This process includes the weatherstrip, the surface, the interaction between these two, and finally the robot itself and its interaction with the weatherstrip. In this chapter investigations are conducted into the rubber behavior and its robotized assembly.

Since the automotive sector is on the forefront of automation with robotics, it is useful to investigate if applications similar to the one investigated in this project are documented in literature, and to use these as references.

Rubber behaves quite differently compared to more common engineering materials such as metals, ceramics or fiber composites. Hence, it is necessary to investigate all effects inherent to rubber materials and the corresponding models. Designing (dynamical) systems consisting of traditional engineering materials such as metals, is a common task and, as such, most engineers have some experience with it. They know from this experience what effects/behavior to expect, how to model it and what they can safely disregard. They also have a 'feel' for good or bad results when simulating such systems. In the case of applying rubber weatherstrips, this is different. In the domains of dynamics and control, rubber is not commonly considered, resulting in less experience and 'feel' for good or bad results. In this regard, it is wise to get a thorough understanding of the rubber material and its behavior before trying to simulate it. Moreover, usable models and realistic experimental data have to be researched in the existing literature. In this study the focus lies on EPDM rubber, since most automotive weatherstrips are made of EPDM sponge and dense rubber.

2.1 Robotic Assembly

The automotive industry is one among the first industries that takes advantage of robotic technologies, especially for assembly of various parts of a car and painting the car body. Some assembly techniques used in the automotive industry are for instance, spot welding, arc welding, laser beam welding, magnetic pulse welding, adhesive bonding, clinching and brazing [42]. All these techniques are used to join two rigid (mostly metal) car parts to each other.

In [52] the authors state that while robotic automation has played a key role in certain aspects of the car manufacturing process, such as welding, stamping, material handling and painting, final assembly of a car is mostly human labor. The same article reports that the car manufacturing company GM explores merits of an automatic robotic wheel and tire load system, which can attach a wheel to the car autonomously. In that article, some challenging tasks for future robotic automation are also mentioned, such as peg-in-hole assembly, contour match assembly, and surface match assembly.

Peg-in-hole assembly is a widely studied subject (for instance [16, 61, 66]) and refers to the robotic placement of one part into the hole of another part. According to [52], contour match assembly has been rarely studied; this sort of assembly refers to mating of parts along a contour of another part, for instance a weather strip along a car door. Surface match assembly refers to stacking 3D surfaces together, such as a carpet placed onto the vehicle floor. This type of assembly is not yet studied according to the article.

Figure 2.1: Assembly of a sunroof [29]

Mortimer [29] studied the modernization of UK car manufacturing and, in addition, gives some other examples of robotic assembly in the automotive sector. Of most interest is the application of the weatherstrip seal to the sunroof aperture in the car roof. This process is depicted in Figure 2.1. Here the sunroof system has to be perfectly aligned with the roof of the car to minimize wind roar. The weatherstrip seal is an integral part of this system and has to be perfectly aligned as well.

The machine depicted in Figure 2.1 applies the weatherstrip, places the sunroof and adjusts the glass alignment of the sunroof. An apparent limitation of this machine is the inflexibility in handling sunroofs of different shape.

While the aforementioned article [29] mentions automatic assembly of weatherstrips, the machine used is a tailored solution for a specific type of sunroof. An arm-type robot placing the weatherstrip would be a more flexible solution, since it may be reconfigured to assemble other type of sunroofs.

The topic of applying weatherstrip seals to automotive parts automatically with specialized machines or with more versatile robots is already described in patents, see for instance: [9, 39, 40, 41, 48]. These patents describe apparatus and methods for applying weatherstrips onto car door openings and robots for installing the weatherstrips into car doors or sunroof openings. However, a complete solution for automatic assembly of weatherstrips onto car parts does not seem to exist yet.

2.2 Rubber

Rubber exhibits material behavior that is quite different when compared to linear elastic materials, such as steel and aluminum. Figure 2.2 shows a typical stress-strain response for a rubber material.

The dotted line in this figure depicts the elastic response, which is nonlinear. The dashed line represents the behavior under slow loading and shows hysteresis. The solid line depicts behavior under fast loading and shows viscous friction effects.

In the next sections, the most common effects in rubber and ways to model them are discussed. These effects are grouped into three main categories: *nonlinear elasticity*, *visco-elasticity* and *inelastic behavior*.

Other useful resources to get a comprehensive review of the behavior and modeling of rubbers are for instance [47, 37].

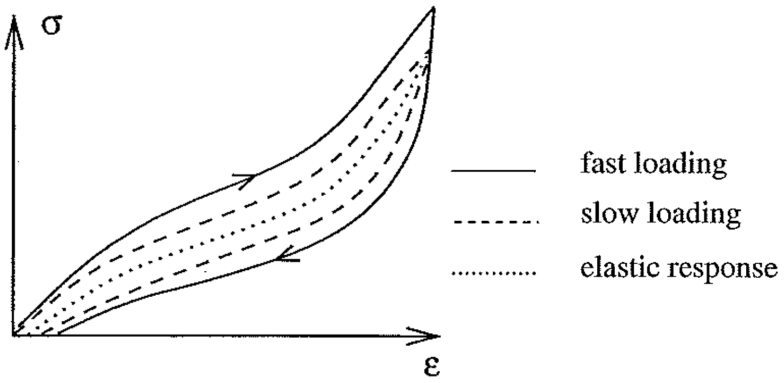

Figure 2.2: Typical rubber stress-strain response [47]

Some effects are purposely ignored because they are deemed to be of no importance to the process of weatherstrip assembly or can simply be circumvented. These effects include among others temperature dependency, ageing, chemical influences and moisture absorption.

2.2.1 Nonlinear Elasticity

The elastic stress-strain response of a rubber, as depicted with the dotted line in Figure 2.2, can be nonlinear and may cover very large deformations. In literature about nonlinear elastic material behavior, elongation is often characterized by the stretch ratio λ in stead of the strain ϵ used in linear elastic materials, a definition of λ is given in (2.1). A typical nonlinear elastic stress-stretch response of a hyperelastic material is shown in Figure 2.3. Materials that are characterized by such a large deformation elastic behavior, are called *hyper-elastic* [15, 24, 50].

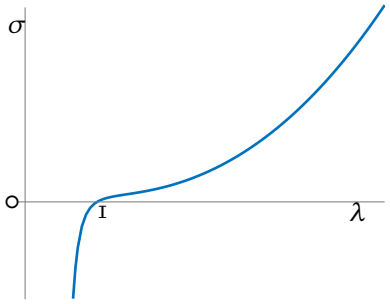

Figure 2.3: Typical nonlinear stretch-strain response

In Figure 2.3 the elongation factor is depicted by λ, and the stress is depicted by σ. An elongation

factor of 1 means no elongation. A hyperelastic response often starts with a certain slope, then softens (has a lower slope) at moderate elongation and stiffens (has a higher slope) at large elongations. These materials often are much stiffer in compression ($0 < \lambda < 1$) than in tension ($\lambda > 1$).

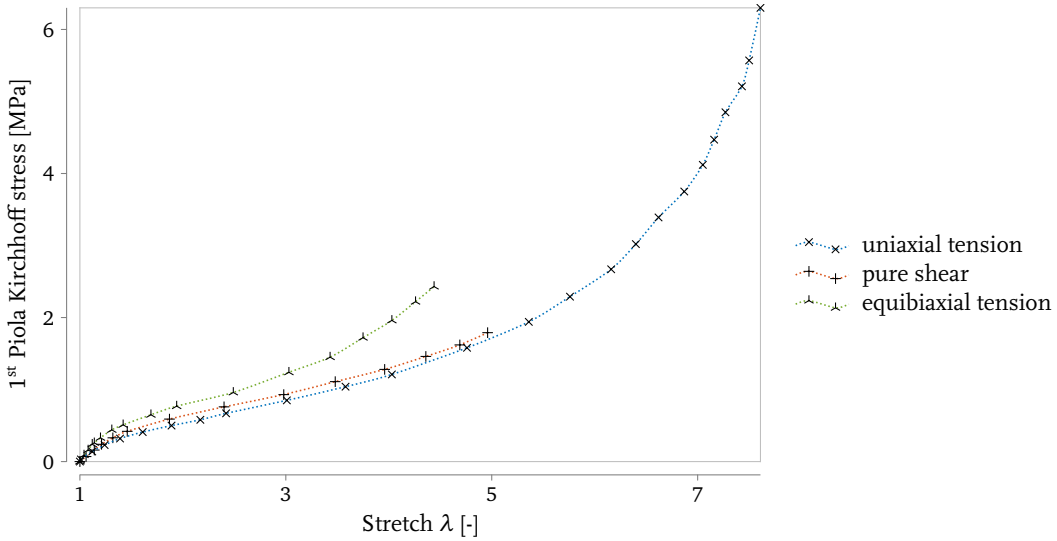

Figure 2.4: Experimental data for uniaxial tension, pure shear and equi-biaxial tension experiments, from [55].

An example of hyperelastic behavior can be found in [55], and is depicted in Figure 2.4. Here a vulcanized rubber specimen with a filler content of 8 % sulfur, is subjected to three experiments: uniaxial tension, pure shear and equi-biaxial tension. On the vertical axis the *first Piola Kirchhoff stress* is depicted, this is a measure for stress in the material which relates the force in the deformed state to the area in the undeformed state [50]. The nonlinear behavior and the stiffening at high elongation is clearly visible.

2.2.2 Nonlinear Elastic Models

Modeling nonlinear elastic or hyperelastic materials is more complicated than modeling linear elastic materials and, as such, a lot of different methods to model this behavior exist. An overview of different hyper-elastic models is given in [38, 50, 55], where [38, 55] also compare different models to experimental data.

The equations given in this section are for *one-dimensional* models (along one geometric axis), but the same principles hold for three-dimensions, where stress- and deformation tensors are used [15, 50].

Hyper-elastic behavior can be modeled with the use of the strain energy function $W(\lambda)$ and the *stretch ratio* λ. The latter is the ratio between the deformed length L and the original length L_0:

$$\lambda = \frac{L}{L_0} \tag{2.1}$$

The strain energy function $W(\lambda)$ is dependent on the stretch ratio and is used to calculate the stress σ in the material:

$$\sigma = \frac{\mathrm{d}W}{\mathrm{d}\lambda}\lambda \tag{2.2}$$

The majority of strain energy functions are written in terms of the principal stretch ratios $\lambda_1, \lambda_2, \lambda_3$, the strain invariants I_1, I_2, I_3 and the volume change factor J:

$$I_1 = \lambda_1^2 + \lambda_2^2 + \lambda_3^2 \tag{2.3}$$
$$I_2 = \lambda_1^2\lambda_2^2 + \lambda_2^2\lambda_3^2 + \lambda_3^2\lambda_1^2 \tag{2.4}$$
$$I_3 = \lambda_1^2\lambda_2^2\lambda_3^2 \qquad (I_3 = 1, \text{ for incompressible materials}) \tag{2.5}$$
$$J = \lambda_1\lambda_2\lambda_3 \qquad (J = 1, \text{ for incompressible materials}) \tag{2.6}$$

Most dense rubber materials are incompressible, which means that they have no volume change ($J = 1$) and their third strain invariant is equal to 1. Sponge rubbers, on the other hand, are compressible and need to be modeled with strain energy functions that take volume change into account.

In the next paragraphs, some hyper-elastic material models are considered.

Neo-Hookean

The Neo-Hookean [4, 15, 31, 50, 55] model is a one term model of the Rivlin type:

$$W = C_{10}(I_1 - 3) \tag{2.7}$$

This is the simplest hyper-elastic model and has C_{10} as the only material parameter.

This model is successfully used to model the deformation of weatherstrips with complex geometry in [56, 57, 58, 64]. Marckmann and Verron conclude that for small strain (up to 50 %), the Neo-Hookean model should be chosen over all other models because it is able to predict material response for different types of loading conditions [38].

Mooney-Rivlin

The Mooney-Rivlin [4, 15, 22, 31, 50, 55] model has two terms and two material parameters, C_{10} and C_{01}:

$$W = C_{10}(I_1 - 3) + C_{01}(I_2 - 3) \tag{2.8}$$

This model can be used for strains up to 100 %, but it is not well suited for modeling compression behavior [6].

This model is one of several ones used in [22] to model the static compression of an EPDM weatherstrip seal shaped as a hollow tube. The authors of [22] find that an Arruda-Boyce model has better agreement with their experimental data than a Mooney-Rivlin model.

James-Green-Simpson

The James-Green-Simpson model [50] is also a model of the Rivlin type, it has five material parameters and can be used for strains up to 200 % [6]:

$$W = C_{10}(I_1 - 3) + C_{01}(I_2 - 3) + C_{11}(I_1 - 3)(I_2 - 3) + C_{20}(I_1 - 3)^2 + C_{30}(I_1 - 3)^3 \tag{2.9}$$

In [2, 63] this model is used to simulate an EPDM weatherstrip with complex geometry under compression loading with a finite element method. A comparison between a linear material model and the James-Green-Simpson model reveals large differences in behavior (up to 200 %).

Arruda-Boyce

The Arruda-Boyce model is also known as the eight-chain model [6, 4, 10, 55] and has two material parameters, μ and λ_L:

$$W = \mu \sum_{i=1}^{5} \frac{C_i}{\lambda_L^{2i-2}} (I_1^i - 3^i) \tag{2.10}$$

The constants C_i are defined as [6, 10, 22]:

$$C_1 = \frac{1}{2}, C_2 = \frac{1}{20}, C_3 = \frac{11}{1050}, C_4 = \frac{19}{7050}, C_5 = \frac{519}{673750}$$

In [37] it is claimed that this model provides sufficient accuracy for multiple deformation modes (tensile, compression, uniaxial, biaxial), when configured with standard tensile test data. The Arruda-Boyce model is used to simulate the compression loads of an EPDM weatherstrip [22], and it shows the best agreement with experimental data with respect to other used models.

Ogden

The Ogden model [4, 15, 22, 25, 50, 55] is based on the stretch ratios directly, and has two material parameters per term, μ_i and α_i:

$$W = \sum_{i=1}^{N} \frac{\mu_i}{\alpha_i} (\lambda_1^{\alpha_i} + \lambda_2^{\alpha_i} + \lambda_3^{\alpha_i} - 3) \tag{2.11}$$

This model is applicable to strains of up to 700 % [6]. It is used in [18] to model the behavior of EPDM rubber with different loading rates and it is used in [64] to model weatherstrips made of TPE and EPDM rubber.

General Remarks on Nonlinear Elastic Models

It has to be noted that all material models have to be fitted to experimental data before they can be used. A model is only usable if it can reproduce experimental data to a certain accuracy. Also, it is desirable that a model has as few parameters as possible, which makes the fitting procedure easier. Finally, an ideal model would be able to predict behavior outside the fitted data set. This is important to realize, because for hyperelastic models this is almost never the case. To illustrate this, see Figure 2.5 from [55]. In this figure, on the left-hand side, an Ogden 3 parameter model is fitted to equi-biaxial tension data (red line). Uniaxial tension and pure shear experiments are simulated with this model and shown as black and blue lines, respectively. In the figure on the right-hand side, the model is fitted to the pure shear data (blue line), and simulated for the uniaxial tension (black line) and equi-biaxial tension (red line). From these figures it is clear that these fitted models represent the fitted data quite good, but behave poorly for data outside the fitted set. This is the case for all models considered in [55].

Another example where different fitted models are compared is given in [64], where a Mooney-Rivlin model is fitted to experimental data from an EPDM specimen with three different strain ranges: 10 %, 20 % and 30 %. Three simulations with these models are compared and shown in Figure 2.6. In this figure, the top curve depicts the model fitted to data with a range of 10 % strain, and the bottom curve is fitted to data with a 30 % strain range. The difference at a stretch of $\lambda = 1$ is more than 40 %.

The models of weatherstrip behavior in this project are used to predict the behavior of the weatherstrip under certain loading conditions, while the models are based on experimental material

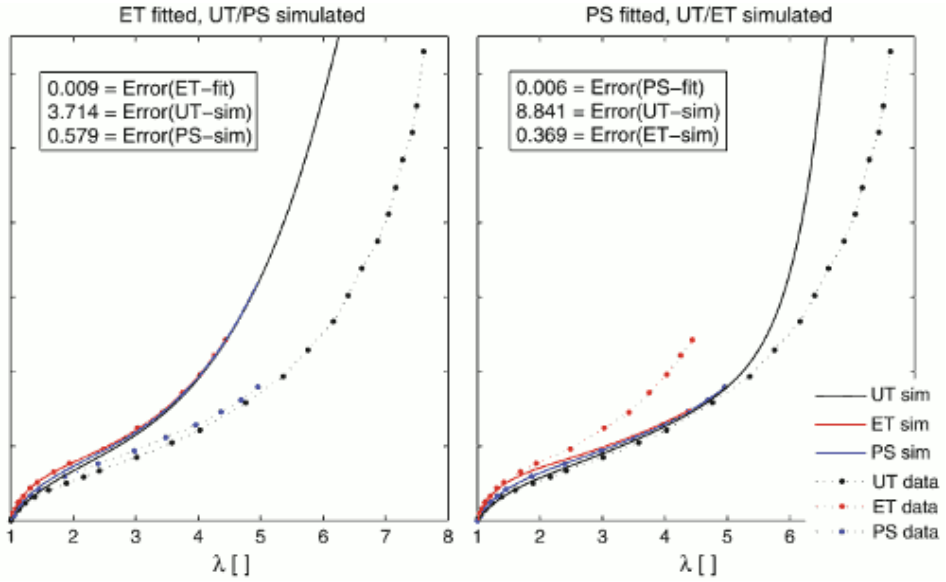

Figure 2.5: Ogden 3 parameter model fitted to data [55]. Left: model is fitted to equi-biaxial tension data, right: model is fitted to pure shear data.

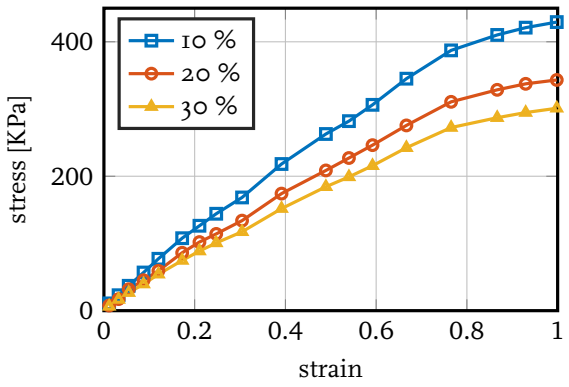

Figure 2.6: Comparison between Mooney-Rivlin models fitted to three different data sets [64]

data extracted from a limited set of experiments and loading conditions. The above examples show that besides a good material model, it is crucial to have experimental data that is expected to reasonably represent the simulation that has to be performed.

2.2.3 Viscoelasticity

Besides the nonlinear elastic phenomena, rubbers also exhibits *viscoelastic* behavior. This behavior is characterized by time dependency, due to which, the relation between stress and strain is a function of loading rate.

An overview of some important viscoelastic effects are given in the following paragraphs. In Section 2.2.4, some material models are discussed that incorporate these viscoelastic effects.

Relaxation

When a viscoelastic material is subject to a step change in strain, the stress also exhibits a sudden jump but then decreases in time to a lower steady-state value. This effect is called *(stress)-relaxation* [7, 8, 12, 22, 24, 34, 50] and is depicted in Figure 2.7. On the left-hand side in this figure, the strain input

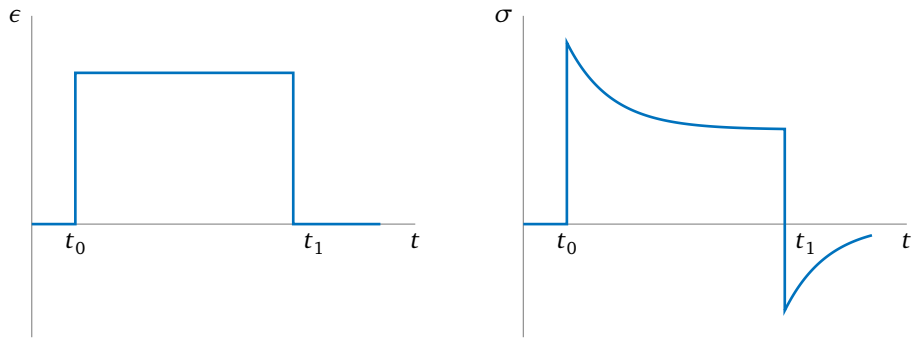

Figure 2.7: Stress relaxation to a strain-step input

is shown and on the right-hand side the resulting stress is depicted. After the initial spike in the stress, when the strain is kept constant the stress decreases (relaxes) with time. A result of this is that only a part of the deformation energy is stored as elastic energy which can be restored after deformation. The resulting deformation energy is dissipated and can not be restored, this is the decaying part of the stress curve in Figure 2.7.

An example of this behavior is given in [22], where a stress relaxation experiment on an EPDM weatherstrip is conducted (the results are shown in Figure 2.8). Here, a small part of a weatherstrip is indented 4 mm with an automatic indentation device and indentation force is measured. This force relaxes more than 10 % over a period of 20 seconds. This indicates that the effect of stress-relaxation makes it difficult to estimate the strain of the material given the stress and vice versa.

The result of the relaxation experiment shown in Figure 2.8 indicates that it is important to investigate the effect of relaxation on automatic application of weatherstrips, which is the main topic of this research project. Relaxation itself hinders the estimation of strain from force measurements and, more importantly, relaxation is coupled to *creep* (see next section) which has to be minimized for a satisfying result.

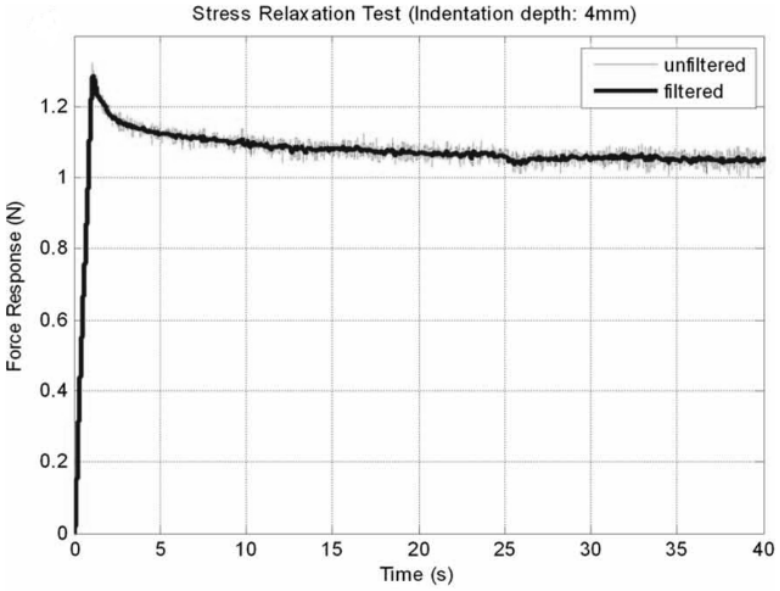

Figure 2.8: Stress relaxation in an EPDM weatherstrip [22]

Creep

Another viscoelastic effect of rubbers is creep [24, 50], which is an increasing strain on a steady stress state. This effect is depicted in Figure 2.9. Creep and stress-relaxation depend on the same mechanics and, as such, are similar to each other.

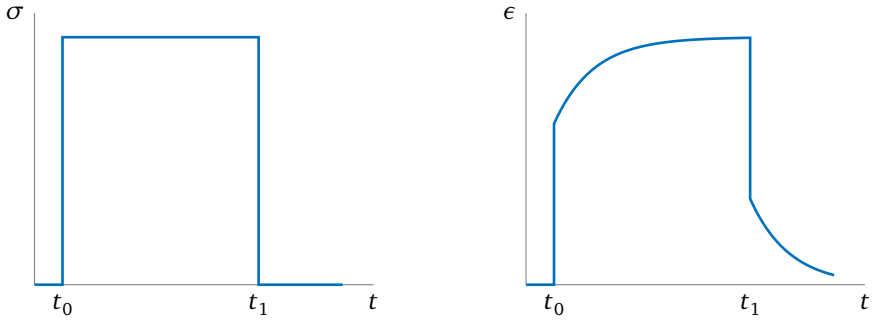

Figure 2.9: Creep behavior on stress-step input

While creep is often explained as increasing strain while the stress is kept steady, it can also have the opposite effect. When a weatherstrip is placed around a contour with a certain strain and internal stress, the material may start to creep and as a result the strain and internal stress decreases with time. In the case of a weatherstrip applied around a closed contour, a gap gets formed as soon as the material starts to creep. Figure 2.8 shows a weatherstrip which relaxes more than 10 %; this may indicate that the creep in this weatherstrip could be of the same order and has to be investigated.

Hysteresis and Damping

In Figures 2.7 and 2.9, relaxation and creep are shown that result from a step input in strain and stress, respectively. When a viscoelastic material undergoes harmonic excitation, the response shows hysteresis [24, 46, 50]. This hysteresis is a result of the same mechanics as relaxation and creep. When a harmonic stress input is applied, the resulting strain lags behind and vice versa. An example of this behavior is shown in Figure 2.10.

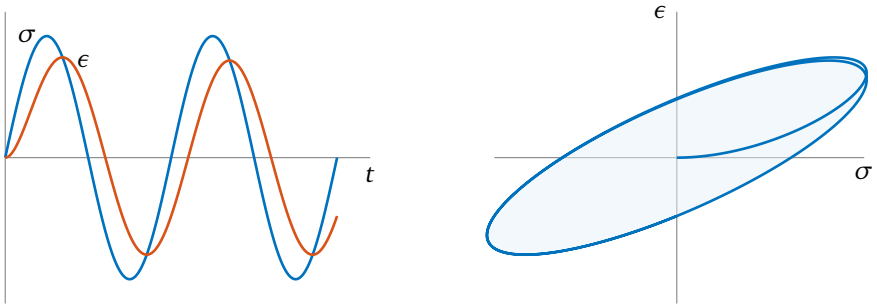

Figure 2.10: Hysteresis from sinusoidal stress input

In this figure, on the left-hand side, both stress and strain are plotted versus time, on the right-hand side a hysteresis loop (stress versus strain) is plotted. The area within the closed curve is hysteresis and amounts to the dissipated energy. This hysteresis is also called material damping, and is a result of the out of phase behavior of the harmonic response. The amount of phase lag ζ between the input stress and the output strain is a measure of the amount of hysteresis/damping; the higher the phase lag, the wider the hysteresis loop is, and the damping is higher.

The process of placing a weatherstrip around a contour does not involve harmonic excitation, so the hysteresis and damping due to harmonic excitation are not an important effect in this regard.

Rate-Dependent Response

When a viscoelastic material is subject to loading with a slow rate, it behaves differently compared to a fast loading case; in other words, its response is rate dependent [7, 18, 43, 45, 50]. This is exemplified in Figure 2.11 where lines are drawn for the instantaneous response σ_{inst}, the equilibrium response σ_{eq} and the viscous response σ_{visc}. The instantaneous response is the response that would be measured when the material is loaded at an infinite rate. The equilibrium response on the other hand would be measured when the material is infinitely slow loaded. An actual case, with a realistically achievable loading rate, would be the viscous response line. This line can be anywhere in the shaded area between the instantaneous and the equilibrium responses.

When an experiment (for instance, a tensile test) is carried out on a rubber specimen with a loading rate that is high enough, the response initially moves along the instantaneous response line. When the loading is stopped and the stress is kept at a constant level, the response will move horizontally towards the equilibrium response; this is creep behavior. When strain would be kept constant the response would move vertically downwards to the equilibrium line, this indicates relaxation.

Figure 2.11 indicates that the stiffness or modulus (σ/ϵ) of the material is dependent on the loading rate, which in case of harmonic excitation leads to frequency dependency. A fast loading results in a stiffer (higher modulus) response than a slow loading, so a higher frequency harmonic excitation results in a stiffer harmonic response. For a phase lag between the input and output of a harmonic excitation, such as shown in Figure 2.10, this is a little bit more complex. The phase lag ζ,

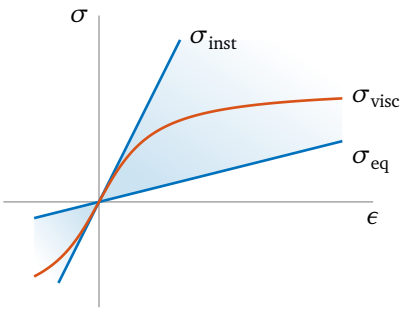

Figure 2.11: Instantaneous, equilibrium and viscoelastic responses

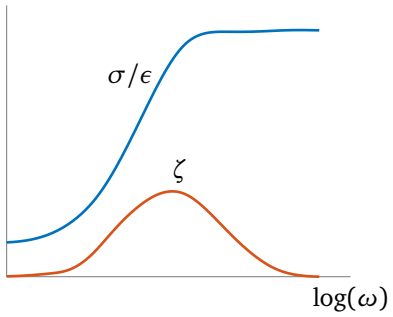

Figure 2.12: Dynamic modulus and damping

or hysteresis/damping, is low for low frequencies, grows for intermediate frequencies and decreases again for high frequencies. This is shown in Figure 2.12.

It is already reasoned that in the process of assembling weatherstrips, harmonic effects are likely not important. In [43], the authors investigate the frequency dependent stiffness of automotive weatherstrip seals. One of their experimental results is shown in Figure 2.13. In this figure, the curve labeled with 1 has the highest static deformation, while the curve labeled with 5 has the lowest static deformation. In the case of low deformation level, the stiffness increases linearly with frequency but only with a limited magnitude. This indicates that when a weatherstrip is excited within a small frequency range, or even with a static loading rate, the frequency dependency is limited. For the process of weatherstrip assembly, this means that it is safe to assume that the frequency dependent behavior is of negligible.

The effects of loading rate on the stress-stretch behavior of EPDM rubber weatherstrips are investigated in [18]. In Figure 2.14, the results of experiments with a low loading rate ($0.4\,s^{-1}$) are compared to experiments with a high loading rate ($2800\,s^{-1}$ and $3200\,s^{-1}$). First thing to notice is that the slow loading curve shows a lot of hysteresis, but not of the kind discussed above. The hysteresis encountered in this example is caused by the so called *Mullins effect*, a form of plastic deformation treated in Section 2.2.5. For stretch ratios higher than 1.1, the low and high loading rate curves are diverging, the high loading rate curve has a much higher stiffness than the low loading rate curve. From this figure it can be concluded that for high stretch ratios the loading rate has an important influence on the behavior of the material. For low stretch ratios the curves look quite similar, so this effect is not as pronounced in that case. It has to be investigated if this effect has to be taken into account for the weatherstrip assembly process.

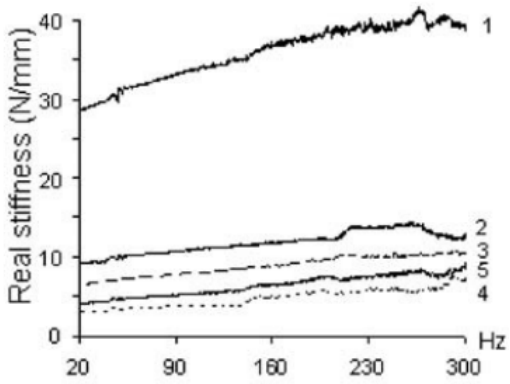

Figure 2.13: Dynamic stiffness [43]

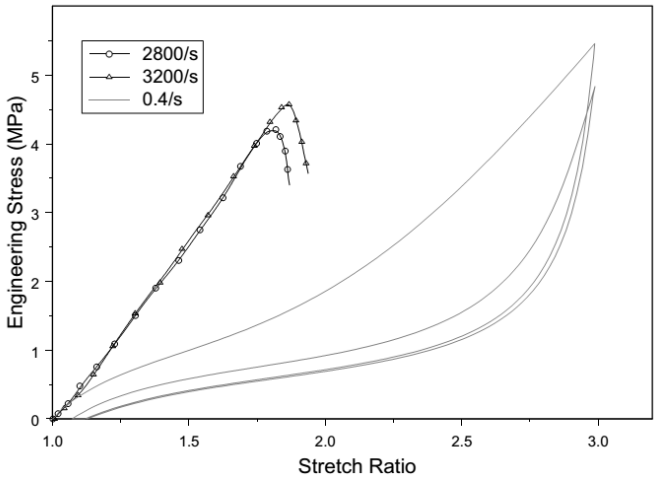

Figure 2.14: Loading rate effects [18]

2.2.4 Viscoelastic Models

Viscoelastic behavior is often modeled by means of lumped spring-damper models [8, 12, 22, 24, 43, 45, 46, 50]. Other models are the Prony series approach [12, 22, 25, 30, 46, 53], the fractional derivative modeling [46, 49] and the modified power law [46].

Standard solid model

The simplest model which captures the creep and relaxation behavior is the standard solid model, depicted in Figure 2.15. This model involves a spring in parallel with a serial spring-damper combination, and can be described with the following differential equation:

$$\dot{\sigma} + \frac{E}{\eta}\sigma = (E + E_\infty)\dot{\epsilon} + \frac{EE_\infty}{\eta}\epsilon \tag{2.12}$$

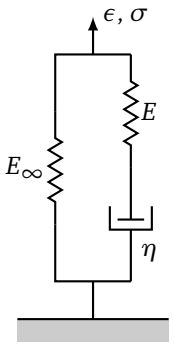

Figure 2.15: Standard solid model

This model contains three material parameters, the stiffness at equilibrium condition E_∞, the extra stiffness E and the damper viscosity coefficient η. When this model is subject to a high loading rate, the damper acts stiff and the overall stiffness of the model is governed by $E_\infty + E$. When the model is subject to a low loading rate, the damper yields with the same rate and the stiffness is purely determined by E_∞.

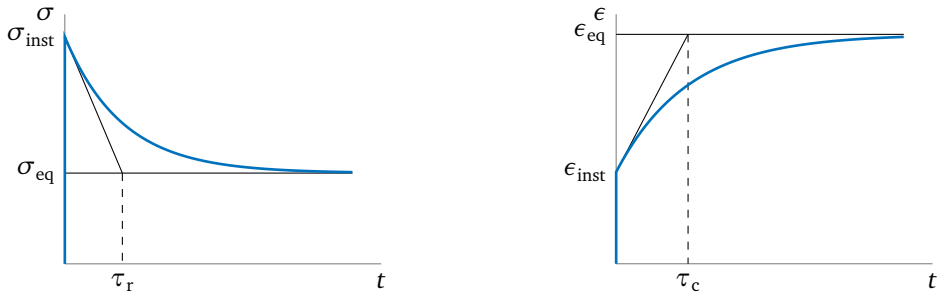

Figure 2.16: Relaxation (left-hand side) and creep (right-hand side) determined by the standard solid model

In Figure 2.16, relaxation and creep that are modeled with the standard solid model are shown. It shows that the model describes relaxation and creep with exponential functions of time. Time

constants τ_r and τ_c are given by:

$$\tau_r = \frac{\eta}{E} \tag{2.13}$$

$$\tau_c = \frac{\eta}{E_\infty} + \frac{\eta}{E} \tag{2.14}$$

The total time dependent modulus of this model is given by:

$$E(t) = E_\infty + Ee^{\frac{-t}{\tau_r}} \tag{2.15}$$

This model can also be used to model harmonic hysteresis and damping. However, it is not suitable for modeling frequency dependent behavior, since the material parameters are constants and not frequency dependent. Also, the creep and relaxation behaviors are determined by only one specific time constant for each. This limits the validity of the model within a narrow frequency band. Another serious limitation is that it is not capable of describing hyperelastic material behavior.

Generalized Maxwell model

To overcome the limitation of the standard solid model in terms of representing the relaxation and creep with a single time constant, an extension is needed which includes more spring damper combinations. This extension is called the generalized Maxwell model and is shown in Figure 2.17.

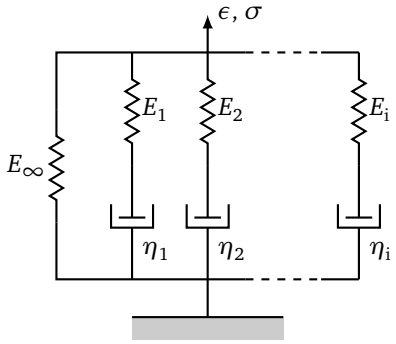

Figure 2.17: Generalized Maxwell model

The time dependent modulus of this model is given by:

$$E(t) = E_\infty + \sum_{i=1}^{m} E_i e^{\frac{-t}{\tau_i}} \tag{2.16}$$

$$\tau_i = \frac{\eta_i}{E_i} \tag{2.17}$$

This model describes relaxation, creep and harmonic hysteresis in a wide frequency range, but is limited to linear viscoelastic behavior only.

Prony series

The Prony series approach [4, 25, 30, 46, 53] is a method which resembles the generalized Maxwell model. It can represent multiple sets of parallel spring damper combinations, and has the advantage

that it can also include hyperelasticity. The general form of this model is [30]:

$$g(t) = g_\infty + \sum_{i=1}^{m} g_i e^{\frac{-t}{\tau_i}} \tag{2.18}$$

where τ_i is a time constant, while g_∞ and g_i are constants that specify the contribution of the equilibrium and the viscous responses, respectively. When applied to a simple linear viscoelastic material, it can be rewritten to equation (2.16). It is also possible to include hyperelastic material models into this form; an example for the Mooney-Rivlin model (equation (2.8)) would be:

$$W(t) = C_{10}(t)(I_1 - 3) + C_{01}(t)(I_2 - 3) \tag{2.19}$$

$$C_{10}(t) = C_{10}^{\infty} + \sum_{i=1}^{m} C_{10}^{i} e^{\frac{-t}{\tau_i}} \tag{2.20}$$

$$C_{01}(t) = C_{01}^{\infty} + \sum_{i=1}^{m} C_{01}^{i} e^{\frac{-t}{\tau_i}} \tag{2.21}$$

Here the material parameters C_{10} and C_{01} are functions of time instead of constant coefficients for the invariants I_1 and I_2 like in the original Mooney-Rivlin model of equation (2.8). The new material parameters for this model are C_{10}^{∞} and C_{01}^{∞} for the equilibrium response, and C_{10}^{i} and C_{01}^{i} for the viscous response. The latter two have to be determined for all m terms of the Prony series, where m denotes the total number of spring damper combinations modeled. Each Prony series term represents a standard solid model with certain time constants, so each extra term added is equivalent to adding another spring-damper-spring combination to the model. This enables modeling the viscous behavior over a wide frequency range.

Some finite element software packages used to model rubber material behavior use the Prony series to append the computation of the material stress σ, which enables the combination of the Prony series with an arbitrary hyperelastic model to create a visco-hyperelastic model:

$$\boldsymbol{P} = \int_0^t \left(\alpha_\infty + \sum_{i=1}^{m} \alpha_i e^{-\frac{t-\tau}{\tau_i}} \right) 2 \frac{\mathrm{d}}{\mathrm{d}\tau} \frac{\partial W}{\partial \boldsymbol{C}} \mathrm{d}\tau \tag{2.22}$$

Here, $\boldsymbol{P}$ is the *second Piola-Kirchhoff stress* for the three dimensional case which is a stress measure that relates forces in the undeformed state to areas in the undeformed state [50]. $\boldsymbol{C}$ is the *right Cauchy-Green deformation tensor*, which is a measure of deformation [50], comparable to the stretch ratio in (2.2).

In [22] the Prony series approach is used with an Arruda-Boyce hyperelastic model to describe the dynamics of automotive weatherstrips with a finite element method. A stress relaxation experiment is conducted to estimate the parameters for the Prony series, these parameters are used in a finite element simulation of car door dynamics.

The Prony series approach can model relaxation, creep and harmonic hysteresis over a wide range of frequencies with hyperelastic elasticity. This method is available in most finite element programs. Because of this, it seems to be the best choice to model the weatherstrip assembly process.

Fractional derivatives and power law methods

In [46] the fractional derivative model and the power law method are mentioned. Both methods are somewhat similar to the Prony series approach, but are not available in most standard finite element programs which makes them less attractive.

The fractional derivative model is given by:

$$\sigma + b\frac{\mathrm{d}^{\alpha}\sigma}{\mathrm{d}t^{\alpha}} = E_0\epsilon + E_1\frac{\mathrm{d}^{\alpha}\epsilon}{\mathrm{d}t^{\alpha}} \tag{2.23}$$

where b, E_0 and E_1 are material parameters and $0 \leq \alpha \leq 1$. For more information see [49].

The power law method is explained in [65] and is given by:

$$E(t) = E_e + \frac{E_g - E_e}{(1 + t/\rho)^n} \tag{2.24}$$

where E_e and E_g are material parameters, ρ is a relaxation time and n is a power.

2.2.5 Inelastic Behavior

Viscoelasticity is characterized by rate dependent energy loss (hysteresis), another effect often seen in rubbers is hysteresis due to quasi-static loading and plastic deformation. The most prominent of these inelastic effects are the Mullins effect and the Payne effect, both are explained below.

Mullins effect

When an unstretched rubber sample is loaded, its initial material parameters change due to the loading. After a few loading cycles this behavior stabilizes, so the material parameters are constant again. When the material is loaded to a higher stretch than before, the material parameters change again. This softening behavior is known as the Mullins effect [13, 17, 18, 19, 21, 34, 44, 53]. Figure 2.18

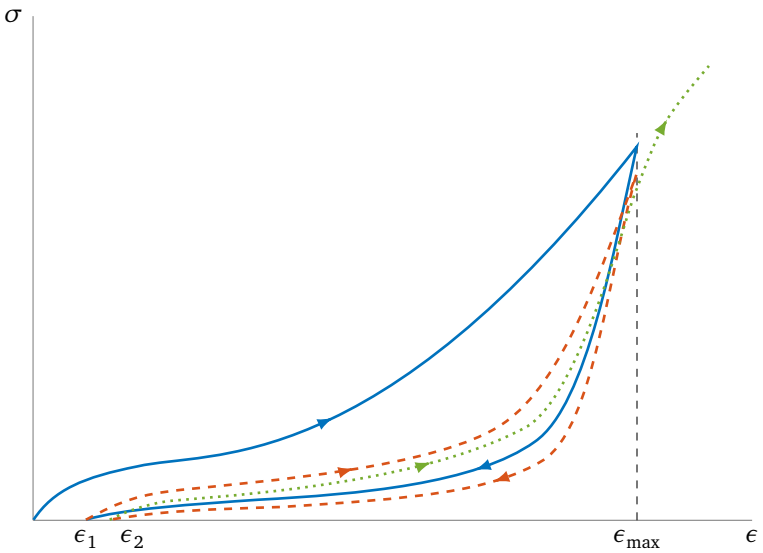

Figure 2.18: Typical Mullins behavior: first loading curve is depicted with the blue line, the second loading curve is depicted with the dashed red line and the third loading curve is depicted with the dotted green line.

shows typical Mullins behavior, the blue line depicts the first loading and unloading to a maximum strain of ϵ_{max}. After the first loading curve there remains a small amount of strain (which is denoted by ϵ_1). The second loading curve (red line) traverses a new path, somewhere above the first unloading curve to the same maximum strain ϵ_{max}. The second unloading curve lies somewhat below the first

unloading curve. This goes on until the loading curve stabilizes after 5 to 10 cycles. In the figure, the third loading curve is subjected to a higher maximum strain compared to the first two loading curves. After the point of previous maximum strain (denoted with ϵ_{max} in Figure 2.18) the curve continues the (projected) path of the first curve before it returned on its unloading curve.

The difference between the loading and unloading curves, and also the difference between subsequent loading cases, is a form of softening. The material behaves less stiff in subsequent loading cycles. This means that the material parameters are dependent on strain history. Also, the hysteresis that occurs is not due to fast loading, and occurs even at steady state loading. The Mullins effect is probably due to rearranging or damaging internal networks, but there seems to be no generally accepted theory on the cause of this effect [21].

Another result of the Mullins effect is the strain set at zero stress after a complete loading cycle, for instance ϵ_1 in Figure 2.18, after the first loading cycle. In [18] the authors report that this strain set is not recoverable, which is experimentally shown by leaving stretched specimen of EPDM rubber unloaded for a week. However, [20] reports partial recovery for EPDM specimen after a 20 min stress-free period.

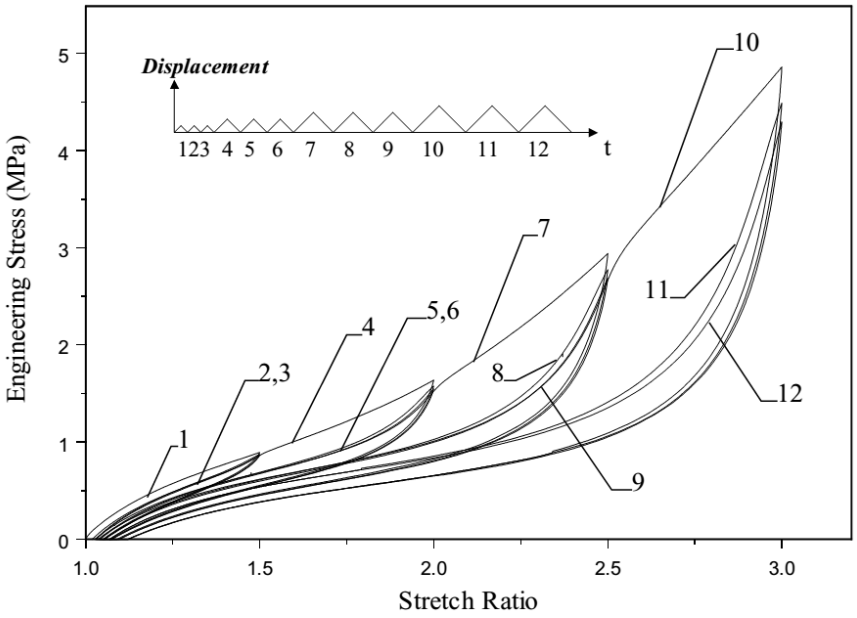

Figure 2.19: Mullins effect measured by [18]

In Figure 2.19, the result of a stress-stretch experiment on EPDM rubber is shown; this experiment is described in [18]. In the inset the loading curve is shown. The loading strain increases every three cycles. By inspection of this figure, a few things can be observed. First, the behavior can become severely nonlinear (for instance cycle 12). Secondly, the hysteresis can become quite big, especially for 'fresh' loading curves that are subject to a new maximum strain. A third observation is that the amount of hysteresis or softening seems to be larger for larger strains, that is, the loading curves look 'fatter' for higher maximum achieved strain. Finally, it can be seen that the strain set for the last cycle is around 0.15 ($\lambda = 1.15$), which is almost 10 % of the maximum strain of $\epsilon = 2$. For smaller loading curves it is hard to read a reliable number.

The authors of [64] performed uniaxial and equi-biaxial tension tests on EPDM rubber, their results are shown in Figure 2.20. These are the stabilized loading curves after five repetitions. In these

figures it can be seen that in the zero stress state some strain remains; the residual strain or strain set. In the uniaxial case, depicted on the left of Figure 2.20, the curve with the smallest maximum strain (10 %) has a strain set of 1.7 %. This is 17 % of the maximum reached strain, indicating that even for small strains this effect can be significant. For the equi-biaxial case, depicted on the right of Figure 2.20, the results are similar. Here a residual strain set of 2 % remains from a maximum reached strain of 10 %.

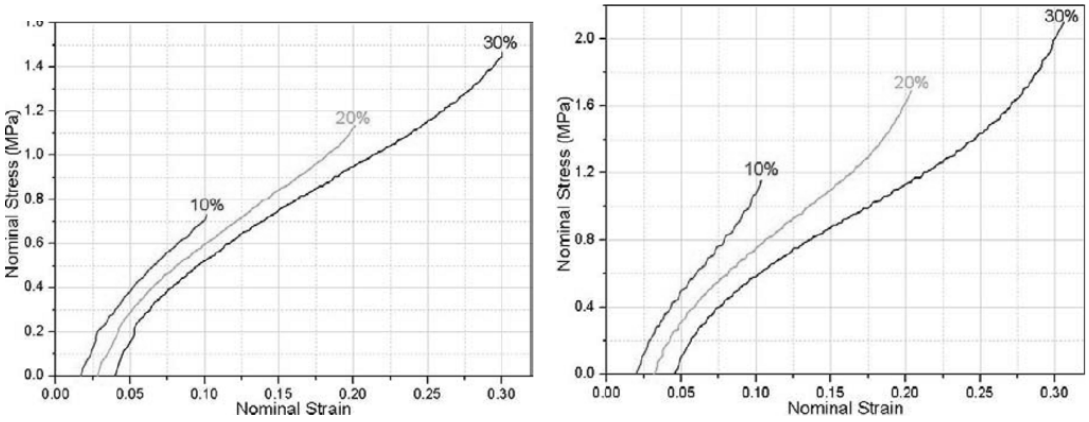

Figure 2.20: Stabilized loading curves (after five repetitions) for uniaxial tension tests (left), and equi-biaxial tension tests (right) [64].

Another experiment on permanent strain set is performed in [23], where specimens of rubber with different filling degree are submitted to cyclical loading and there permanent strain measured. The results are shown in Figure 2.21. The bottom line depicts a rubber with a filler content of 1 phr, the middle curve has a filler content of 20 phr, and the top curve has a filler content of 60 phr. The authors note that a filler content of 1 phr has no effect on mechanical properties, and can therefore be considered as unfilled. All loading cycles reach a maximum stretch of $\lambda = 3$. From this figure it is clear that even for unfilled rubbers the permanent strain becomes significant. It also confirms the findings from Figure 2.20 that small stretches result in relatively big permanent strain set; in the order of magnitude of a few percent. This means that a rubber loaded to a certain extent and thereafter unloaded to a zero stress state, can still be elongated a few percent.

This permanent strain set has serious implications to the weatherstrip assembly process; a remaining elongation of a weatherstrip may result in difficulties connecting the ends of the weatherstrip around a closed contour. There does not seem to be consensus in literature whether this strain set is (partly) recoverable or not, so creep resulting from this cannot be excluded.

Payne effect

Besides frequency dependent behavior when excited harmonically, a rubber does also exhibit amplitude dependent behavior. This effect is named the Payne effect [26, 33, 60]. In Figure 2.22 the modulus (σ/ϵ) and damping (ζ) are plotted against the (logarithmic) strain amplitude ϵ_A for a harmonic excitation. Similar to the rate (frequency) dependent response shown in Figure 2.12, the modulus and damping change over a wide range. According to [45] the amplitude dependent effects in rubber are more prominent than frequency dependent effects.

While this amplitude dependent effect is considered to be important for a wide range of applications such as shock absorbers, in the case of non-harmonic excitation such as the assembly of weatherstrips, it is assumed to be negligible.

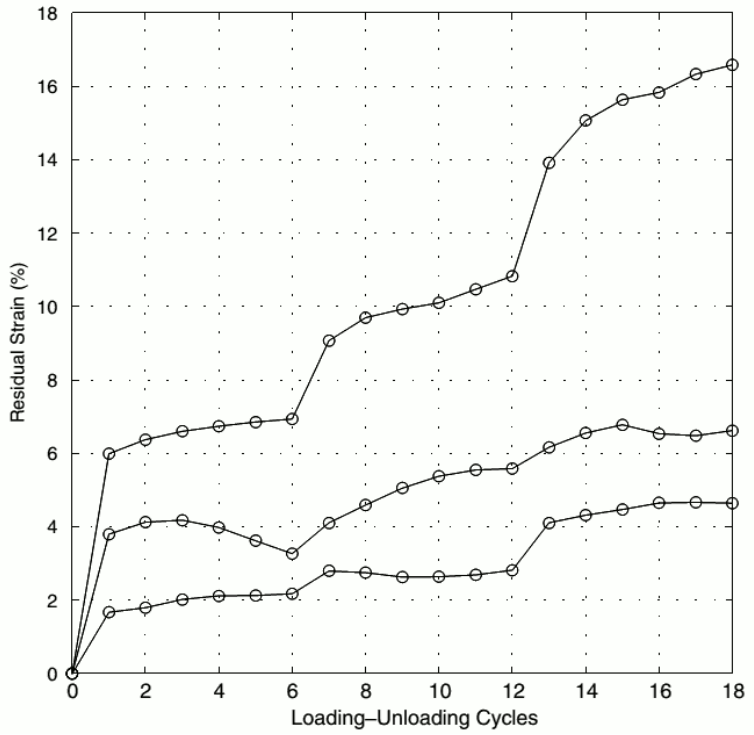

Figure 2.21: Permanent strain set after a number of loading cycles. Cycles 1 to 6 have a maximum stretch of $\lambda_m = 1.5$, cycles 7 to 12 of $\lambda_m = 2$ and cycles 13 to 18 of $\lambda_m = 3$ [23].

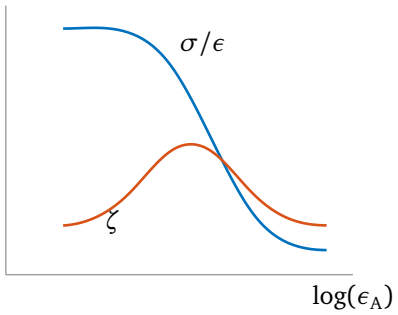

Figure 2.22: Typical Payne effect

2.2.6 Inelastic Models

The authors of [21] give a comprehensive overview of models that capture the Mullins effect. They classify two types of models: phenomenological and physically motivated models. It seems that no model can be considered as the most prominent one. In principle, all models are fairly accurate estimates. One of these models is used for modeling automotive weatherstrips [18] and is available in the finite element program ANSYS [5]. This is the so called Ogden-Roxburgh model, which is explained below.

The amplitude dependent Payne effect is assumed to be negligible for the process of weatherstrip assembly, so only one model is investigated: the generalized elasto-plastic model.

Ogden-Roxburgh model

The Ogden-Roxburgh model [44] can only partly describe the Mullins effect. This model assumes an idealized Mullins effect, which means that subsequent unloading and loading cycles traverse the same path. In Figure 2.18 this would mean that the second loading curve would traverse the first unloading curve in reverse. A second shortcoming of this model is the lack of permanent strain set, since all curves computed using this model return to the origin.

The idea behind the model is to introduce a damage variable η which depends on loading history. This damage variable is used to alter the energy function $W(\lambda_1, \lambda_2)$ as defined by the used hyperelastic material model (for instance the Mooney-Rivlin model defined in equation (2.8)), and define a *pseudo-energy function* $W(\lambda_1, \lambda_2, \eta)$. This pseudo-energy function differs from the original energy function since it not only depends on the strain invariants I_1, I_2 and I_3 or the stretches λ_1, λ_2 and λ_3, but also on the damage variable η. This damage variable can be used to lower the value of the pseudo energy function, and as a result, mimic damage behavior. Here it is assumed that the material is incompressible ($\lambda_1\lambda_2\lambda_3 = 1$) and as a result, there are only two independent principal stretches. This function is no longer a measure of stored energy, therefore the name pseudo-energy function:

$$W(\lambda_1, \lambda_2, \eta) = \eta\tilde{W}(\lambda_1, \lambda_2) + \phi(\eta) \tag{2.25}$$

where $\tilde{W}$ denotes a primary loading path (for instance the blue loading curve in Figure 2.18), without damage. The damage variable η scales the original energy function $\tilde{W}$ and the damage function $\phi(\eta)$ is a measure of energy used to damage the material. In the Ogden-Roxburgh model, the damage function is defined as:

$$-\frac{\partial\phi}{\partial\eta} = m\text{erf}^{-1}(r(\eta - 1)) + W_{\text{m}} \tag{2.26}$$

where m and r are material parameters, erf^{-1} is the inverse of the error function and W_{m} is the energy attained at the maximum stretch of the original loading path. This results in the following definition of the damage variable:

$$\eta = 1 - \frac{1}{r}\text{erf}\left[\frac{1}{m}(W_{\text{m}} - \tilde{W})\right] \tag{2.27}$$

Similar to equation (2.2), the stress in a three dimensional case is then given by the second Piola-Kirchhoff stress tensor $\boldsymbol{P}$:

$$\boldsymbol{P} = 2\frac{\partial W}{\partial \boldsymbol{C}} = 2\eta\frac{\partial\tilde{W}}{\partial \boldsymbol{C}} \tag{2.28}$$

where $\boldsymbol{C}$ is the right Cauchy-Green deformation tensor. So the damage variable η lowers the value of the stress (second Piola-Kirchhoff stress tensor) at a certain strain (right Cauchy-Green deformation tensor).

Permanent Strain Set

While the aforementioned Ogden-Roxburgh model is capable of modeling some prominent features of the Mullins effect in rubber and is included in the ANSYS finite element program, it is not capable of reproducing the permanent strain set. Some other models that do include the permanent strain set (for instance, the Dorfmann-Ogden model [23]), are not included in commercial finite element programs and, as such, less desirable. In literature, there does not seem to exist a suitable model that includes permanent strain set and is also included in finite element programs or otherwise easy to implement.

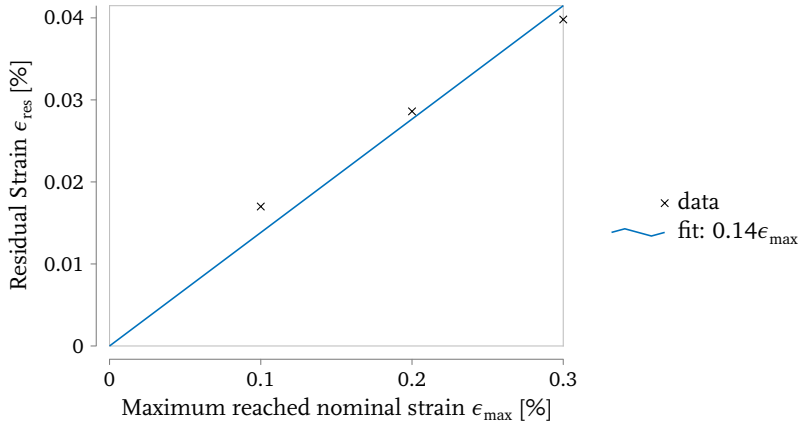

Figure 2.23: Linear approximation of permanent strain set

A more pragmatic solution is needed to facilitate the inclusion of the permanent strain set in rubber modeling. With this in mind, the data from the uniaxial experiment described in [64] and depicted in Figure 2.20 on the left is used to fit a straight line which represents the residual strain that remains after a certain maximum reached stretch. This linear fit and the data it is based upon is depicted in Figure 2.23. The choice for the uniaxial experiment instead of the equi-biaxial experiment is made because the uniaxial experiment is similar to the process of weatherstrip assembly. The resulting fit is described by the following function:

$$\epsilon_{res} = 0.14\epsilon_{max} \tag{2.29}$$

where ϵ_{res} is the residual strain, remaining after unloading and ϵ_{max} is the maximum reached nominal strain during loading. A constraint of the fit is that the function starts in the origin, since a residual strain cannot be nonzero when the specimen has not been loaded yet.

Elasto-Plastic Model

In [45] it is suggested to model the amplitude dependent behavior with Coulomb friction elements. Together with spring elements, a setup similar to the generalized Maxwell model would result in an elasto-plastic model, see Figure 2.24. Here the Coulomb friction coefficients are given by μ. This model can also be used to describe hardening behavior [45, 50], but it is not used for modeling the Mullins effect.

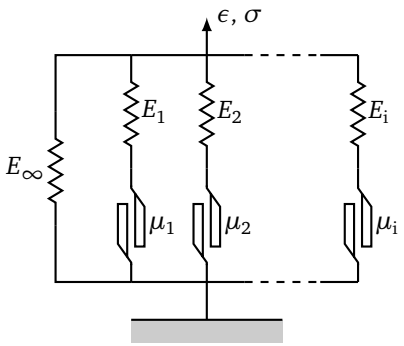

Figure 2.24: Generalized elasto-plastic model

2.2.7 Choice of Material Models

In this chapter some important effects in rubber material are mentioned and models to simulate these effects are given. In Chapter 3 simulations are performed to investigate the influence of the effects mentioned in this chapter. Not all effects and models are useful for modeling the process of weatherstrip assembly. In this section, choices are made with regard to which effects will have to be modeled and which models will be used for the weatherstrip assembly process, for each of the three main categories of material behavior (nonlinear elasticity, visco-elasticity and inelastic behavior).

Nonlinear Elastic Model

From the figures in Section 2.2.2 it is clear that it is necessary to include nonlinear behavior in simulations of the weatherstripping process.

The James-Green-Simpson model [2, 63], the Arruda-Boyce model [22] and the Ogden model [18, 64] have been used to model EPDM weatherstrips. The Arruda-Boyce model is used in [22] to model the compression of an EPDM weatherstrip seal, a Prony series approach is used to model relaxation behavior. The Ogden model is used in [18] together with the Ogden-Roxburgh model to also include the Mullins effect. The experiments (uniaxial tension) used in [18] to determine material parameters are more in line with the weatherstrip assembly process studied in this project, than the compression test used in [22].

Therefore the Ogden model together with the Ogden-Roxburgh model with accompanying material parameters from [18] is chosen to be used in this study to model the nonlinear elastic behavior and the Mullins effect.

Viscoelastic Model

The Prony series approach has the ability to model all viscoelastic effects mentioned in Section 2.2.3, and is also included in the ANSYS finite element program. In [22] the Prony series approach is used to model relaxation of an EPDM weatherstrip. The material parameters from the study can be used to model relaxation in the weatherstrip assembly process. It is not possible to combine these parameters with the Ogden model for nonlinear elasticity because they originate from a totally different experiment (uniaxial tension of a solid specimen [18] versus radial compression of a hollow tube [22]). The data is however usable for investigating the effects of relaxation on the weatherstrip assembly process.

The Prony series approach is chosen to model viscoelastic behavior in Chapter 3.

Inelastic Behavior Model

In Section 2.2.5 it is argued that the Mullins effect is important to consider in this study, while the Payne effect may be disregarded. The Mullins effect can be partly modeled with the Ogden-Roxburgh model and data from [18]. This is convenient since this model is also included in the nonlinear elastic model. The remaining effect of permanent strain set can be modeled with the linear approximation from Equation (2.29).

For the inelastic behavior, the Ogden-Roxburgh model is chosen to model the Mullins effect together with the linear approximation from Equation (2.29).

2.3 Conclusions

In this chapter an investigation on robotic assembly is performed, it is concluded that robotized sealing of automotive weatherstrips is not widely being used or reported in literature.

Furthermore the mechanical behavior of rubber materials is investigated and several effects specific to rubber have been identified. Different models to describe these effects have been proposed and a selection of which models to use is made; the nonlinear elastic behavior will be modeled with the Ogden and the Ogden-Roxburgh model, the viscoelastic behavior will be modeled with the Prony series approach and the inelastic behavior will be modeled with the Ogden-Roxburgh model together with a linear approximation.

Chapter 3

Rubber Modeling and Simulations

In this chapter, several simulations of rubber behavior are performed. The goal of these simulations is to find out how different material models and material data influence the behavior of the simulated experiments. Since there are a lot of different models reported in literature, it is reasonable to believe that the choice for a certain model has a big influence on the simulation results.

3.1 Nonlinear Elasticity

3.1.1 Comparison of Nonlinear Models for a Uniaxial Tension Test

First a uniaxial tensile test is simulated using material models and material data found in literature. In [22], five different material models with accompanying sets of material parameters are reported, and are used to model the compression of weatherstrip seal made from sponge EDPM rubber. Three of these models are used to simulate a uniaxial tension test, the results are depicted in Figure 3.1. While the material parameters for the three models are fitted trough the same data in [22], they produce quite different results. The nominal stress at maximum stretch is more than 2 times higher for the Ogden model than for the Mooney-Rivlin model. This shows that the choice of the used model may have a significant influence on the simulation results. In this specific case it becomes clear that these models and parameters are not suitable to simulate stretch ratios above 1.5, they deviate too much from each other to be reliable. The used material parameters and ANSYS APDL input listing can be found in Appendix A.

Figure 3.2 shows the results of the same simulation, but with different material models. In this case, dense EPDM rubber models and data are used from different sources. The first model used is a 3-term Ogden model fitted trough data from a uniaxial tension experiment in [18]. The second model is a James-Green-Simpson model, used in [63]. The model parameters are determined by nonlinear least-squares fitting of uniaxial and pure shear experimental data from Ford. The third model is also a 3-term Ogden model, reported in [64]. It is not clear if this data is a result of a uniaxial tension test or an equi-biaxial tension test. The used material parameters and ANSYS APDL input listing can be found in Appendix A.

From Figure 3.2 it can be concluded that in the case of material data and material models from different sources, the difference in results is even bigger than in the case shown in Figure 3.1. This leads to the conclusion that it is not wise to take material models and material data at face value; it has to be assured that the material model and parameters are based on experimental data from experiments similar to the problem at hand [28]. Because of this realization a project is started to

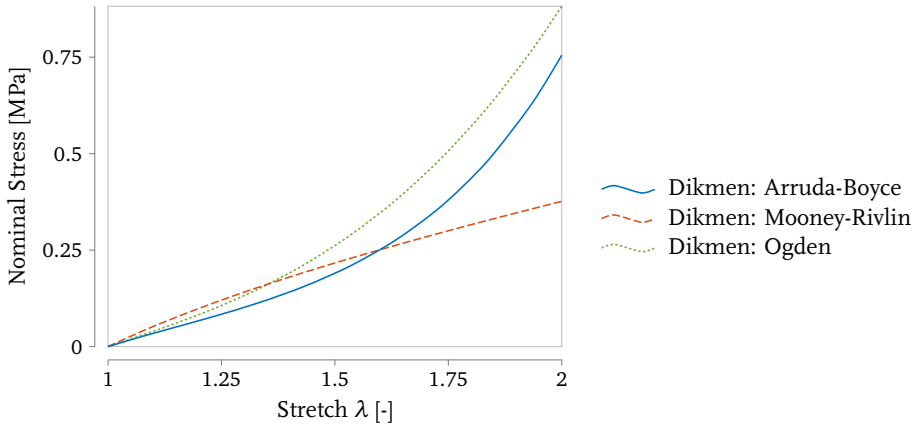

Figure 3.1: Sponge rubber models, data from [22, Dikmen]

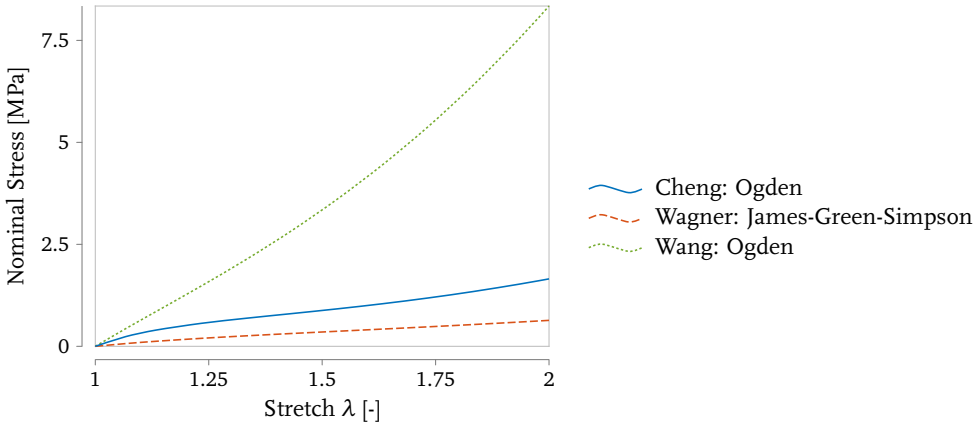

Figure 3.2: Dense rubber models, data from [18, Cheng], [63, Wagner] and [64, Wang]

experimentally investigate the material properties of weatherstrips used in the automotive industry [59].

3.1.2 Linearizing at Small Stretch Ratio

For the process of weatherstrip assembly, it is not expected to encounter large stretch ratios over the entire weatherstrip. A uniaxial simulation should therefore consider small stretch ratios. Moreover, for small stretch ratios it may be possible to approximate the nonlinear behavior with a linear relationship between stretch and stress. Figure 3.3 depicts a simulation of a uniaxial tension test with the same material models and parameters as in Figure 3.2, but now for a small stretch ratio. The marked solid lines represent linear approximations to the results of the nonlinear simulations. From this figure it is clear that the Wagner model and the Wang model have an almost perfect linear representation in this region. The linear fit for the Cheng model deviates somewhat from the nonlinear results, but has still good agreement. This motivates the idea to use a linear material model to model the rubber behavior at small stretches. A complicating factor is that this simulation is a simple uniaxial tension test, while in the real application more complicated deformations will be encountered. The stretch-stress behavior could still be highly nonlinear in that case.

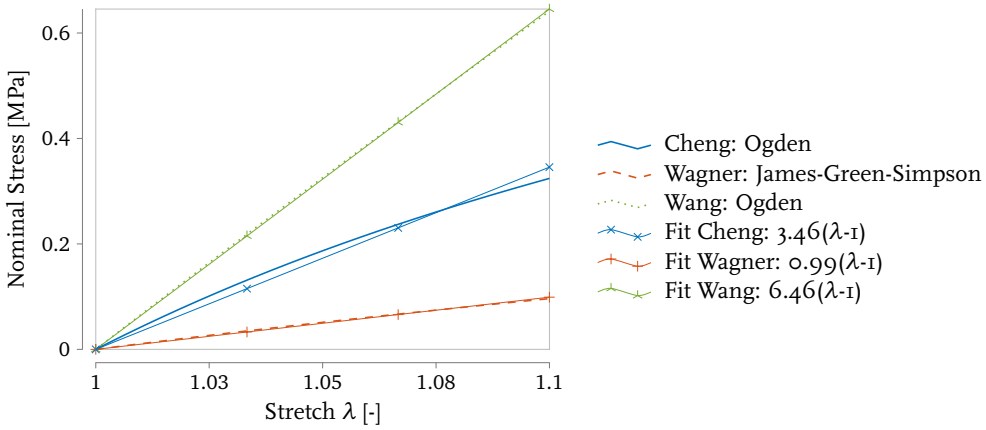

Figure 3.3: Linear fit results for a small stretch ratio, data from [18, Cheng], [63, Wagner] and [64, Wang]

3.1.3 Including Compression

Hyperelastic materials may behave stiffer in compression than in tension, and the process of weatherstrip assembly may include pressing the weatherstrip to a surface. This means it is important to investigate the compresison behavior. The models used in the experiment depicted in Figure 3.3 are not calibrated for compression, only for tension, so their validity in the compression region is not guaranteed. Figure 3.4 depicts the results from a simulated compression and tension experiment. Tension is included to show the difference between tension and compression. The figure shows that all models tend to get stiffer for higher compression compared to the linear approximation of the tension experiment. The Ogden model from the paper of Cheng [18] deviates the most from its linear (tension) approximation. This indicates that care has to be taken when a linear approximation is used and compression is involved.

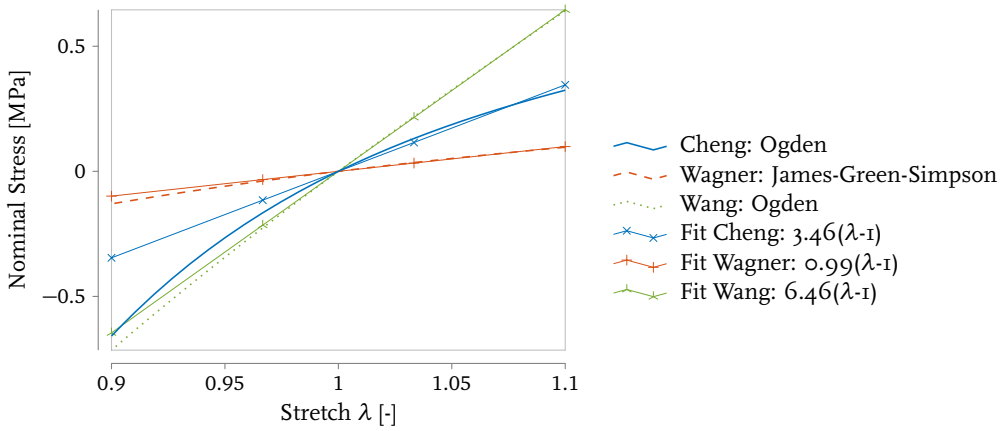

Figure 3.4: Uniaxial compression and tension, with fit results from uniaxial tension, data from [18, Cheng], [63, Wagner] and [64, Wang]

3.1.4 Mullins Effect

To investigate if the Mullins effect is significant in the process of weatherstrip assembly, some experiments are simulated. The first experiment is a recreation of an experiment detailed in [18]. Here the authors measured the nominal stress in a specimen that was uniaxially loaded and unloaded in tension with four different stretch ratios. The experimental data and the simulation result are depicted in Figure 3.5, the ANSYS APDL listing and material parameters can be found in Appendix A.2. This figure shows that there is good agreement between experimental and simulation results. It also shows that this model does not take into account the permanent strain set.

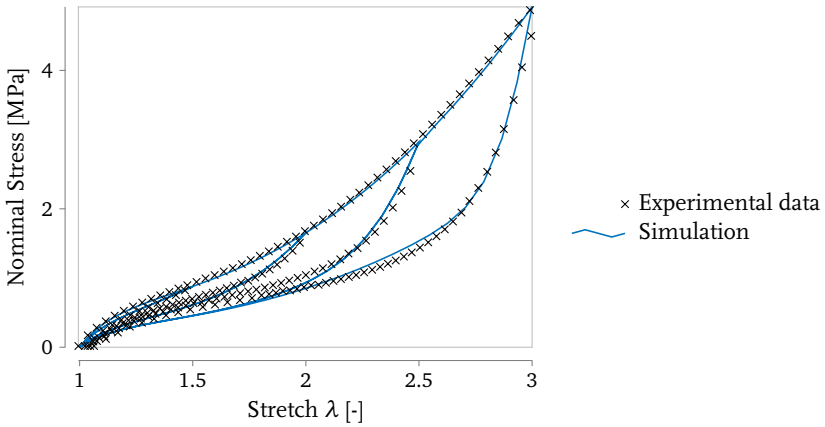

Figure 3.5: Modeling the mullins effect, data from [18]

A simulation of the Mullins effect for a small stretch ratio is conducted and the results are depicted in Figure 3.6. A simulation with a stretch ratio of 1.1 did not show any hysteresis, so a larger stretch ratio was chosen to show the effect (albeit small). This figure shows that the Mullins effect is negligible for small stretch ratios according to this model and material parameters. Therefor it is also concluded that the permanent strain set, as part of the Mullins effect, is expected to be negligible. It has to be noted that the model parameters are fitted to large stretch experimental data, so it may misrepresent

the behavior for small stretch ratios. The linear approximation to the uniaxial tension experiment is also shown in this figure and it shows good agreement to the simulation data for stretch ratios below 1.1.

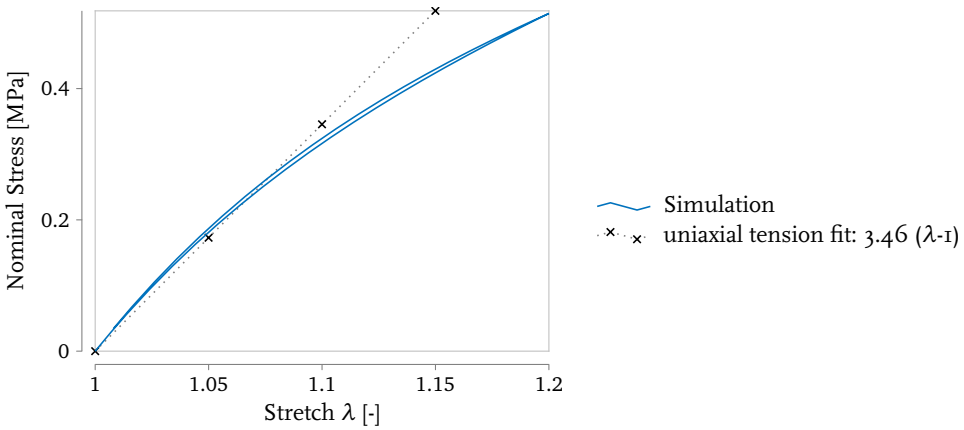

Figure 3.6: Modeling the mullins effect for a small stretch ratio

3.2 Viscoelasticity

3.2.1 Stretch Rate

An experiment to investigate the influence of loading rate effects is carried out in [18], as shown in Figure 2.14. That figure indicates that the loading rate may have a big influence on the behavior of the specimen, especially at high stretch ratios. For low stretch ratios, the curves seem to overlap each other. The material data provided by [18] is used to simulate a uniaxial tension test with different loading rates at low stretch ratios. The different loading rates are simulated by means of different material parameters. As a consequence, the models are still just nonlinear-elastic, they do not inhibit relaxation or creep behavior. The low loading rate simulation uses the same 3-term Ogden model and data as seen in Figures 3.2, 3.3, 3.4, 3.5 and 3.6. The high loading rate simulation also uses a 3-term Ogden model, of which the material parameters are given in Appendix A.3. The ANSYS APDL input listing can also be found in Appendix A.3.

Figure 3.7 shows the result of the simulations for small stretch ratios. The figure indicates that for low stretch ratios, the low and high loading rates produce quite similar results. Considering that the low loading rate is impractically low whereas the high loading rate is unfeasibly high, a more realistic value (in the case of weatherstrip assembly) would end up between the two extremes. A feasible loading rate for the weatherstrip assembly process is estimated to be $0.1\,s^{-1}$ to $1\,s^{-1}$.

3.2.2 Relaxation

A second simulation is performed, this time with viscoelastic material parameters extracted from [45]. In that paper the authors perform experiments on various types of rubber and determine, among others, the dynamic modulus and damping for each material. The material parameters for EPDM rubber are extracted from this paper (see Appendix B) and used to simulate a relaxation experiment. In Figure 3.8 the results of these simulations are shown. The left side of this figure shows stress versus stretch ratio curves, the right side shows stress versus time curves. The model used (*linear*

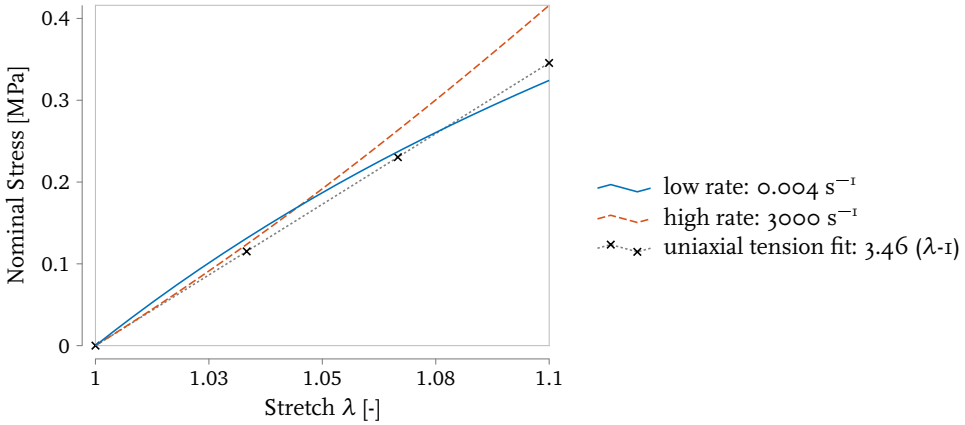

Figure 3.7: Uniaxial tension simulation with different stretch rates

Prony model) is a normal linear elastic material model combined with a three term Prony series for the viscoelastic behavior. The first simulation is a step input in stretch ratio, to a stretch ratio of 1.1. The next three simulations are ramped inputs with different loading rates, but all to the same stretch ratio of 1.1. Interesting to note is the relatively high peak stress for the step input and the relatively low steady state stress. The difference between these two values is the effect of relaxation and is in this case very large. For lower, and more realistic, loading rates the stress peak is lower and the difference between peak and steady state value is smaller. Also, the stress in this simulation is a magnitude higher than the stress in similar experiments with a hyperelastic model such as the ones depicted in Figures 3.3 and 3.7. This means that while the material used in both [45] and [18] is the same, different experimental measuring methods result in different material parameters. Consequently, it is hard to use the linear Prony model to investigate the effects of relaxation and creep because it produces stress values that are incompatible with the ones obtained with the Cheng model.

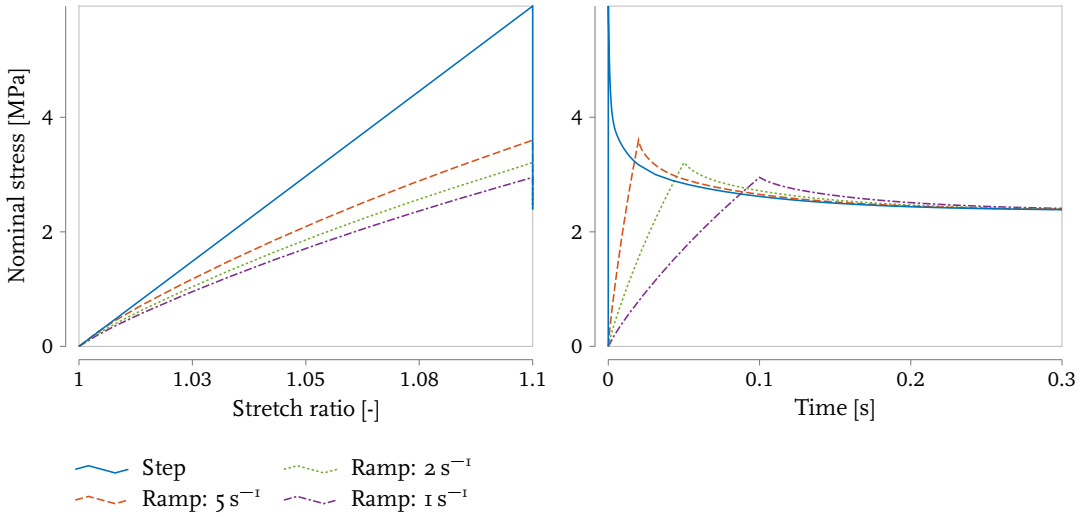

Figure 3.8: Uniaxial tension simulation with a 3-term Prony series viscoelastic model and different loading cases to a stretch ratio of 1.1

Unfortunately there are no viscoelastic parameters for the Ogden model of Cheng [18] or viscoelastic experimental data available. One method to overcome this lack of data is to use viscoelastic data from another source and combine this with the Ogden model of Cheng to create a *hyperelastic Prony model*. In Figure 3.9 the results of the same simulations as depicted in Figure 3.8 but with a combined 3-term Ogden and 3-term Prony series visco-hyperelastic model are shown. It has to be noted that the hyperelastic Prony model is a combination of two different sources and, as such, it is not possible to test the reliability of this model. The material parameters and the ANSYS code listing for this model can be found in Appendix A.4. It can, however, be noticed that the hyperelastic Prony model gives stress results comparable to results shown in Figure 3.7 for the step input, but has very low steady state values. The nature of the Prony series, as shown in equations (2.18) and (2.22), results in the fact that it scales the stiffness of a material model down over time, from the instantaneous response parameters towards the equilibrium response parameters, see Figure 2.11. The 3-term Ogden model from Cheng is measured with a very low loading rate ($0.004\,s^{-1}$), so the steady state results from a visco-hyperelastic model should be similar to the results of the Cheng hyperelastic model. This is not the case for the hyperelastic Prony model, because of the nature of the Prony series as explained above.

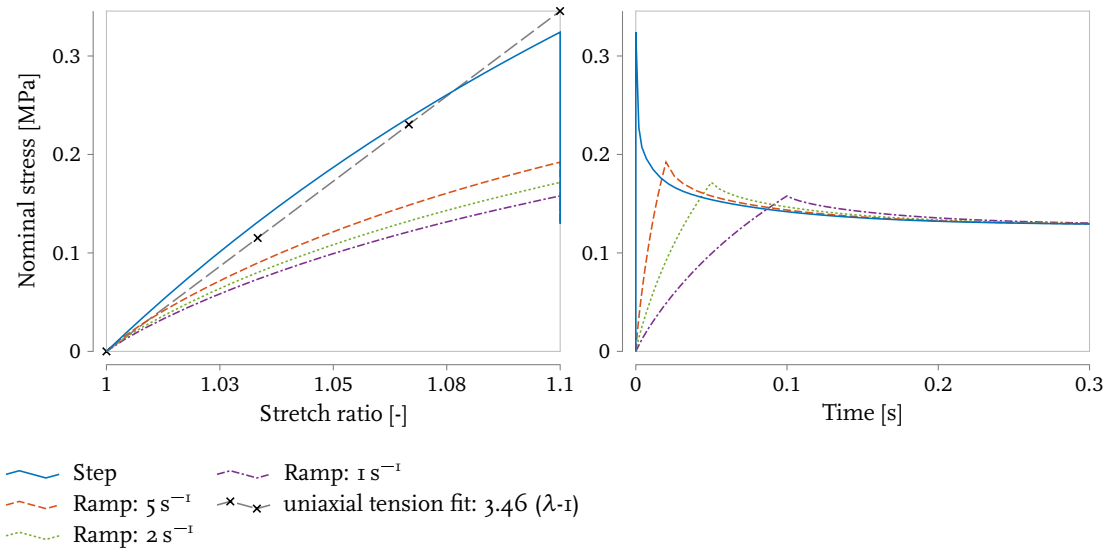

Figure 3.9: Uniaxial tension simulation with a combined 3-term Prony series and 3-term Ogden visco-hyperelastic model and different loading cases to a stretch ratio of 1.1

While it is clear that the hyperelastic Prony model and resulting simulation results as shown in Figure 3.9 are not compatible with the results shown in Figure 3.7, there are some things to learn from this model. The hyperelastic Prony model predicts that the relaxation effect is severe when the material is loaded with a high loading rate. For slow loading rates, the effect of relaxation seems relatively small. Moreover, it could be argued that this effect (and consequently, also the effect of creep) can be safely ignored in the process of weatherstrip assembly, where loading rates would be between $0.1\,s^{-1}$ and $1\,s^{-1}$.

3.3 Conclusions

Simulations with different material models from different sources show that it is possible to use a linear approximation of the nonlinear hyperelastic behavior for small stretch ratios, which are to be expected in weatherstrip assembly. It is also shown that for small stretch ratios, the Mullins effect hardly manifests itself, so it can be neglected. Relaxation and creep behavior have been shown to have a large effect on the maximum stress in the material, however, this is only the case for fast loading. In the case of weatherstrip assembly where the loading rate is assumed to be small, the effects of relaxation and creep seem to be small enough to neglect. The simulation results in this chapter support the idea to model the weatherstrip behavior with a linear elastic model; in the next chapter a comparison is made between the nonlinear finite element model and a linear elastic model.

Chapter 4

Finite Element Model Simulations of Weatherstrip Assembly

In this chapter finite element model simulations of the weatherstrip application process are performed. The goal is to develop a linear elastic model which can be used as a state-space model in Matlab. This means that hyperelasticity, inelastic behavior, relaxation and creep cannot be taken into account or have to be approximated in the final Matlab model. In Chapter 3 it has already been argued that the behavior of EPDM rubber can be approximated by a linear elastic material model. Effects of relaxation, creep and inelastic behavior are assumed to be of no concern in the weatherstrip assembly process. However, as can be seen in Figure 3.4, while the linearized models perform satisfactory in tension, they do not perform as well in compression. In this chapter a comparison between hyperelastic and linear elastic material models in the weatherstrip assembly process is made.

4.1 Weatherstrip Model

The process of weatherstrip assembly in reality involves quite long weatherstrips. In FEM models modeling long geometries requires al lot of elements which negatively impact solution times or even prohibits a solution. As argued in Chapter 3, the behavior of the EPDM rubber used in the weatherstrip can be approximated by a linear elastic behavior within a small stretch range. This means that it is not necessary to model the entire strip, but it is sufficient to model only the part of the strip between the dispenser and the application point.

The geometry of the rubber weatherstrip used in this study is shown in Figure 4.1, where the values of the measurements are given as:

$L_x = 4\,\text{mm}$	width of strip
$L_y = 4\,\text{mm}$	half height of strip
$L_z = 20\,\text{mm}$	length of strip
$r_1 = 4\,\text{mm}$	radius of rounded top of strip
$r_w = 10\,\text{mm}$	radius of applicator wheel
$L_w = 8\,\text{mm}$	position of applicator wheel in z-direction

The hyperelastic material model used is the 3-term Ogden model from the paper of Cheng [18],

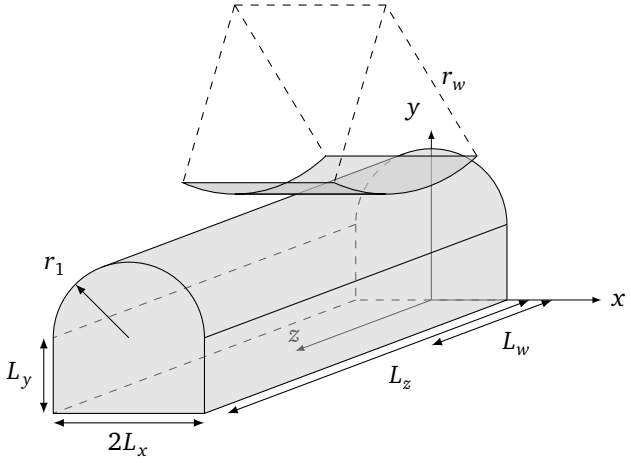

Figure 4.1: Geometry of rubber weatherstrip and applicator wheel

the Ogden model is given by equation (2.11):

$$W = \sum_{i=1}^{N} \frac{\mu_i}{\alpha_i}(\lambda_1^{\alpha_i} + \lambda_2^{\alpha_i} + \lambda_3^{\alpha_i} - 3)$$

where the parameters are given in Table 4.1.

Table 4.1: Material parameters for 3-term Ogden hyperelastic model

	parameter values		
parameter	1	2	3
μ_i	7.45×10^{2}	-2.39×10^{2}	-3.03×10^{-1}
α_i	-6.73×10^{-2}	-2.13×10^{-1}	-7.27

The linear elastic model is a linearization of the hyperelastic material, as shown in Figure 3.3, with a stiffness of 3.46 MPa.

In the simulations detailed in subsequent sections, the model geometry and parameters as given above are used, unless explicitly specified otherwise. It is also assumed that friction between the applicator wheel and the top of the weatherstrip and friction between the bottom of the weatherstrip and the substrate are of no concern. Appendix C describes a simulation where a comparison is made between a model with friction and an model without friction. From this simulation it is concluded that the friction effect can be disregarded in simulating the weatherstrip application process.

The ANSYS ADPL code used to produce the simulations in this chapter can be found in Appendix A.5.

4.2 Application Pressure

A finite element simulation is performed to investigate the desired application pressure on the weatherstrip for good adhesion. Double sided tape is used to bond the weatherstrip to the substrate, these tapes typically need an application pressure of 100 kPa [1] for a strong bond. An application force of 10 N is applied to the top of the weatherstrip with an applicator wheel, to achieve the desired

bonding pressure at the bottom of the strip. Two different simulations are carried out, one with the hyperelastic material as described in Chapter 4.1, and one with a linear elastic material.

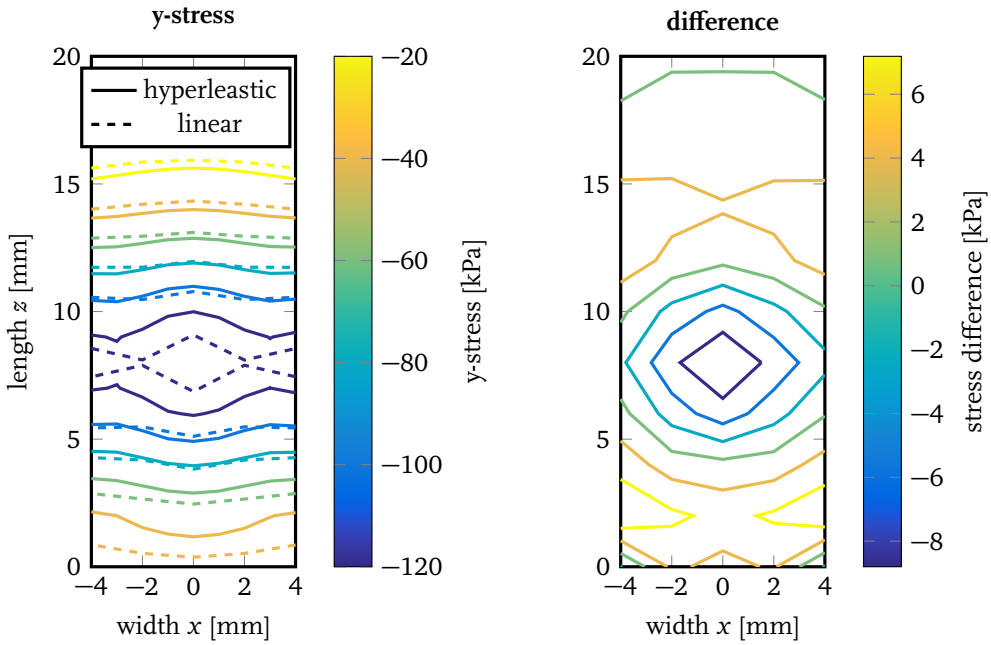

Figure 4.2: Stress distribution on bottom of weatherstrip: hyperelastic and linear model on the left and the difference between these two models on the right.

In Figure 4.2 the resulting stress in global y-direction at the bottom of the weatherstrip is shown for the two different material models. In the right figure the difference between these two simulations is depicted. From the left figure it is apparent that both models predict an area (between about 6 mm to 10 mm in the length of the strip, directly under the center of the applicator wheel) where the pressure is high enough to result in a strong bond. Both models give a comparable stress distribution, with only small differences between the two models (with a maximum of 8 kPa on a total of above 120 kPa). It has to be noted that the linear model has a coarser mesh than the hyperelastic model (element edge size of 2 mm for the linear model, versus 1 mm for the hyperelastic model), which partly explains the difference between these models. Figure 4.2 indicates that a linearization of the hyperelastic model gives adequate results, when only taking stress distribution into account. Since it is shown in Section 3.1.3 that the linear elastic model has better agreement with the nonlinear hyperelastic model in the tension regime than in the compression regime, there is reason to assume that the linear elastic model will achieve better results in the simulation shown in Figure 4.2 when it is fitted to compression test data.

Figure 4.3 depicts the displacement in the global x-direction (sideways) on the bottom of the weatherstrip as a result from the application pressure. On the left the results for the hyperelastic and linear model are shown and on the right the difference between these two models is shown. The maximum displacement in these figures is 0.04 mm which is negligible for the process of weatherstrip assembly, so the quantitative results of this simulation are of little concern for this process. These simulation results can be used, however, as a reference for the further development of the finite element model into a linear state-space model.

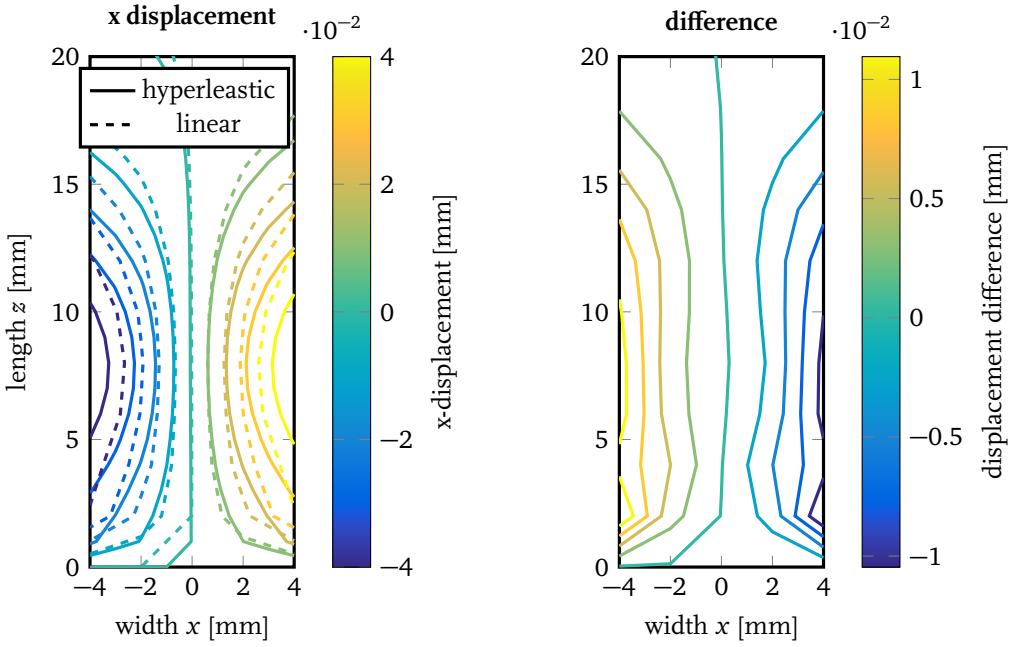

Figure 4.3: Displacement in x-direction on bottom of weatherstrip: hyperelastic and linear model on the left and the difference between these two models on the right.

4.3 Conclusion

A comparison is made between a nonlinear hyperelastic model of the weatherstrip and a linear elastic model of the weatherstrip. This comparison shows that the linear model can adequately represent the behavior of the weatherstrip for the expected load case, and can be used as a starting point for the creation of a linear state-space model of the weatherstrip.

Chapter 5

Linear State-Space Model

In the previous chapter finite element simulations of the weatherstrip behavior are performed with the hyperelastic and linear material models. In this chapter the linear finite element model is converted into a linear state-space model. The reason behind this is that a linear state-space model is well suited for control design and servo control simulations in a numerical software package, such as Matlab [36]. Moreover a linear state-space system can be used as a basis for a state observer to estimate deformations in the rubber and interaction forces that are not directly measurable on the physical system. Furthermore, the linear state-space model is reduced in order with model order reduction techniques to make it computationally more efficient.

The process of creating a linear state-space model from an ANSYS FEM model is automated in Matlab, that is, dedicated tools are developed in this project to perform the tasks that are described in this chapter. The objective behind this is to automatize the process of generating a usable model for control design and servo simulations, since for each different weatherstrip (different geometry and material properties) a new FEM model needs to be created which, in turn, is used to create a state-space model.

5.1 Importing Linear FEM Model into Matlab

Starting from a finite element analysis, which is performed in Chapter 4, there are generally two possible methods to create a linear state-space system from the finite element model [27, 32]: the *nodal* form method and the *modal* form method. The modal form is widely used in engineering practice but has some drawbacks. The next paragraphs explain each form and why one is chosen over the other one. Both methods start with a modal analysis in the ANSYS software (see Appendix A.6).

5.1.1 Modal Analysis in ANSYS

An n-DOF (*degree of freedom*) general second order dynamical system can be written as:

$$\boldsymbol{M}\ddot{\boldsymbol{q}} + \boldsymbol{B}\dot{\boldsymbol{q}} + \boldsymbol{K}\boldsymbol{q} = \boldsymbol{f} \tag{5.1}$$

where $\boldsymbol{M}$, $\boldsymbol{B}$ and $\boldsymbol{K}$ are the $n \times n$ mass, damping and stiffness matrices, respectively, $\boldsymbol{q}$ denotes the $n \times 1$ nodal displacement vector and $\boldsymbol{f}$ is an $n \times 1$ force vector. For a static finite element simulation as the one described in Chapter 4, the stiffness matrix $\boldsymbol{K}$ is readily available, the mass matrix $\boldsymbol{M}$ can easily be created when the density of the material is known, while the damping matrix $\boldsymbol{B}$ is generally not known. For most modal analysis with lightly damped systems the damping matrix is omitted since

it has little influence on the modal behavior. For the transient behavior, servo control simulations for instance, $\boldsymbol{B}$ is needed to model the damping behavior of the process. Consequently the damping is not considered during modal analysis, but it has to be included when the state-space system is created in Section 5.3.

The undamped system can be used to compute the unforced response ($\boldsymbol{f} = 0$), a so called modal analysis. In ANSYS software a modal analysis is performed for undamped systems of the following form [5]:

$$\boldsymbol{M}\ddot{\boldsymbol{q}} + \boldsymbol{K}\boldsymbol{q} = \boldsymbol{0} \tag{5.2}$$

For free vibrations of the system (5.2), of the form:

$$\boldsymbol{q} = \boldsymbol{\phi}_i \cos(\omega_i t) \tag{5.3}$$

where $\boldsymbol{\phi}_i$ ($n \times 1$) is the ith eigenvector corresponding to the ith eigenvalue ω_i of the system described by (5.2), the system (5.2) can be re-written as:

$$(-\boldsymbol{\Omega}^2\boldsymbol{M} + \boldsymbol{K})\boldsymbol{\Phi} = \boldsymbol{0} \tag{5.4}$$

where $\boldsymbol{\Omega}$ is an $n \times n$ diagonal matrix containing the eigenvalues:

$$\boldsymbol{\Omega} = \begin{bmatrix} \omega_1 & & & 0 \\ & \omega_2 & & \\ & & \ddots & \\ 0 & & & \omega_n \end{bmatrix} \tag{5.5}$$

and $\boldsymbol{\Phi}$ is an $n \times n$ matrix with eigenvectors. This eigenvalue problem can be solved quite efficiently in most finite element programs.

5.1.2 Nodal Form

The nodal form is a method to create a state-space system from the finite element model (5.2):

$$\begin{aligned} \dot{\boldsymbol{x}}_{\mathrm{n}} &= \boldsymbol{F}_{\mathrm{n}}\boldsymbol{x}_{\mathrm{n}} + \boldsymbol{G}_{\mathrm{n}}\boldsymbol{u} \\ \boldsymbol{y} &= \boldsymbol{H}_{\mathrm{n}}\boldsymbol{x}_{\mathrm{n}} + \boldsymbol{D}_{\mathrm{n}}\boldsymbol{u} \end{aligned} \tag{5.6}$$

Where $\boldsymbol{x}_{\mathrm{n}} = [\boldsymbol{q}\ \dot{\boldsymbol{q}}]^{\mathrm{T}}$ is the $2n \times 1$ state vector, $\boldsymbol{A}_{\mathrm{n}}$ is the $2n \times 2n$ system matrix, $\boldsymbol{B}_{\mathrm{n}}$ is the $2n \times m$ input matrix for m inputs, $\boldsymbol{C}_{\mathrm{n}}$ is the $l \times 2n$ output matrix for l outputs, $\boldsymbol{D}_{\mathrm{n}}$ is the $l \times m$ feedthrough matrix, and are given by:

$$\begin{aligned} \boldsymbol{F}_{\mathrm{n}} &= \begin{bmatrix} \boldsymbol{0} & \boldsymbol{I} \\ -\boldsymbol{M}^{-1}\boldsymbol{K} & \boldsymbol{0} \end{bmatrix}, & \boldsymbol{G}_{\mathrm{n}} &= \begin{bmatrix} \boldsymbol{0} \\ \boldsymbol{M}^{-1} \end{bmatrix} \\ \boldsymbol{H}_{\mathrm{n}} &= \begin{bmatrix} \boldsymbol{I} & \boldsymbol{0} \end{bmatrix}, & \boldsymbol{D}_{\mathrm{n}} &= \begin{bmatrix} \boldsymbol{0} \end{bmatrix} \end{aligned} \tag{5.7}$$

In the nodal form, these matrices are directly related to the mass and stiffness matrices $\boldsymbol{M}$ and $\boldsymbol{K}$ of the ANSYS model (equation (5.2)), and do not depend on the *results* of the modal analysis. Using ANSYS it is, however, needed to *create* the modal analysis, to be able to extract the mass and stiffness matrices $\boldsymbol{M}$ and $\boldsymbol{K}$, respectively. In most cases the number of inputs and outputs are lower than the number of DOFs which means that the matrices $\boldsymbol{B}_{\mathrm{n}}$, $\boldsymbol{C}_{\mathrm{n}}$ and $\boldsymbol{D}_{\mathrm{n}}$ and the vectors $\boldsymbol{u}$ and $\boldsymbol{y}$ are not their full size.

5.1.3 Modal Form

The modal form method uses the eigenvalues and eigenvectors from the eigenvalue problem (5.4) and is written as:

$$\begin{aligned} \dot{\boldsymbol{x}}_{\mathrm{m}} &= \boldsymbol{F}_{\mathrm{m}}\boldsymbol{x}_{\mathrm{m}} + \boldsymbol{G}_{\mathrm{m}}\boldsymbol{u} \\ \boldsymbol{y} &= \boldsymbol{H}_{\mathrm{m}}\boldsymbol{x}_{\mathrm{m}} + \boldsymbol{D}_{\mathrm{m}}\boldsymbol{u} \end{aligned} \tag{5.8}$$

The state vector in this case is $\boldsymbol{x}_{\mathrm{m}} = [\boldsymbol{\eta}\ \dot{\boldsymbol{\eta}}]^{\mathrm{T}}$, where $\boldsymbol{\eta}$ is an $n \times 1$ modal coordinate vector which has no clear physical interpretation. The system matrices in (5.8) use the results of the modal analysis and are given as:

$$\begin{aligned} \boldsymbol{F}_{\mathrm{m}} &= \begin{bmatrix} \boldsymbol{0} & \boldsymbol{I} \\ -\boldsymbol{\Omega}^2 & \boldsymbol{0} \end{bmatrix} \quad \boldsymbol{G}_{\mathrm{m}} = \begin{bmatrix} \boldsymbol{0} \\ \boldsymbol{\Phi}^{-1} \end{bmatrix} \\ \boldsymbol{H}_{\mathrm{m}} &= \begin{bmatrix} \boldsymbol{\Phi} & \boldsymbol{0} \end{bmatrix}, \qquad \boldsymbol{D}_{\mathrm{m}} = \begin{bmatrix} \boldsymbol{0} \end{bmatrix} \end{aligned} \tag{5.9}$$

5.1.4 Comparison of the Nodal and Modal Forms

Both Nodal and Modal forms have advantages and disadvantages. The conveniences of the nodal form are that it uses the mass and stiffness matrices directly, and since it is written in nodal coordinates it is straightforward to add extra mass or stiffness to certain nodes as desired. The disadvantage of the nodal form is the need to export the entire mass and stiffness matrix from the finite element program to Matlab. These matrices can get quite big for models with thousands of nodes.

The modal form has as advantage that the finite element program can be used for the eigenvalue computation and model reduction by taking the lowest modes into account only. A disadvantage is that the modal coordinates have no clear physical interpretation, so adding extra mass or stiffness becomes challenging. This generally means that the modal form is less flexible from a user perspective than the nodal form, and thus the nodal form is used in this project.

5.1.5 Imported Model in Matlab

The nodal form of the state-space model is used in Matlab by importing the stiffness matrix $\boldsymbol{K}$ and mass matrix $\boldsymbol{M}$ of a weatherstrip sample. Given the node locations, it is possible to visualize the model of the weatherstrip within Matlab, as shown in Figure 5.1. Here, the dots at the corners of the

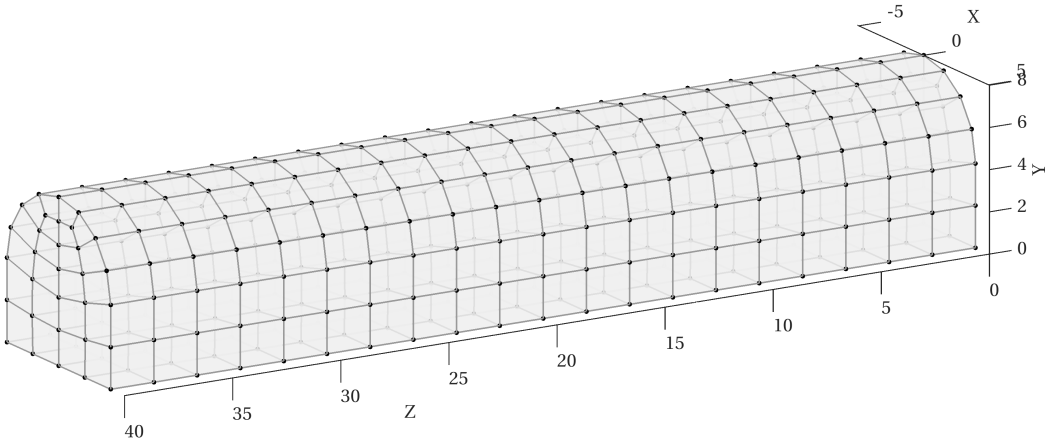

Figure 5.1: Imported mesh in Matlab

shaded elements are the nodes of the model. In the nodal form, the displacement and velocity of these nodes are the state coordinates of the state-space system. In the process of weatherstrip assembly, an applicator wheel will put pressure on the top of the strip, while the bottom is constrained by the substrate on which the strip is attached. An illustration of this process can be seen in Figure 4.1. To be able to interact in this way with the state-space model, the top and bottom nodes of the weatherstrip model are used for motion and force interactions with the environment (applicator and substrate).

5.1.6 Comparison Between the Linear Matlab Model and the ANSYS model

The quality of the state-space model of the weatherstrip depends on its ability to mimic the behavior of the linear finite element model as described in Chapter 4. In the procedure to import the model of the weatherstrip into Matlab, some bookkeeping of nodes, node locations and interaction forces is needed which can introduce errors. It is therefore useful to check the correctness of the stiffness and mass matrix in Matlab. A first check is the comparison of eigenvalues resulting from a modal analysis as described in Section 5.1.1, when performed in ANSYS and Matlab. The result of this check is that the eigenvalues are similar within 3 significant digits, which implies that both the mass and stiffness matrices are imported correctly.

Before the state-space model is created from the imported mass and stiffness matrices, the stiffness matrix can be used to perform a linear static simulation similar to the one shown in Figure 4.2, where the stress on the bottom of the weatherstrip resulting from applicator pressure is simulated. If the linear static simulation can reproduce the FEM result shown in Figure 4.2, that would verify the correctness of the stiffness matrix and increase confidence into the linear state-space model build upon this matrix. In this case, not only bookkeeping errors could occur during import of the stiffness matrix and application of external forces, but also a different algorithm to apply forces and compute stresses could be used. To put it more explicitly, within ANSYS an algorithm is present to simulate contact between objects (for instance, contact between the applicator wheel and the weatherstrip), which is not available in Matlab. Therefore it is needed to approximate this behavior and, as such, some errors can be introduced.

In the static situation, the nodal accelerations are zero and from model (5.2) the stiffness matrix $\boldsymbol{K}$ can be used to compute the nodal displacements $\boldsymbol{q}$:

$$\boldsymbol{K}\boldsymbol{q} = \boldsymbol{f} \tag{5.10}$$

where $\boldsymbol{f}$ is a vector with externally applied nodal forces. In the finite element simulation, as described in Chapter 4 and Appendix A.5, a cylindric wheel is pressed onto the top of the weatherstrip and interaction forces between the wheel and nodes of the weatherstrip are calculated. These reaction forces are exported to Matlab and used as external nodal forces $\boldsymbol{f}$.

In Figures 5.2 and 5.3 comparisons are made between the results from the linear finite element model and from the stiffness matrix model. Figure 5.2 depicts the stress at the bottom of the strip, and Figure 5.3 depicts the sideways displacement of the weatherstrip.

From these figures it is clear that the stiffness matrix model shows good agreement with the linear FEM model, which indicates that the stiffness matrix can be used to create a linear state-space model of the weatherstrip.

5.2 Model Order Reduction with the Craig Bampton Method

In Section 5.1.2 it is shown that a linear state-space model can be created from the mass and stiffness matrices $\boldsymbol{M}$ and $\boldsymbol{K}$, respectively. In the case of a FEM model with n degrees of freedom, the state-space

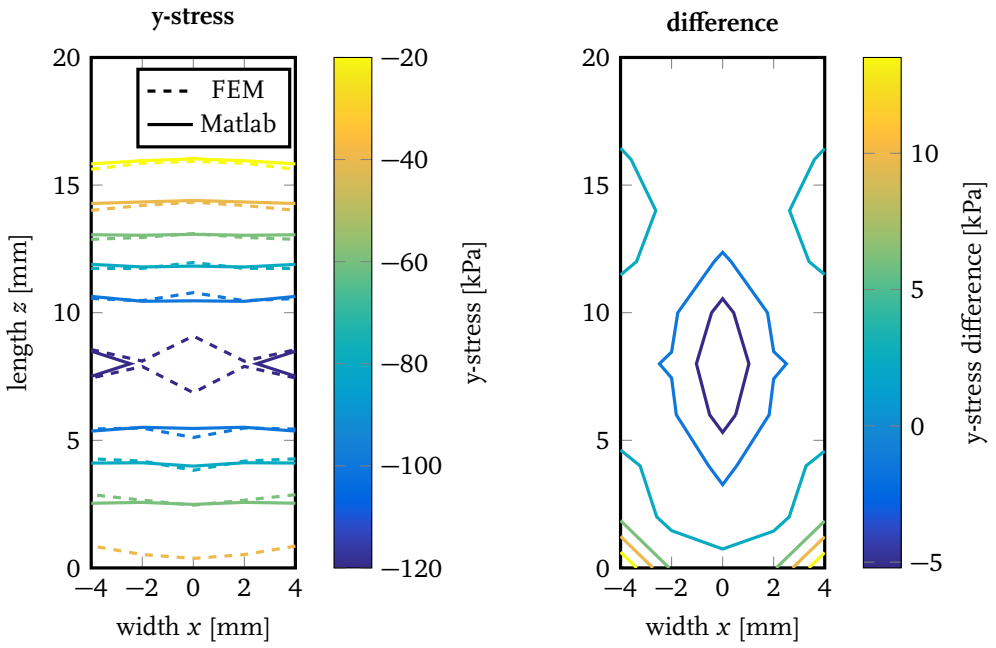

Figure 5.2: Stress distribution at the bottom of the weatherstrip: linear FEM and Matlab model on the left-hand side and the difference between these two models on the right-hand side.

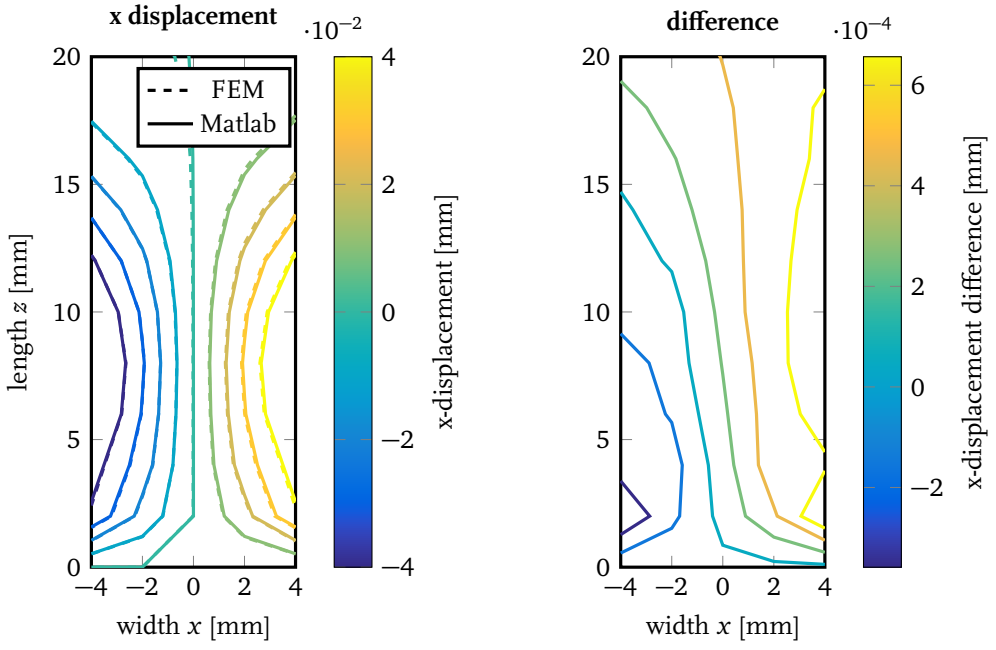

Figure 5.3: Sideways displacement at the bottom of the weatherstrip: linear FEM and Matlab model on the left-hand side and the difference between these two models on the right-hand side.

model based on this FEM model has $2n$ states. It is computationally not advantageous to have a state-space model with a large number of states, so reducing the order of the model is beneficial.

There are various methods to reduce a dynamical model, see [14] for an overview of possible methods. The authors of [14] conclude that for a model that needs to adequately represent the input-output behavior of a system, the *balanced truncation* method is preferred. However, this method is limited to models of moderate size. The FEM model of the weatherstrip is of high dimension (number of DOF ≈ 2000), and it may be necessary to use even bigger models in future investigations. Therefore the balanced truncation method may be inadequate and a different method may be needed.

The *mode displacement* method described in [14] is well suited for large models, but it is focused on the global dynamics of the model and not on the specific input-output behavior.

Taking these considerations into account, a two step method is chosen whereby the FEM model is first reduced with the mode displacement method (specifically: *Craig-Bampton*) to a model of moderate size, and as step two, it is reduced further with the balanced truncation method, taking into account the input-output behavior of the model. Reference [32] provides an in depth explanation of the Craig-Bampton reduction method. A short overview of this method is given below:

Consider a full system with n degrees of freedom:

$$\boldsymbol{M}\ddot{\boldsymbol{q}} + \boldsymbol{B}\dot{\boldsymbol{q}} + \boldsymbol{K}\boldsymbol{q} = \boldsymbol{f} \tag{5.11}$$

where $\boldsymbol{M}$, $\boldsymbol{B}$, $\boldsymbol{K}$, $\boldsymbol{q}$ and $\boldsymbol{f}$ are defined as in (5.2). Damping matrix $\boldsymbol{B}$ can only be included for weakly damped systems or for systems with proportional damping [32]. The vector $\boldsymbol{q}$ is partitioned into an internal part $\boldsymbol{q}_{\mathrm{i}}$ and a boundary part $\boldsymbol{q}_{\mathrm{b}}$. The interaction forces and boundary conditions have to act on the boundary DOFs. This partitioning leads to the following system:

$$\begin{bmatrix} \boldsymbol{M}_{\mathrm{bb}} & \boldsymbol{M}_{\mathrm{bi}} \\ \boldsymbol{M}_{\mathrm{ib}} & \boldsymbol{M}_{\mathrm{ii}} \end{bmatrix} \begin{bmatrix} \ddot{\boldsymbol{q}}_{\mathrm{b}} \\ \ddot{\boldsymbol{q}}_{\mathrm{i}} \end{bmatrix} + \begin{bmatrix} \boldsymbol{B}_{\mathrm{bb}} & \boldsymbol{B}_{\mathrm{bi}} \\ \boldsymbol{B}_{\mathrm{ib}} & \boldsymbol{B}_{\mathrm{ii}} \end{bmatrix} \begin{bmatrix} \dot{\boldsymbol{q}}_{\mathrm{b}} \\ \dot{\boldsymbol{q}}_{\mathrm{i}} \end{bmatrix} + \begin{bmatrix} \boldsymbol{K}_{\mathrm{bb}} & \boldsymbol{K}_{\mathrm{bi}} \\ \boldsymbol{K}_{\mathrm{ib}} & \boldsymbol{K}_{\mathrm{ii}} \end{bmatrix} \begin{bmatrix} \boldsymbol{q}_{\mathrm{b}} \\ \boldsymbol{q}_{\mathrm{i}} \end{bmatrix} = \begin{bmatrix} \boldsymbol{f}_{\mathrm{b}} \\ \boldsymbol{f}_{\mathrm{i}} \end{bmatrix} \tag{5.12}$$

The internal part of this system is used to extract eigenvalues:

$$\left[-\omega^2 \boldsymbol{M}_{\mathrm{ii}} + \boldsymbol{K}_{\mathrm{ii}}\right] \boldsymbol{\phi} = \boldsymbol{0} \tag{5.13}$$

From the n_i solutions, only the first n_k eigenvalues ($\omega_1 \leq \omega_2 < \ldots \omega_n$) and eigenvectors are kept and stored in the matrices $\boldsymbol{\Omega}_{\mathrm{kk}}$ and $\boldsymbol{\Phi}_{\mathrm{ik}}$, respectively:

$$\boldsymbol{\Omega}_{\mathrm{kk}} = \begin{bmatrix} \omega_1 & & & 0 \\ & \omega_2 & & \\ & & \ddots & \\ 0 & & & \omega_n \end{bmatrix} \tag{5.14}$$

$$\boldsymbol{\Phi}_{\mathrm{ik}} = \begin{bmatrix} \boldsymbol{\phi}_1, & \boldsymbol{\phi}_2, & \ldots & \boldsymbol{\phi}_{n_k} \end{bmatrix} \tag{5.15}$$

The reduced mass matrix $\boldsymbol{M}_{\mathrm{CB}}$, damping matrix $\boldsymbol{B}_{\mathrm{CB}}$ stiffness matrix $\boldsymbol{K}_{\mathrm{CB}}$ and force vector $\boldsymbol{f}_{\mathrm{CB}}$ now become:

$$\begin{aligned} \boldsymbol{M}_{\mathrm{CB}} &= \begin{bmatrix} \boldsymbol{M}^{\mathrm{S}}_{\mathrm{bb}} & (\boldsymbol{M}_{\mathrm{bi}} - \boldsymbol{K}^{\mathrm{T}}_{\mathrm{ib}} \boldsymbol{K}^{-1}_{\mathrm{ii}} \boldsymbol{M}_{\mathrm{ii}}) \boldsymbol{\Phi}_{\mathrm{ik}} \\ \mathrm{sym.} & \boldsymbol{\Phi}^{\mathrm{T}}_{\mathrm{ik}} \boldsymbol{M}_{\mathrm{ii}} \boldsymbol{\Phi}_{\mathrm{ik}} \end{bmatrix} \\ \boldsymbol{B}_{\mathrm{CB}} &= \begin{bmatrix} \boldsymbol{B}^{\mathrm{S}}_{\mathrm{bb}} & (\boldsymbol{B}_{\mathrm{bi}} - \boldsymbol{K}^{\mathrm{T}}_{\mathrm{ib}} \boldsymbol{K}^{-1}_{\mathrm{ii}} \boldsymbol{B}_{\mathrm{ii}}) \boldsymbol{\Phi}_{\mathrm{ik}} \\ \mathrm{sym.} & \boldsymbol{\Phi}^{\mathrm{T}}_{\mathrm{ik}} \boldsymbol{B}_{\mathrm{ii}} \boldsymbol{\Phi}_{\mathrm{ik}} \end{bmatrix} \\ \boldsymbol{K}_{\mathrm{CB}} &= \begin{bmatrix} \boldsymbol{K}^{\mathrm{S}}_{\mathrm{bb}} & \boldsymbol{0}_{\mathrm{bk}} \\ \mathrm{sym.} & \boldsymbol{\Omega}^2_{\mathrm{kk}} \end{bmatrix} \\ \boldsymbol{f}_{\mathrm{CB}} &= \begin{bmatrix} \boldsymbol{f}^{\mathrm{S}}_{\mathrm{b}} \\ \boldsymbol{\Phi}^{\mathrm{T}}_{\mathrm{ik}} \boldsymbol{f}_{\mathrm{i}} \end{bmatrix} \end{aligned} \tag{5.16}$$

where the matrices $\boldsymbol{M}_{\mathrm{bb}}^{\mathrm{S}}$, $\boldsymbol{B}_{\mathrm{bb}}^{\mathrm{S}}$, $\boldsymbol{K}_{\mathrm{bb}}^{\mathrm{S}}$ and $\boldsymbol{f}_{\mathrm{b}}^{\mathrm{S}}$ comprise the statically reduced parts and are given as follows:

$$\begin{aligned}
\boldsymbol{M}_{\mathrm{bb}}^{\mathrm{S}} &= \boldsymbol{M}_{\mathrm{mm}} - \boldsymbol{M}_{\mathrm{bi}}\boldsymbol{K}_{\mathrm{ii}}^{-1}\boldsymbol{K}_{\mathrm{ib}} - \boldsymbol{K}_{\mathrm{ib}}^{\mathrm{T}}\boldsymbol{K}_{\mathrm{ii}}^{-1}\boldsymbol{M}_{\mathrm{ib}} + \boldsymbol{K}_{\mathrm{ib}}^{\mathrm{T}}\boldsymbol{K}_{\mathrm{ii}}^{-1}\boldsymbol{M}_{\mathrm{ii}}\boldsymbol{K}_{\mathrm{ii}}^{-1}\boldsymbol{K}_{\mathrm{ib}} \\
\boldsymbol{B}_{\mathrm{bb}}^{\mathrm{S}} &= \boldsymbol{B}_{\mathrm{mm}} - \boldsymbol{B}_{\mathrm{bi}}\boldsymbol{K}_{\mathrm{ii}}^{-1}\boldsymbol{K}_{\mathrm{ib}} - \boldsymbol{K}_{\mathrm{ib}}^{\mathrm{T}}\boldsymbol{K}_{\mathrm{ii}}^{-1}\boldsymbol{B}_{\mathrm{ib}} + \boldsymbol{K}_{\mathrm{ib}}^{\mathrm{T}}\boldsymbol{K}_{\mathrm{ii}}^{-1}\boldsymbol{B}_{\mathrm{ii}}\boldsymbol{K}_{\mathrm{ii}}^{-1}\boldsymbol{K}_{\mathrm{ib}} \\
\boldsymbol{K}_{\mathrm{bb}}^{\mathrm{S}} &= \boldsymbol{K}_{\mathrm{bb}} - \boldsymbol{K}_{\mathrm{bi}}\boldsymbol{K}_{\mathrm{ii}}^{-1}\boldsymbol{K}_{\mathrm{ib}} \\
\boldsymbol{f}_{\mathrm{b}}^{\mathrm{S}} &= \boldsymbol{f}_{\mathrm{b}} - \boldsymbol{K}_{\mathrm{ib}}^{\mathrm{T}}\boldsymbol{K}_{\mathrm{ii}}^{-1}\boldsymbol{f}_{\mathrm{i}}
\end{aligned} \tag{5.17}$$

Next the reduced system can be formed:

$$\boldsymbol{M}_{\mathrm{CB}}\ddot{\boldsymbol{p}} + \boldsymbol{B}_{\mathrm{CB}}\dot{\boldsymbol{p}} + \boldsymbol{K}_{\mathrm{CB}}\boldsymbol{p} = \boldsymbol{f}_{\mathrm{CB}} \tag{5.18}$$

where the vector $\boldsymbol{p}$ contains the set of reduced coordinates, and is related to the full set of coordinates $\boldsymbol{q}$ via:

$$\boldsymbol{q} = \begin{bmatrix} \boldsymbol{I}_{\mathrm{bb}} & \boldsymbol{0}_{\mathrm{bk}} \\ -\boldsymbol{K}_{\mathrm{ii}}^{-1}\boldsymbol{K}_{\mathrm{ib}} & \boldsymbol{\Phi}_{\mathrm{ik}} \end{bmatrix} \boldsymbol{p} = \boldsymbol{T}_{\mathrm{CB}}\boldsymbol{p} \tag{5.19}$$

It is important to notice that when all external loads are applied to the boundary DOFs or equivalently, when the boundary DOFs are chosen in such a way to include the DOFs that are loaded with external forces, the reduced force vector becomes:

$$\boldsymbol{f}_{\mathrm{CB}} = \begin{bmatrix} \boldsymbol{f}_{\mathrm{b}} \\ \boldsymbol{0} \end{bmatrix} \tag{5.20}$$

For the weatherstrip model as shown in Figure 5.1 the FEM model has approximately 2000 degrees of freedom and this is reduced to 650 with a node displacement technique. The nodes on the top and on the bottom of the strip are used as interface nodes in the Craig-Bampton reduction which means that these nodes are present in the resulting reduced model (as explained in Section 5.1.5). All other nodes are not taken into account in the reduced model, but their dynamical behavior is represented by their modal contribution up to a selected frequency (2500 Hz in this case). The second reduction step, the balanced truncation method, can only be performed when a state-space realization of the system is available, which is the subject of Section 5.3.

5.2.1 Verification of the Craig-Bampton Reduced Model

The model reduced with the mode displacement method of Craig-Bampton should give similar results as the full model in a static case [32], such as the case described in Section 4.2, where the applicator wheel applies pressure on the top of the weatherstrip while the bottom of the strip is constrained. To verify this, a simulation is performed similar to the simulation described in Section 5.1.6; in particular, the results of the following simulation are presented:

$$\boldsymbol{K}_{\mathrm{CB}}\boldsymbol{p} = \boldsymbol{f}_{\mathrm{CB}} \tag{5.21}$$

In Figures 5.4 and 5.5 results of this simulation are shown. The resulting stress and displacement at the bottom of the strip are almost exactly the same as the results with the full model, which confirms that the Craig-Bampton reduction gives exact results for a static case. Moreover, a comparison between the eigenvalues of the full model and the Craig-Bampton reduced model (see Appendix D) reveals that the Craig-Bampton reduced model is within 1 % of the full model for all modes up to 1460 Hz, and within 10 % for all modes up to 2400 Hz.

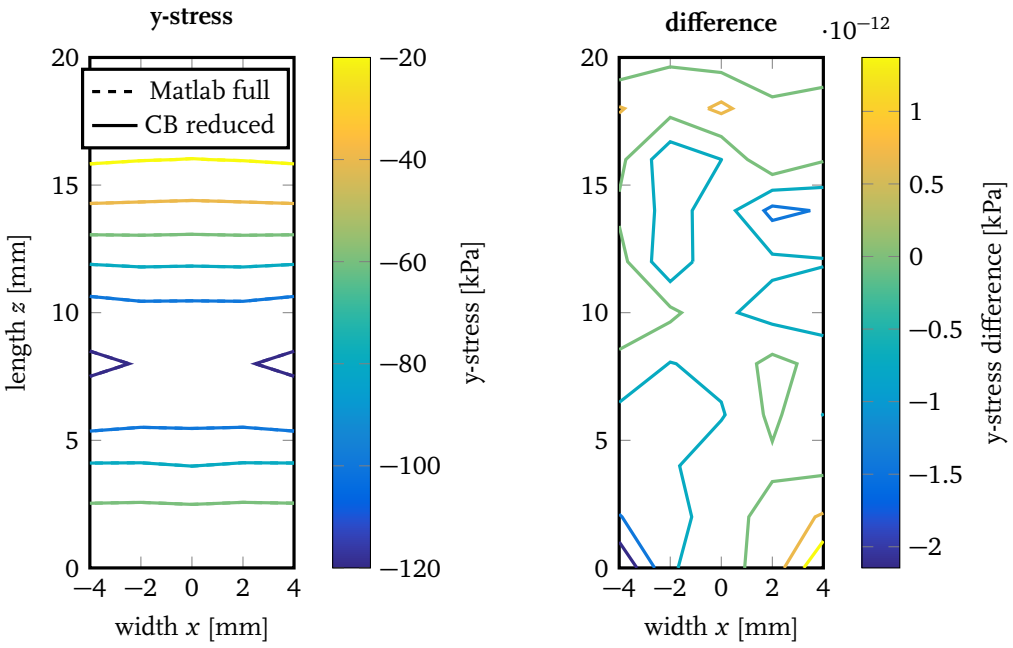

Figure 5.4: Stress distribution at the bottom of the weatherstrip: full Matlab model and Craig-Bampton reduced model on the left-hand side and the difference between these two models on the right-hand side.

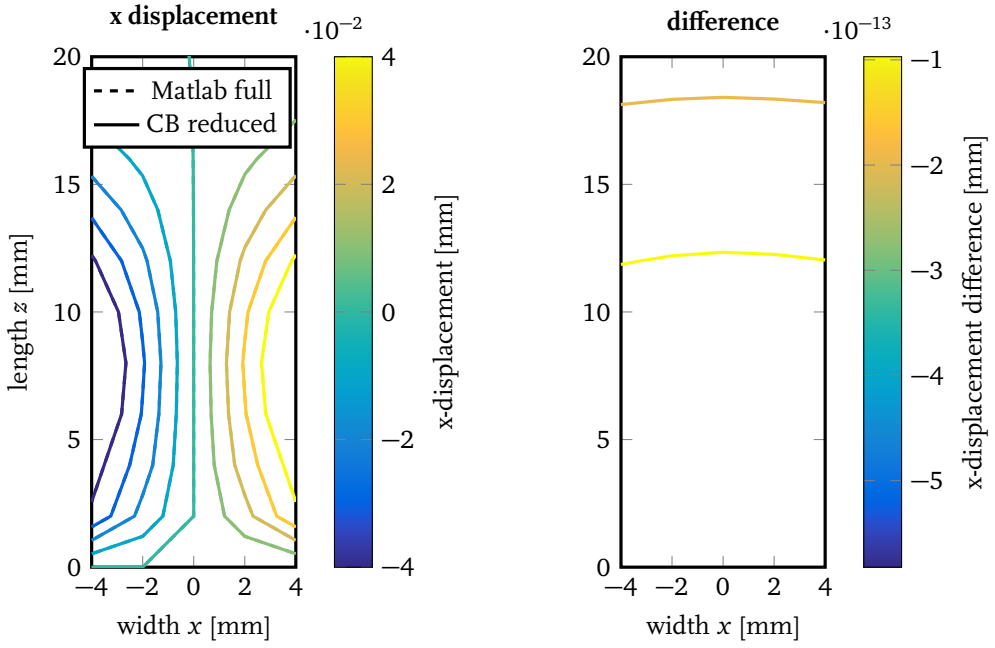

Figure 5.5: Sideways displacement at the bottom of the weatherstrip: full Matlab model and Craig-Bampton reduced model on the left-hand side and the difference between these two models on the right-hand side.

5.3 State-Space Model

The reduced system of (5.18) can be used to create a linear state-space system of the weatherstrip, as described in Section 5.1.2, but now using the reduced stiffness, damping and mass matrices:

$$\begin{aligned} \boldsymbol{F}_{\text{CB}} &= \begin{bmatrix} \boldsymbol{0} & \boldsymbol{I} \\ -\boldsymbol{M}_{\text{CB}}^{-1}\boldsymbol{K}_{\text{CB}} & -\boldsymbol{M}_{\text{CB}}^{-1}\boldsymbol{B}_{\text{CB}} \end{bmatrix}, & \boldsymbol{G}_{\text{CB}} &= \begin{bmatrix} \boldsymbol{0} \\ \boldsymbol{M}_{\text{CB}}^{-1} \end{bmatrix} \\ \boldsymbol{H}_{\text{CB}} &= \begin{bmatrix} \boldsymbol{T}_{\text{CB}} & \boldsymbol{0} \end{bmatrix}, & \boldsymbol{D}_{\text{CB}} &= \begin{bmatrix} \boldsymbol{0} \end{bmatrix} \end{aligned} \tag{5.22}$$

where $\boldsymbol{T}_{\text{CB}}$ is the transformation matrix defined in (5.19). This results in the state-space system, using the reduced coordinate vector $\boldsymbol{x}_{\text{CB}} = [\boldsymbol{p}\ \dot{\boldsymbol{p}}\ ]^{\text{T}}$:

$$\begin{aligned} \dot{\boldsymbol{x}}_{\text{CB}} &= \boldsymbol{F}_{\text{CB}}\boldsymbol{x}_{\text{CB}} + \boldsymbol{G}_{\text{CB}}\boldsymbol{f}_{\text{CB}} \\ \boldsymbol{y}_{\text{CB}} &= \boldsymbol{H}_{\text{CB}}\boldsymbol{x}_{\text{CB}} + \boldsymbol{D}_{\text{CB}}\boldsymbol{f}_{\text{CB}} \end{aligned} \tag{5.23}$$

The reduced damping matrix $\boldsymbol{B}_{\text{CB}}$ which originates from the full damping matrix $\boldsymbol{B}$ has to be included in the state-space system since that will be used for servo control simulations. The material model that is used in Chapter 4 is based on measurement data from [18]. This data does not include damping behavior, so a different source is used for the damping effects. In Chapter 3.2.2 and Appendix B, data from [45] are used to simulate visco-elastic behavior. There a damping of $d = 0.2 \approx 2\xi$ is found for a wide frequency range, this damping is implemented as proportional damping:

$$\boldsymbol{B}_{\text{CB}} = \alpha\boldsymbol{M}_{\text{CB}} + \beta\boldsymbol{K}_{\text{CB}} \tag{5.24}$$

with $\alpha = 60$ and $\beta = 3 \times 10^{-6}$.

5.3.1 Reduction with the Balanced Truncation Method

After the first step of reduction with the Craig-Bampton method in Section 5.2, the model is reduced even further with the balanced truncation method. A short overview of the balanced truncation method is given below, an in-depth review of this method can be found in [14].

Because the model of the weatherstrip is already reduced with the Craig-Bampton method, the balanced truncation reduction starts with the Craig-Bampton reduced state-space system [35, 14]:

$$\begin{aligned} \dot{\boldsymbol{x}}_{\text{CB}} &= \boldsymbol{F}_{\text{CB}}\boldsymbol{x}_{\text{CB}} + \boldsymbol{G}_{\text{CB}}\boldsymbol{f}_{\text{CB}} \\ \boldsymbol{y}_{\text{CB}} &= \boldsymbol{H}_{\text{CB}}\boldsymbol{x}_{\text{CB}} + \boldsymbol{D}_{\text{CB}}\boldsymbol{f}_{\text{CB}} \end{aligned} \tag{5.25}$$

This state-space system has a controllability Gramian $\boldsymbol{W}_{\text{c}}$ and observability Gramian $\boldsymbol{W}_{\text{o}}$. The core of the balanced truncation method is to compute a state transformation matrix $\boldsymbol{T}_{\text{BR}}$ such that the transformed controllability is equal to the transformed observability matrix:

$$\boldsymbol{W}_{\text{c,BR}} = \boldsymbol{T}_{\text{BR}}\boldsymbol{W}_{\text{c}}\boldsymbol{T}_{\text{BR}}^{\text{T}} = \boldsymbol{W}_{\text{o,BR}} = \boldsymbol{T}_{\text{BR}}\boldsymbol{W}_{\text{o}}\boldsymbol{T}_{\text{BR}}^{\text{T}} \tag{5.26}$$

These Gramians are diagonal and ordered such that the entries on the diagonal correspond to the states that are increasingly difficult to observe and control. The state-space system can be transformed without reduction into the so called *balanced realization*:

$$\begin{aligned} \dot{\boldsymbol{x}}_{\text{BR}} &= \boldsymbol{F}_{\text{BR}}\boldsymbol{x}_{\text{BR}} + \boldsymbol{G}_{\text{BR}}\boldsymbol{f}_{\text{CB}} \\ \boldsymbol{y} &= \boldsymbol{H}_{\text{BR}}\boldsymbol{x}_{\text{BR}} + \boldsymbol{D}_{\text{CB}}\boldsymbol{f}_{\text{CB}} \end{aligned} \tag{5.27}$$

with the following partitioning:

$$\begin{aligned} \boldsymbol{F}_{\mathrm{BR}} &= \boldsymbol{T}_{\mathrm{BR}} \boldsymbol{F}_{\mathrm{CB}} \boldsymbol{T}_{\mathrm{BR}}^{-1} = \begin{bmatrix} \boldsymbol{F}_{\mathrm{BT}} & \boldsymbol{F}_{12} \\ \boldsymbol{F}_{21} & \boldsymbol{F}_{22} \end{bmatrix} \\ \boldsymbol{G}_{\mathrm{BR}} &= \boldsymbol{T}_{\mathrm{BR}} \boldsymbol{G}_{\mathrm{CB}} = \begin{bmatrix} \boldsymbol{G}_{\mathrm{BT}} \\ \boldsymbol{G}_2 \end{bmatrix} \\ \boldsymbol{H}_{\mathrm{BR}} &= \boldsymbol{H}_{\mathrm{CB}} \boldsymbol{T}_{\mathrm{BR}}^{-1} = \begin{bmatrix} \boldsymbol{H}_{\mathrm{BT}} & \boldsymbol{H}_2 \end{bmatrix} \\ \boldsymbol{x}_{\mathrm{BR}} &= \boldsymbol{T}_{\mathrm{BR}} \boldsymbol{x}_{\mathrm{CB}} = \begin{bmatrix} \boldsymbol{x}_{\mathrm{BT}} \\ \boldsymbol{x}_2 \end{bmatrix} \end{aligned} \tag{5.28}$$

The reduced system can now be written as:

$$\begin{aligned} \dot{\boldsymbol{x}}_{\mathrm{BT}} &= \boldsymbol{F}_{\mathrm{BT}} \boldsymbol{x}_{\mathrm{BT}} + \boldsymbol{G}_{\mathrm{BT}} \boldsymbol{f}_{\mathrm{CB}} \\ \boldsymbol{y}_{\mathrm{BT}} &= \boldsymbol{H}_{\mathrm{BT}} \boldsymbol{x}_{\mathrm{BT}} + \boldsymbol{D}_{\mathrm{CB}} \boldsymbol{f}_{\mathrm{CB}} \end{aligned} \tag{5.29}$$

Here only the states that contribute significantly to the input-output behavior of the system are included, the other states are truncated. This has as consequence that the static gain of high frequency modes is not present in the behavior of the reduced system. Simulations with the above model can significantly deviate from the linear FEM model of Section 5.1.6. To overcome this issue, the so called *matched dc* reduction method is used [27]. This method is an extension to the balanced truncation method and uses the balanced realization of a system (5.27):

$$\begin{aligned} \dot{\boldsymbol{x}}_{\mathrm{DC}} &= \boldsymbol{F}_{\mathrm{DC}} \boldsymbol{x}_{\mathrm{DC}} + \boldsymbol{G}_{\mathrm{DC}} \boldsymbol{f}_{\mathrm{CB}} \\ \boldsymbol{y}_{\mathrm{DC}} &= \boldsymbol{H}_{\mathrm{DC}} \boldsymbol{x}_{\mathrm{DC}} + \boldsymbol{D}_{\mathrm{DC}} \boldsymbol{f}_{\mathrm{CB}} \end{aligned} \tag{5.30}$$

where the system matrices are given as:

$$\begin{aligned} \boldsymbol{F}_{\mathrm{DC}} &= \begin{bmatrix} \boldsymbol{F}_{\mathrm{BT}} - \boldsymbol{F}_{12} \boldsymbol{F}_{22}^{-1} \boldsymbol{F}_{21} \end{bmatrix} \\ \boldsymbol{G}_{\mathrm{DC}} &= \begin{bmatrix} \boldsymbol{G}_{\mathrm{BT}} - \boldsymbol{F}_{12} \boldsymbol{F}_{22}^{-1} \boldsymbol{G}_2 \end{bmatrix} \\ \boldsymbol{H}_{\mathrm{DC}} &= \begin{bmatrix} \boldsymbol{H}_{\mathrm{BT}} - \boldsymbol{H}_2 \boldsymbol{F}_{22}^{-1} \boldsymbol{F}_{21} \end{bmatrix} \\ \boldsymbol{D}_{\mathrm{DC}} &= \begin{bmatrix} \boldsymbol{D}_{\mathrm{CB}} - \boldsymbol{H}_2 \boldsymbol{F}_{22}^{-1} \boldsymbol{G}_2 \end{bmatrix} \end{aligned} \tag{5.31}$$

Here, the static contribution of the truncated modes is included in the system matrices of the reduced system. Interesting to notice is that while the $\boldsymbol{D}$ matrices are empty (equal to zero) for the full system, the Craig-Bampton reduced system and the balanced truncated system, the matched dc reduced system has a nonzero D matrix.

The weatherstrip state-space model is reduced with this method in Matlab (`balreal` and `modred` in Matlab) to a state-space model with 250 states. The nodes on the top of the weatherstrip are used as the inputs and outputs for the balanced truncation method, while the bottom nodes are only used as the outputs.

5.3.2 Verification of the Balanced Truncation Reduced Model

A simulation with the balanced truncation (matched dc) reduced model is performed, which is comparable to the simulation described in Section 5.1.6; in particular an applicator wheel applies pressure at the top of the weatherstrip while the bottom of the strip is constrained. In mathematical terms, the system of (5.30) is simulated until the transient behavior dies out:

$$\begin{aligned} \boldsymbol{0} &= \boldsymbol{F}_{\mathrm{DC}} \boldsymbol{x}_{\mathrm{DC}} + \boldsymbol{G}_{\mathrm{DC}} \boldsymbol{f}_{\mathrm{CB}} \\ \boldsymbol{y}_{\mathrm{DC}} &= \boldsymbol{H}_{\mathrm{DC}} \boldsymbol{x}_{\mathrm{DC}} + \boldsymbol{D}_{\mathrm{DC}} \boldsymbol{f}_{\mathrm{CB}} \end{aligned} \tag{5.32}$$

The results are shown in Figures 5.6 and 5.7. These figures show that the balanced truncated model shows good agreement with the full model for both the stress and the sideways displacement at the bottom of the weatherstrip. Moreover, the natural frequencies of this reduced model have perfect agreement with the Craig-Bampton reduced model (see Appendix D) and good agreement with the full model up to 2400 Hz. It can be concluded that the state-space model first reduced with the Craig-Bampton method and then further reduced with the balanced truncation method gives statically satisfactory results and can be used for servo control simulations.

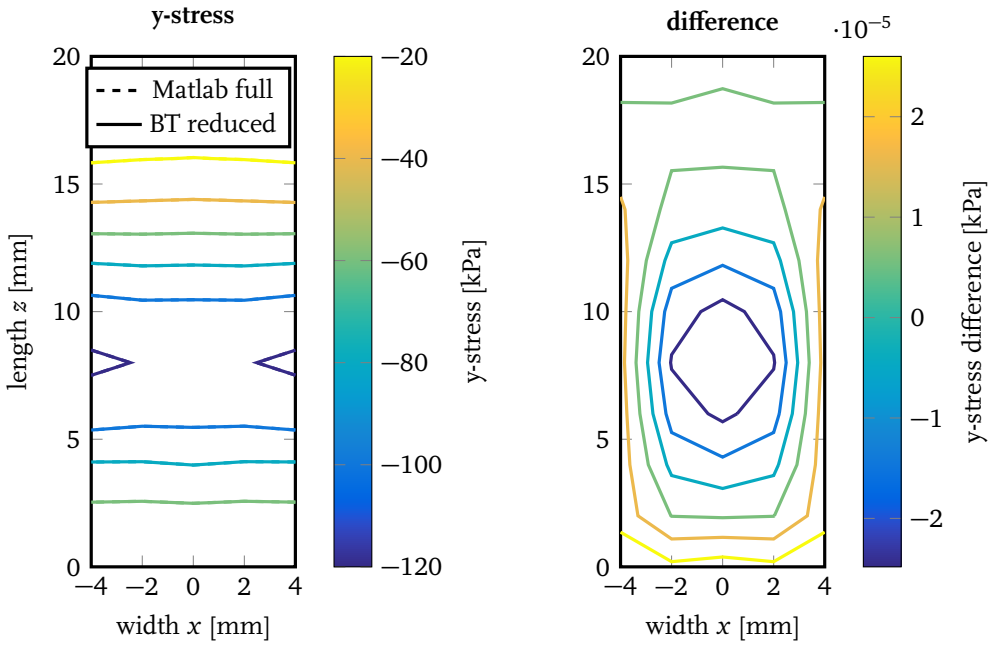

Figure 5.6: Stress distribution at the bottom of the weatherstrip: full Matlab model and balanced truncation reduced model on the left-hand side and the difference between these two models on the right-hand side.

5.4 Input and Output Mapping for Robot Interaction

The full weatherstrip model in Matlab (5.10) has all degrees of freedom available for interaction. The reduced models (both Craig-Bampton and balanced truncation) only have their boundary nodes as defined by (5.12) available for interaction. The boundary nodes chosen in this case are the nodes at the bottom and the nodes at the top of the strip (see Figure 5.1). The nodes at the top will interact with the end-effector of the robot in the servo simulations. The end-effector, however, has only six degrees of freedom (x, y, z, R_x, R_y, R_z) available to interact with the weatherstrip. As defined in Figure 5.1 two main directions of interaction between the end-effector and the weatherstrip are y and z. Along the y direction (height of the strip), the desired contact force between the weatherstrip and the substrate has to be achieved. Hence, the robot end-effector has to supply force Fy to the applicator which is in contact to the weatherstrip, such as to achieve the desired contact force. Since the applicator needs to ensure the desired contact along the complete length of the strip, the end-effector has to control motion of the applicator in the z direction. To be able to model interaction between the end-effector and the weatherstrip in a realistic way, a mapping needs to be created between the force

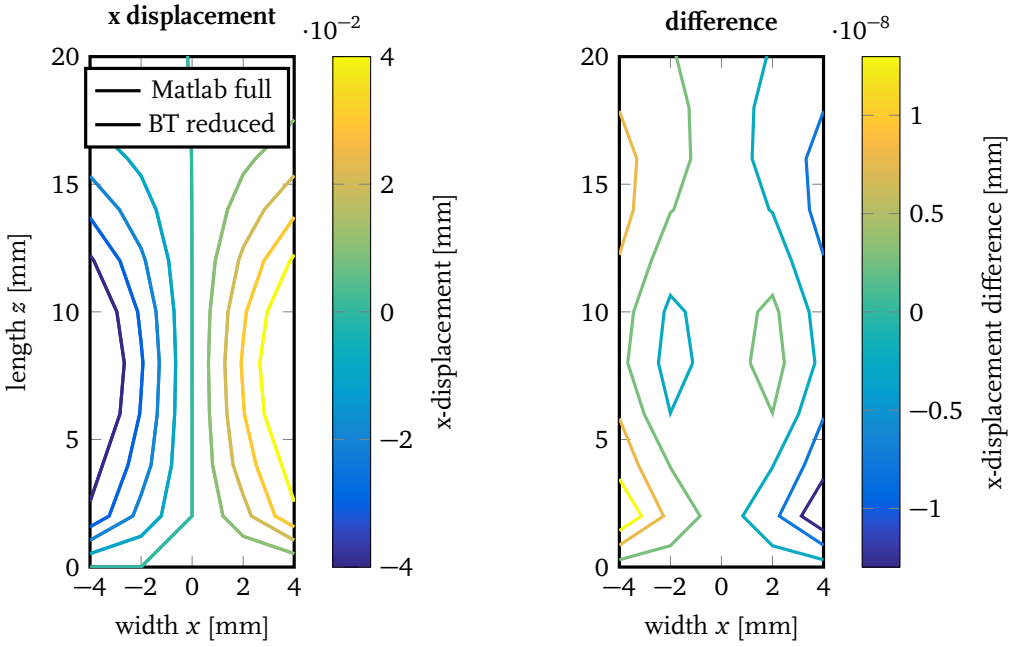

Figure 5.7: Sideways displacement at the bottom of the weatherstrip: full Matlab model and balanced truncation reduced model on the left-hand side and the difference between these two models on the right-hand side.

F_y and z-motion of the end effector, on one hand, and the 100+ degrees of freedom at the top of the weatherstrip, on another.

Within the ANSYS FEM software, sophisticated algorithms are present to model contact between the bodies. These capabilities are used for the FEM simulations described in Chapter 4, where an applicator wheel is pressed onto the top of the weatherstrip. ANSYS computes the area of contact between the wheel and the strip and also computes the contact forces acting on the nodes of the strip. These forces represent the force that the applicator wheel exerts on each node of the weatherstrip model for a certain (F_y, z) configuration of the end-effector.

In Matlab, a two-dimensional Gauss curve is used to map the force F_y of the end-effector to forces acting on the top nodes of the weatherstrip. It is fitted trough the ANSYS reaction forces as follows:

$$F_e(x, z, z_a) = d\, e^{-ax^2 - 2bx(z-z_a) - c(z-z_a)^2} \tag{5.33}$$

where x is the location of a node in x direction, z is the location of a node in z direction, z_a is the location of the applicator wheel in z direction and a, b, c, d are the constants used to shape the curve:

$$\begin{aligned} a &= 0.424 \\ b &= 2.403 \times 10^{-6} \\ c &= 0.123 \\ d &= 2.604 \end{aligned} \tag{5.34}$$

These constants are determined by fitting the function (5.33) to the reaction forces calculated in ANSYS. The resulting contact force for $z_a = 8$ is shown in Figure 5.8. The forces in this contour plot sum to a total of 10 N, which is equal to the force on the applicator wheel as described in Section 4.2. This force distribution can be linearly scaled to enable small deviations from the mean.

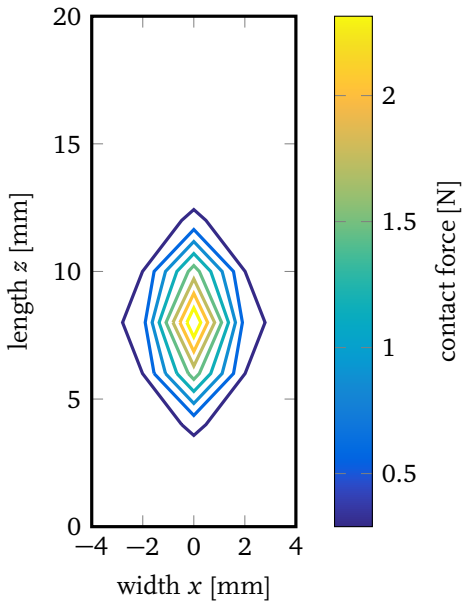

Figure 5.8: Contact force at the top of the strip due to applicator pressure.

When the force is applied onto the weatherstrip with the distribution shown in Figure 5.8, the resulting stress in the y-direction and displacement in the x-direction at the bottom of the weatherstrip are shown in Figures 5.9 and 5.10, respectively. From these figures it is clear that the results are still within a few percent difference compared with the full linear Matlab model. It can thus be concluded that the linear balanced truncated reduced model together with the input force mapping shown in Figure 5.8 can be used to represent the weatherstrip and applicator wheel in servo simulations.

5.5 Conclusion

In this chapter a linear state-space model of the weatherstrip is created, this linear state-space model shows good agreement with the finite element model. Two model order reduction techniques are used to reduce the number of states in the state-space model while keeping good agreement with the original full model. An input and output mapping for force interaction is made to facilitate the interaction between the applicator wheel and the weatherstrip in the next chapter.

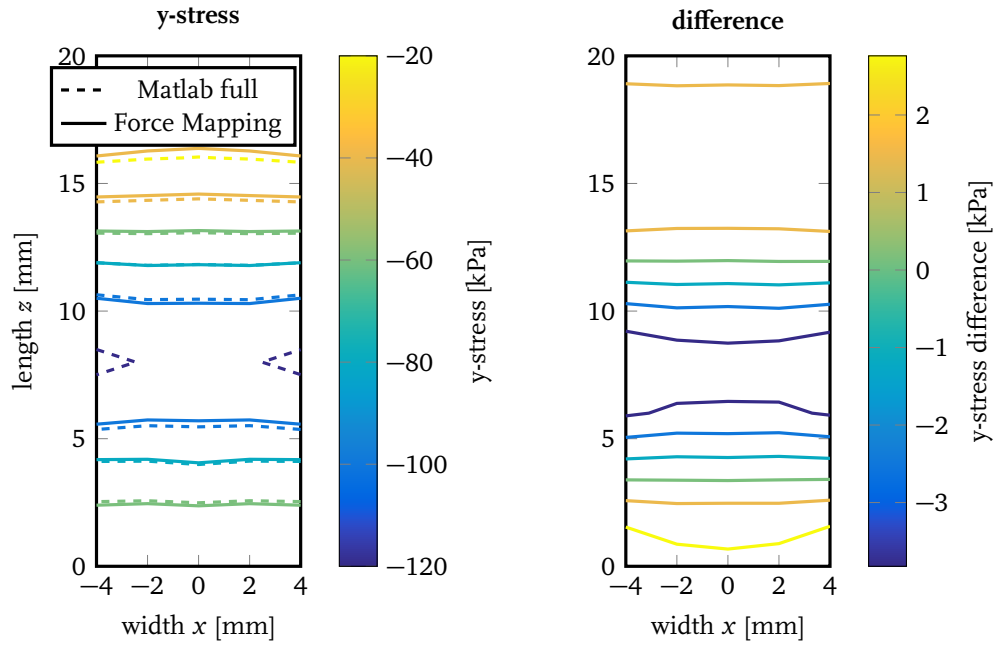

Figure 5.9: Stress distribution at the bottom of the weatherstrip: full Matlab model and balanced truncation reduced model with input force mapping on the left-hand side and the difference between these two models on the right-hand side.

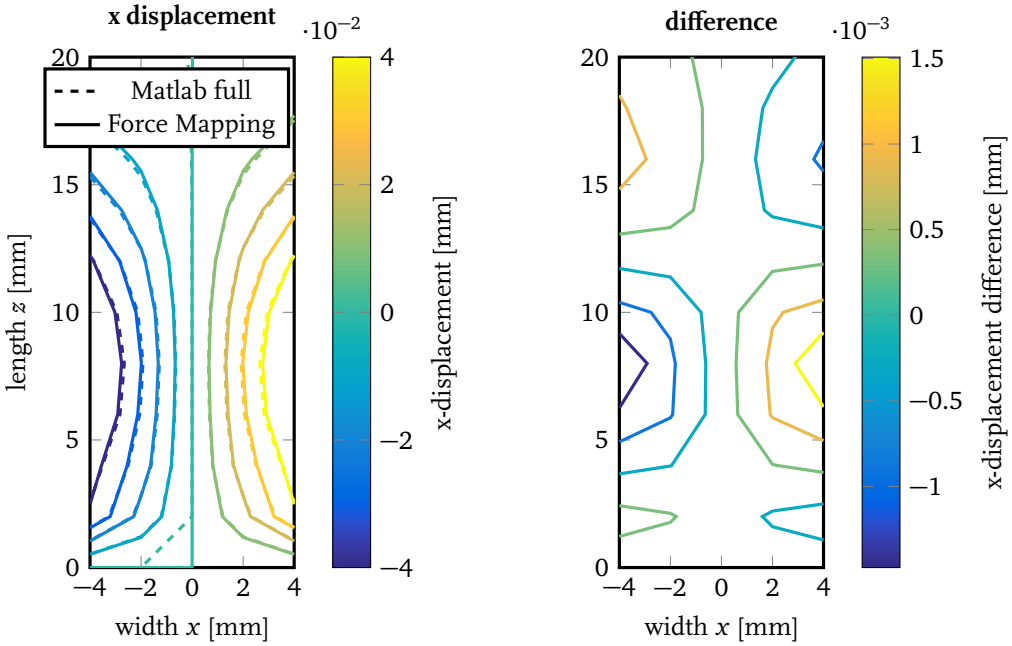

Figure 5.10: Displacement in x-direction at the bottom of the weatherstrip: full Matlab model and balanced truncation reduced model with input force mapping on the left-hand side and the difference between these two models on the right-hand side.

Chapter 6

Control Design for Automated Sealing

In the previous chapters, it is shown that to apply the weatherstrip correctly it is necessary to apply the right amount of force onto the strip. The state-space model developed in Chapter 5 can be used to investigate the stress and deformation at the bottom of the weatherstrip under a force distribution applied on the top of the strip. In this chapter a controller is designed for the applicator wheel to regulate the sealing force and motion for this device. In general, this controller has to regulate six degrees of freedom, since the surface to mount the strip onto can be a three dimensional surface. Regarding the six degrees of freedom, the force is controlled in the directions that are perpendicular with respect to the mounting surface, while motion control takes place in the remaining directions. In this project control design is performed in world space, that is, in Cartesian and angular coordinates. Orthogonality of these coordinates allows for design of motion and force controllers for each DOF independently. In this chapter, force control design is considered for one degree of freedom only. This force controller will be incorporated into the motion/force controller for a robot with six degrees of freedom in Chapter 7.

6.1 Hybrid Impedance Control

There exist a lot of different force control implementations in literature, an overview of some of these algorithms can be found in [11]. There it is argued that *impedance force control* is suited for situations where a motion trajectory needs to be followed before contact with the environment is made and force control starts. Moreover, a *hybrid impedance force control* algorithm [54, 62] gives the designer the opportunity to explicitly split the control design into a separate force and motion part. Hence, the hybrid impedance force controller seems suitable to use in the process of weatherstrip application.

The behavior of the weatherstrip is assumed to be dominated by capacitive effects, that is, by its stiffness. For the case of force control, the applicator wheel can be considered as a point mass m_w which moves in one degree of freedom, denoted by x_w. The applicator wheel is in contact with the top of the weatherstrip, whose position is denoted with x_s and which has a stiffness of k_s. This leads to the following system:

$$m_w \ddot{x}_w + k_s x_s = u \tag{6.1}$$

where, due to contact, $x_w = x_s$. The force $F_e = k_s x_s$ is the contact force between the wheel and the top of the strip, it is assumed that this force can be measured. The control force acting on the applicator

is denoted by u. When the control force is chosen as:

$$\begin{aligned} u &= m_w a_x + a_f \\ a_x &= \frac{1}{m_d}(F_r - F_e) - \frac{1}{m_d} b_d \dot{x}_w \end{aligned} \tag{6.2}$$

where

$$a_f = F_e$$

with m_d and b_d representing the desired mass and damping of the resulting system respectively, and F_r the reference force, the resulting system can be written as:

$$\begin{aligned} m_w \ddot{x}_w + F_e &= \frac{m_w}{m_d}(F_r - F_e) - \frac{m_w}{m_d} b_d \dot{x}_w + F_e \\ m_d \ddot{x}_w + b_d \dot{x}_w &= F_r - F_e \end{aligned} \tag{6.3}$$

This controller has the effect that when the system is at equilibrium ($\ddot{x}_w = 0$ and $\dot{x}_w = 0$), the contact force between the wheel and the top of the strip becomes equal to the reference force. On top of that, the controlled system behaves like a second order system with the desired mass and damping properties:

$$m_d \ddot{x}_w + b_d \dot{x}_w + k_s x_w = F_r \tag{6.4}$$

since the external force is given by $F_e = k_s x_w$. This means that it is possible to set the desired behavior in terms of natural frequency and damping, and achieve the desired contact force.

6.2 Performance of 1 DOF System

In this section it is explained how to tune the gains of the hybrid impedance control law (6.4). For that purpose the block-diagram in Figure 6.1 is considered, where the block labeled $P(s)$ describes the applicator wheel and weatherstrip. The plant dynamics $P(s)$ in Laplace domain is determined by linearization of the weatherstrip model, including force interaction mapping, in Simulink.

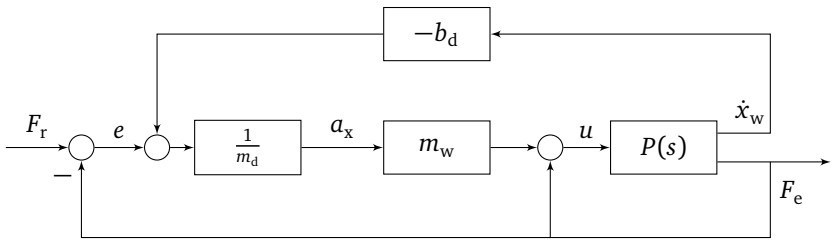

Figure 6.1: Block-diagram of the controlled 1DOF system. The controlled process is located in $P(s)$.

In Figure 6.2 Bode plots are shown for the plant, for the plant with velocity feedback and for the open-loop gain. The open-loop gain in this case is the open loop from e to F_e in Figure 6.1. This figure shows that the open-loop crossover frequency occurs at 25 Hz with a phase margin of 90°. This relatively low crossover frequency is chosen to have enough robustness against parameter variations and effects of nonlinear behavior of the six degrees of freedom robot.

Bode plots of the sensitivity and complementary sensitivity functions, defined as $S = \frac{e}{F_r}$ and $T = \frac{F_e}{F_r}$, respectively, are shown in Figure 6.3. By inspection of this figure, it can be noticed that

the resulting controller enables tracking of the desired application force F_r up to 30 Hz, and a good disturbance rejection up to 20 Hz. Also, the peak in the sensitivity plot S is well below 6 dB, which indicates robustness to parameter variations and model inaccuracies.

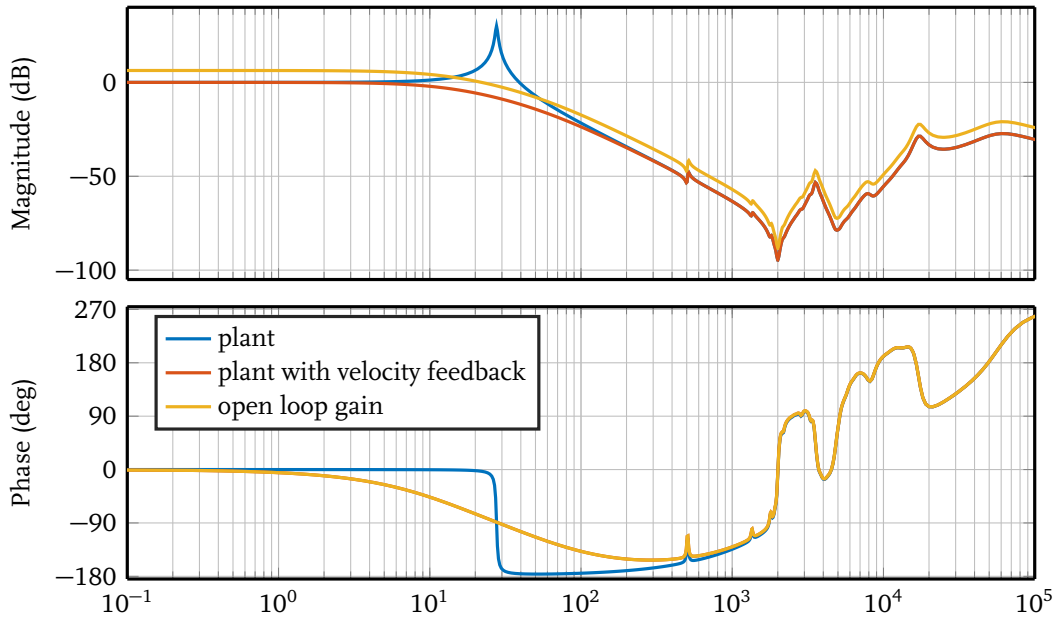

Figure 6.2: Bode diagram of the plant, plant with velocity feedback and the open loop gain, that is the plant with velocity feedback and the gain for force control included

6.3 Implementation

To enable servo simulations of the system consisting of the applicator wheel and weatherstrip a Simulink model is created. The weatherstrip is modeled with the balanced truncated state-space system method described in Chapter 5. In this case the weatherstrip is not modeled as a completely straight strip, since that would not pose a challenge for the control system. To make the control problem more challenging the weatherstrip is modeled with a small bulge in the middle of the strip, representing an unknown deformation of the substrate. In Figure 6.4 the displacements are shown of the bottom and top nodes of the lengthwise cross section (the $z-y$ plane at $x = 0$) of the weatherstrip due to the deformation of the substrate. These deformations are given as a function of the strip length. In Figure 6.5 the state-space model of the weatherstrip with bulge is shown. The node displacement due to the substrate deformation is bigger at the bottom of the strip compared with the top of the strip. This poses a challenge for the force controlled robot, since it now has to cope with a surface that is not flat, and therefore, it has to change the height of the applicator wheel in order to maintain the desired application force.

6.4 1 DOF Servo Simulation

A servo simulation of the one-degree of freedom system is performed that incorporates the moving mass (applicator wheel), the weatherstrip state-space model, the interaction forces, and the motion/-

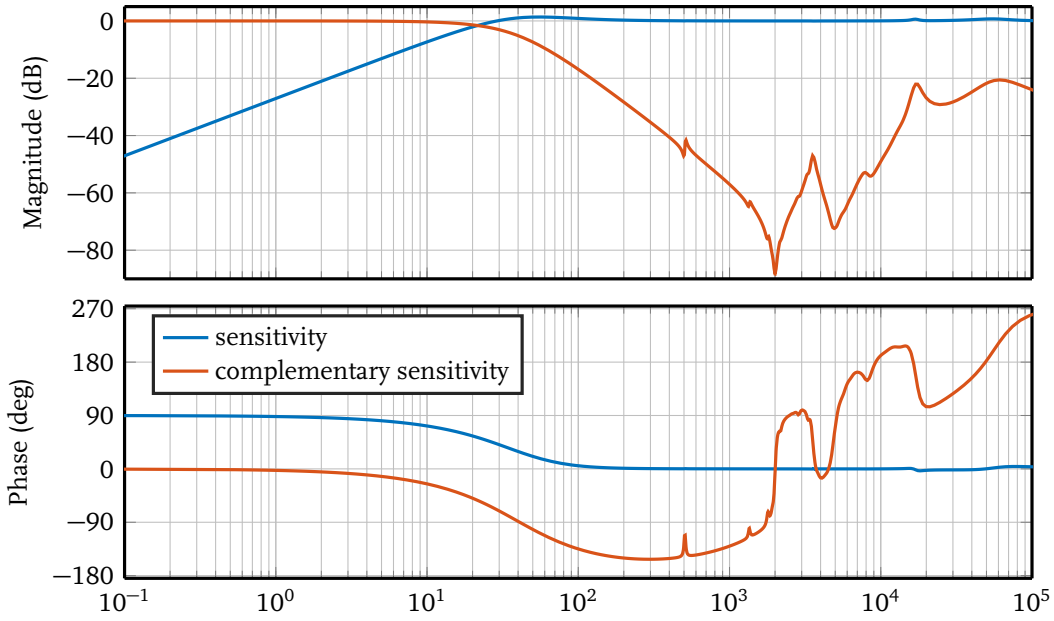

Figure 6.3: Sensitivity S and complementary sensitivity T

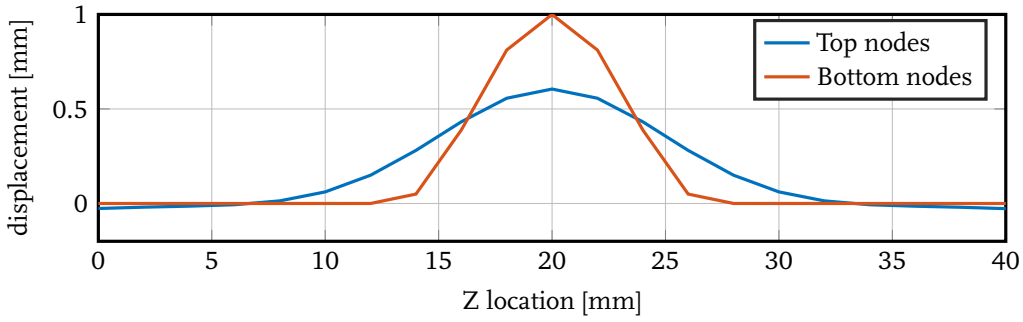

Figure 6.4: Displacement of top and bottom nodes as result of substrate deformation

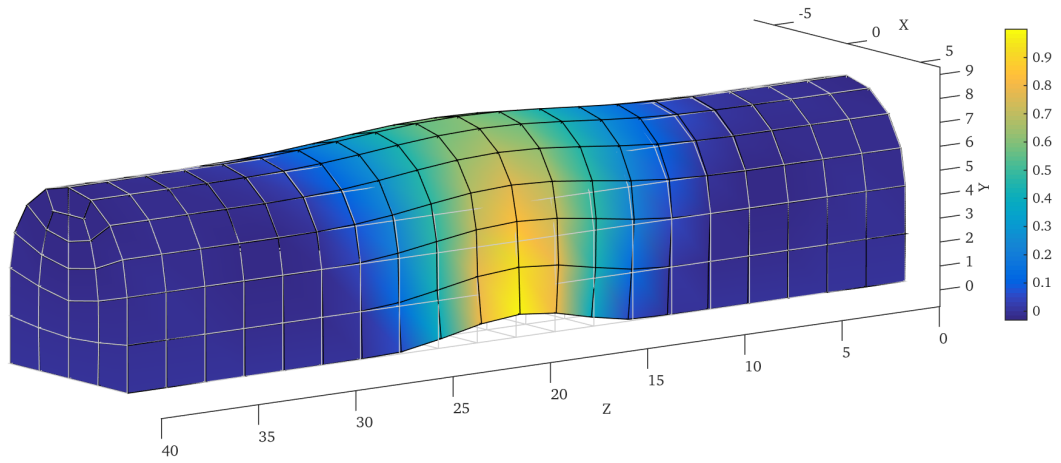

Figure 6.5: Weatherstrip state-space model with bulge

force controller. The reference motion and force profiles for this simulation are shown in Figure 6.6; here the total reference motion of the applicator in the z—direction (lengthwise) of the weatherstrip is depicted in the topmost figure. The starting position is at 2 mm and the final position is at 38 mm. The second figure depicts the reference cosine velocity profile and the third figure depicts the reference acceleration profile. The bottom figure shows the reference force profile for the desired application force.

The desired force of -10 N is the same as the application force used in the FEM simulations in Chapter 4, and the Matlab simulations in Chapter 5.

The achieved contact force at the bottom of the weatherstrip in this simulation is shown in Figure 6.7. Here, the setpoint force is depicted in blue and the realized contact force is shown in red. It can be seen that the maximum force error does not exceed 0.45 N, despite the presence of the bulge in the weatherstrip. The control law of (7.7) does not include integral action, which explains why the force error does not asymptotically converge to zero.

6.5 Conclusion

A force controller is designed for the 1-dimensional system including the linear state-space model of the weatherstrip and the applicator wheel. This force controller has good robustness margins and is able to track signals up to 20 Hz and to attenuate disturbances up to 30 Hz. A time domain simulation with a challenging weatherstrip profile shows that the controller can achieve the desired contact force within reasonable error bounds.

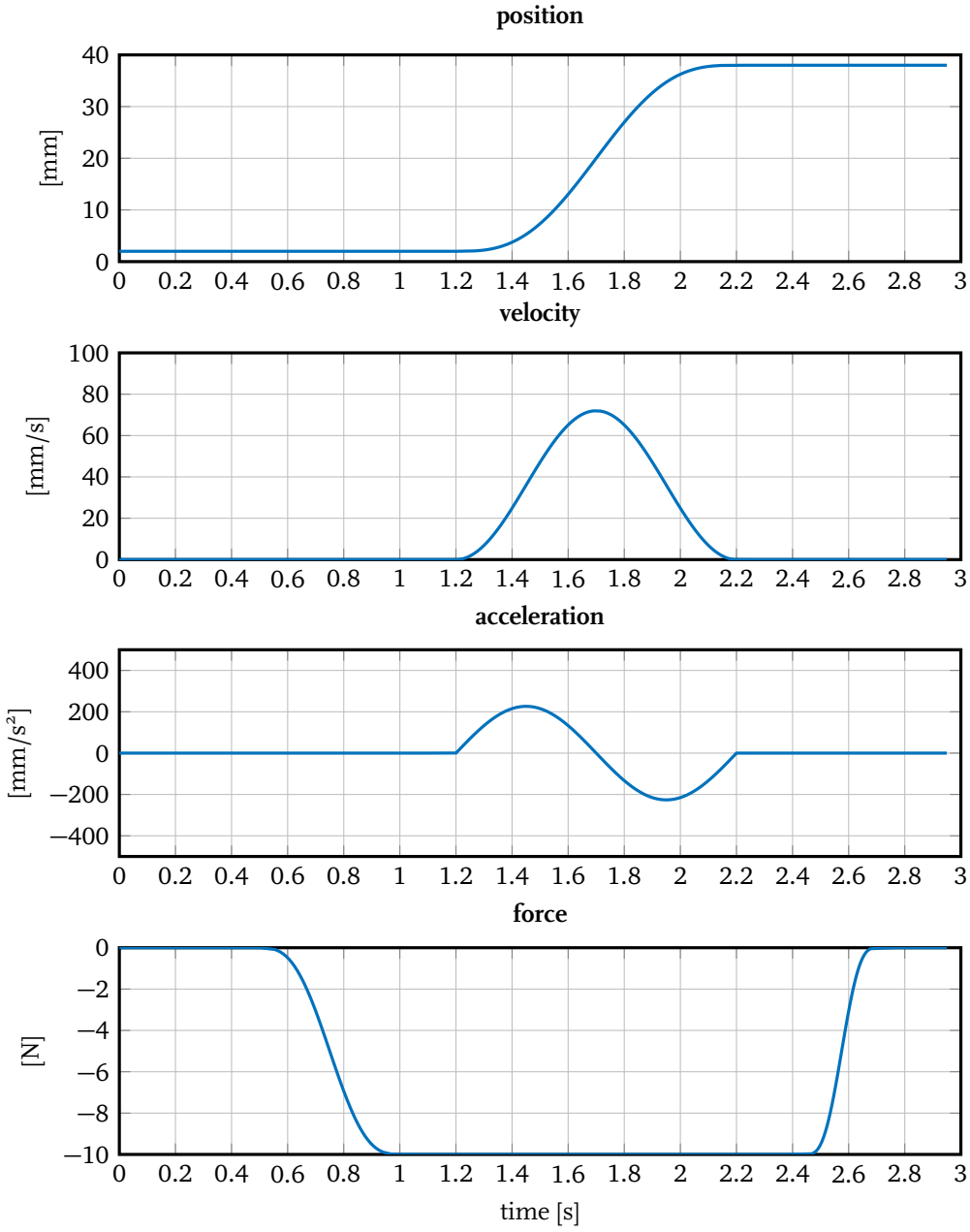

Figure 6.6: The reference motion and force trajectories for the applicator wheel

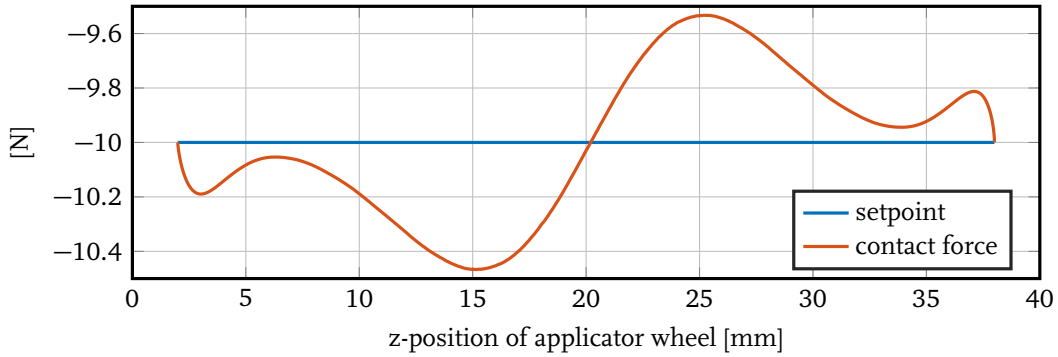

Figure 6.7: Force setpoint and realized contact force on the bottom of the weatherstrip with respect to the z-position of the applicator wheel.

Chapter 7

Control Design and Simulation of Robotized Sealing Process

7.1 Robot Kinematics

To investigate feasibility of the robotized sealing process, the ABB IRB 2400 robot is chosen. A visualization of this robot can be found in Appendix E. This six degrees of freedom robot is typically used in automotive applications and has appropriate dimensions, speed and reach to perform the process of weatherstrip assembly. The dimensions of this robot are retrieved from the CAD files supplied by ABB [3]. The Denavit-Hartenberg parameters for this robot are given in Table 7.1. These parameters are used, together with the inertial parameters given in the next section, to create a SimMechanics model of the robot.

Table 7.1: DH parameters for ABB IRB 2400 robot

Link	θ	d	a	α
1	θ_1	0.615	0.1	$-\frac{1}{2}\pi$
2	θ_2	0	0.705	0
3	θ_3	0	0.135	$-\frac{1}{2}\pi$
4	θ_4	0.755	0	$\frac{1}{2}\pi$
5	θ_5	0	0	$-\frac{1}{2}\pi$
6	θ_6	0.085	0	0

7.2 Robot Dynamics

The mass and inertial parameters of the ABB IRB 2400 robot are computed from the CAD data [3] of the robot, and can be found in Appendix E. These inertial parameters are used in the model of the robot and also in the inverse dynamics control law which is described in section 7.3.1

The dynamics of the 6DOF robot can be written as follows [54, 62]:

$$\boldsymbol{M}(\boldsymbol{q})\ddot{\boldsymbol{q}} + \boldsymbol{C}(\boldsymbol{q},\dot{\boldsymbol{q}})\dot{\boldsymbol{q}} + \boldsymbol{g}(\boldsymbol{q}) + \boldsymbol{J}^T(\boldsymbol{q})\boldsymbol{F}_e = \boldsymbol{\tau} \tag{7.1}$$

where $\boldsymbol{M}$ is the 6×6 inertia matrix, $\boldsymbol{C}\dot{\boldsymbol{q}}$ is the 6-dimensional vector of Coriolis and centripetal effects, $\boldsymbol{g}$ is the 6×1 vector of gravity effects, $\boldsymbol{J}^T\boldsymbol{F}_e$ is the 6×1 vector containing joint torques resulting from

external forces and moments represented by the 6 vector $\boldsymbol{F}_{\mathrm{e}}$. $\boldsymbol{J}$ is the 6×6 Jacobian matrix of the robot and $\boldsymbol{\tau}$ is the 6×1 vector of joint torques.

The vector $\boldsymbol{F}_{\mathrm{e}}$ describes the force that the robot applies to the applicator wheel; it is assumed that $\boldsymbol{F}_{\mathrm{e}}$ can be measured. This force has also to be regulated during application of the weatherstrip to the substrate.

7.3 Task Space Inverse Dynamics Control Law

To achieve the desired interaction force $\boldsymbol{F}_{\mathrm{e}}$ in the task space of the robot, the joint torques $\boldsymbol{\tau}$ have to be controlled. The control law for $\boldsymbol{\tau}$ is developed in three steps; first an inverse dynamics controller is designed in the joint space, then a conversion to the task space is performed, and finally an impedance force controller is designed to regulate the interaction force.

7.3.1 Inverse Dynamics Controller

The inverse dynamics controller is designed to compensate for the nonlinearities in the robot dynamics (7.1) such as to achive a so-called *double integrator system*. This is done by the following control law in the space of joint torques:

$$\boldsymbol{\tau} = \boldsymbol{M}(\boldsymbol{q})\boldsymbol{a}_{\mathrm{q}} + \boldsymbol{C}(\boldsymbol{q}, \dot{\boldsymbol{q}})\dot{\boldsymbol{q}} + \boldsymbol{g}(\boldsymbol{q}) + \boldsymbol{J}^{T}(\boldsymbol{q})\boldsymbol{F}_{\mathrm{e}} \tag{7.2}$$

Application of (7.2) to (7.1) leads to the system:

$$\ddot{\boldsymbol{q}} = \boldsymbol{a}_{\mathrm{q}} \tag{7.3}$$

where $\boldsymbol{a}_{\mathrm{q}}$ is the vector of control laws for the accelerations in the robot joints.

Joint accelerations are determined based on the reference motion of the applicator manipulated by the robot arm together with the desired forces of interaction between the applicator and the weatherstrip. This can be achieved by using the Jacobian $\boldsymbol{J}$, which relates the task space velocities $\dot{\boldsymbol{x}}$ to the joint velocities $\dot{\boldsymbol{q}}$:

$$\dot{\boldsymbol{x}} = \boldsymbol{J}(\boldsymbol{q})\dot{\boldsymbol{q}} \tag{7.4}$$

From (7.4) the following relation is determined between task space accelerations and accelerations in the robot joints:

$$\ddot{\boldsymbol{x}} = \boldsymbol{J}(\boldsymbol{q})\ddot{\boldsymbol{q}} + \dot{\boldsymbol{J}}(\boldsymbol{q})\dot{\boldsymbol{q}} \tag{7.5}$$

This relation can be used to compute the control in the joint space signals $\boldsymbol{a}_{\mathrm{q}}$ based on the corresponding control signals for the task space accelerations $\boldsymbol{a}_{\mathrm{x}}$:

$$\boldsymbol{a}_{\mathrm{q}} = \boldsymbol{J}^{-1}(\boldsymbol{q})\left\{\boldsymbol{a}_{\mathrm{x}} - \dot{\boldsymbol{J}}(\boldsymbol{q})\dot{\boldsymbol{q}}\right\} \tag{7.6}$$

7.3.2 Task Space Control Laws

In the task space the control law concerns elements of vector $\boldsymbol{a}_{\mathrm{x}} = [a_{\mathrm{x}}\, a_{\mathrm{y}}\, a_{\mathrm{z}}\, a_{\mathrm{R_x}}\, a_{\mathrm{R_y}}\, a_{\mathrm{R_z}}]^{T}$. This vector contains decoupled control laws for six degrees of freedom of the applicator manipulated by the robot arm. In Section 5.4 and Chapter 6, it is argued that the motion of applicator handled by the robot end-effector needs to be controlled in the x, z, R_x, R_y, R_z directions, while the y-direction is force

controlled. In the y-direction the hybrid impedance force control algorithm described in Chapter 6 is used:

$$a_y = \frac{m_w}{m_d}(F_r - F_e) - \frac{m_w}{m_d} b_d \dot{y}_w \tag{7.7}$$

where a_y is the second element of $\boldsymbol{a}_x$, m_w is the mass of the applicator wheel attached to the robot, m_d and b_d are the desired mass and damping of the resulting system respectively, F_r is the reference application force, F_e is the measured interaction force and $\dot{y}_w$ is the velocity of the applicator wheel in the Cartesian y-direction.

The five end-effector motions can be controlled with standard PD feedback controllers using the reference accelerations as the feedforward signals:

$$a_c = k_p(c_{ref} - c) + k_d(\dot{c}_{ref} - \dot{c}) \tag{7.8}$$

for coordinates $c = x, z, R_x, R_y, R_z$.

7.4 6DOF Servo Simulation

The robot described in Section 7.1 is implemented in SimMechanics and combined with the reduced state-space weatherstrip model, force mapping and control laws, to enable servo simulations. A block diagram of the simulated model is shown in Figure 7.1, where $\boldsymbol{F}_{ref}$, $\boldsymbol{X}_{ref}$ and $\dot{\boldsymbol{X}}_{ref}$ are the reference force and position signals respectively. The block labeled *controller* represents the implementation of the control laws (7.7) and (7.8). The block labeled *taskspace to jointspace* represents the implementation of (7.6), the block labeled *inverse dynamics* is the implementation of (7.2). The block labeled *plant* is the implementation of the six degrees of freedom robot, the applicator wheel, the force interaction mapping and the linear state-space model of the weatherstrip. The joint coordinates $\boldsymbol{q}$ and velocities $\dot{\boldsymbol{q}}$ are fed back to the *forward kinematics* block to be used to compute the world space coordinates and velocities denoted by $\boldsymbol{X}$ and $\dot{\boldsymbol{X}}$, respectively. The force $\boldsymbol{F}_{e,q}$ is the interaction force measured in end-effector coordinates, and is transformed into the force $\boldsymbol{F}_e$, which is defined in world coordinates.

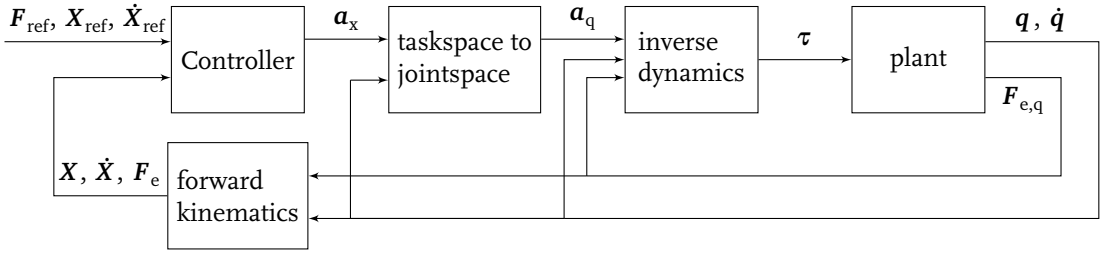

Figure 7.1: Block diagram of the implementation of the servo simulation setup containing the control laws for force and motion. The six degrees of freedom robot and the weatherstrip are represented by the *plant* block.

The weatherstrip has the same bulge as described in Section 6.3 and the reference motion and force profiles for the applicator are the same as the ones described in Section 6.4. A servo simulation of the robot system with force mapping and state-space weatherstrip model is performed, and the resulting contact force can be seen in Figure 7.2. It can be seen that the achieved contact force is similar to that of the one-dimensional case shown in Figure 6.7. The maximum force error does not exceed 0.45 N, but due to the absence of integral action in the controller, the force error does not asymptotically go to zero.

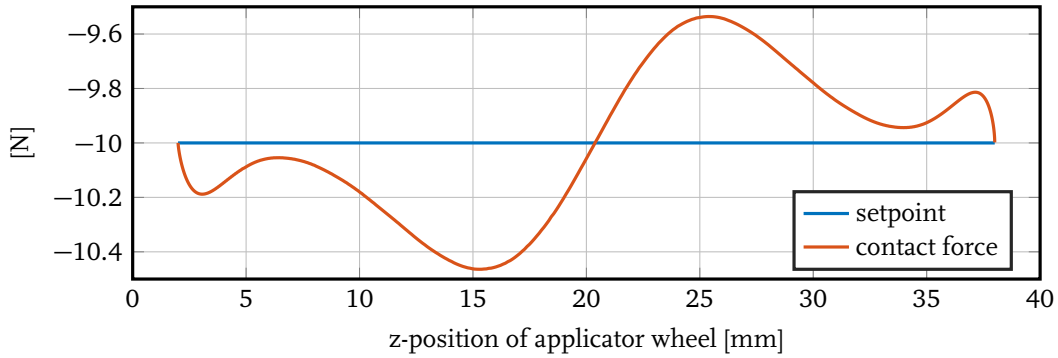

Figure 7.2: Force setpoint and realized contact force on the bottom of the weatherstrip with respect to the z-position of the applicator wheel.

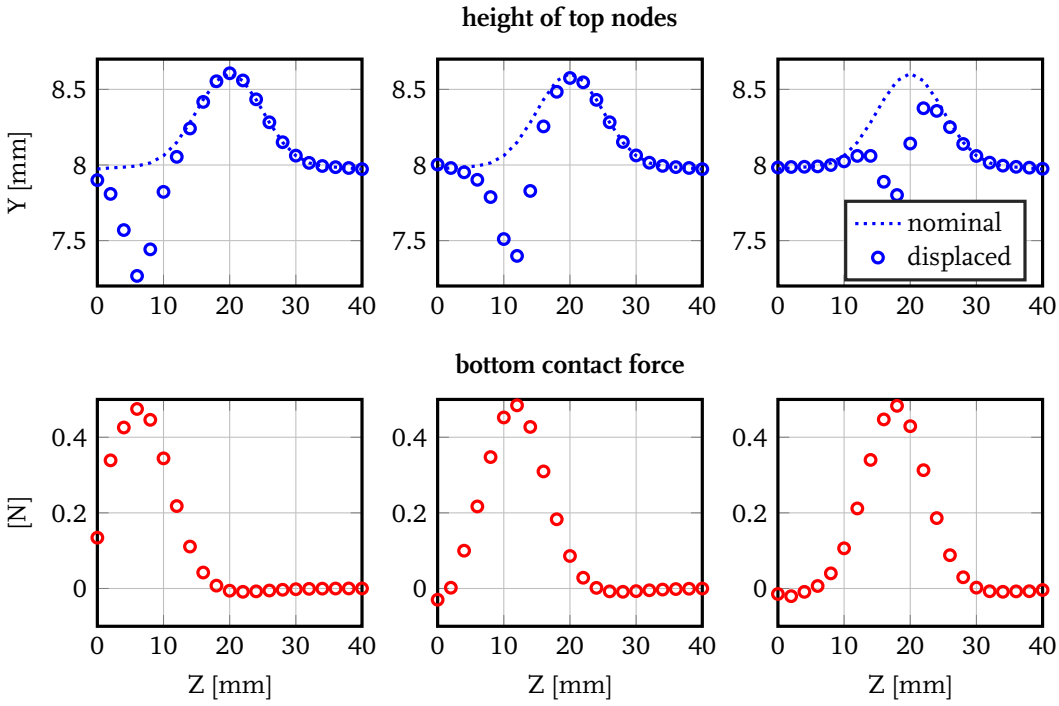

Figure 7.3: Displacement of top nodes and contact force on the bottom of the weatherstrip due to applicator force.

In Figure 7.3 three snapshots are shown of displacements of the middle nodes at the top of the weatherstrip and of the contact forces at the bottom of the weatherstrip. These nodes are located in the the $z-y$ plane at $x=0$. The nominal locations of the nodes are displayed the dashed line, which correspond to the situation when no force is applied to the weatherstrip. Under the application force, the nodes get displaced, which is displayed by the blue circles. It can be seen that while the applicator wheel moves over the weatherstrip, the nodes get pressed down and the contact force at the bottom of the weatherstrip increases.

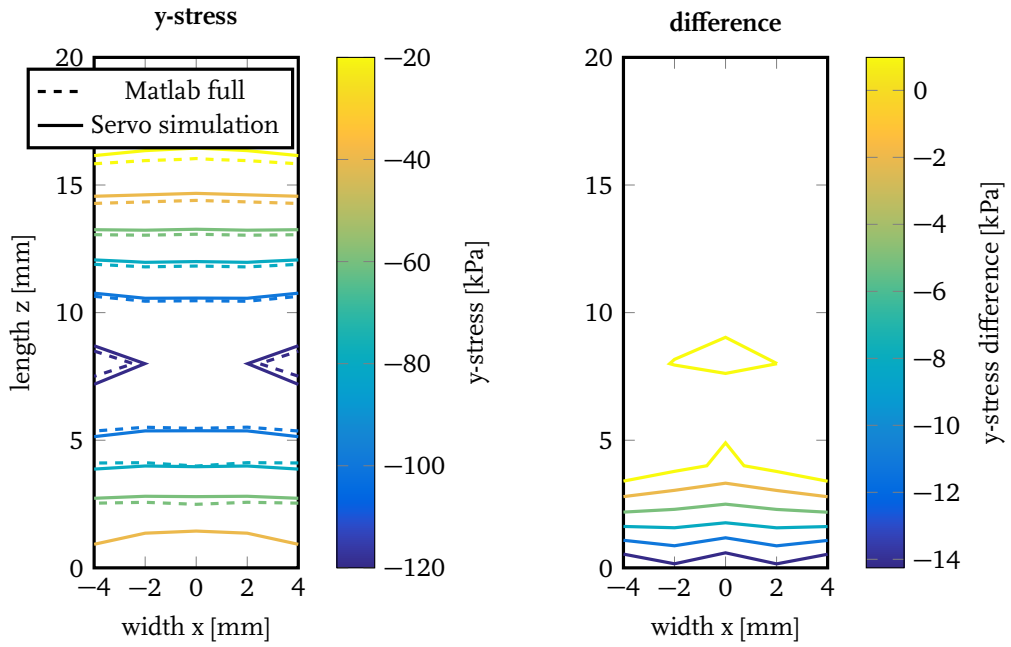

Figure 7.4: Stress distribution at the bottom of the weatherstrip: full Matlab model and servo simulated results on the left hand side and the difference between these two simulations on the right hand side.

The stress in the y-direction at the bottom of the strip is shown in Figure 7.4 for the case when the applicator wheel is located at $z=8$ mm, this is the same situation as shown in Figure 5.2 and in the subsequent figures showing the stress on the bottom of the weatherstrip. It can be seen that the stress distribution in the servo simulation including a six degrees of freedom robot, force interaction mapping and a reduced state-space model is similar to that of the full (static) Matlab simulation (Figure 5.2). The only differences are related to the force error shown in Figure 7.2.

Displacement in the x-direction at the bottom of the weatherstrip is shown in Figure 7.5. This figure shows the case where the applicator wheel is located at $z=8$ mm. This figure confirms the results shown in Figure 7.4, that is, the results of the servo simulation are similar to the results from a static computation with the full Matlab model.

7.5 Conclusion

The six-degree of freedom robot is implemented in Simulink and an inverse dynamics control law is implemented to be able to control the end-effector of the robot in the task space of the robot. The force controller described in Chapter 6 is used in the task space directions that need to be force-controlled.

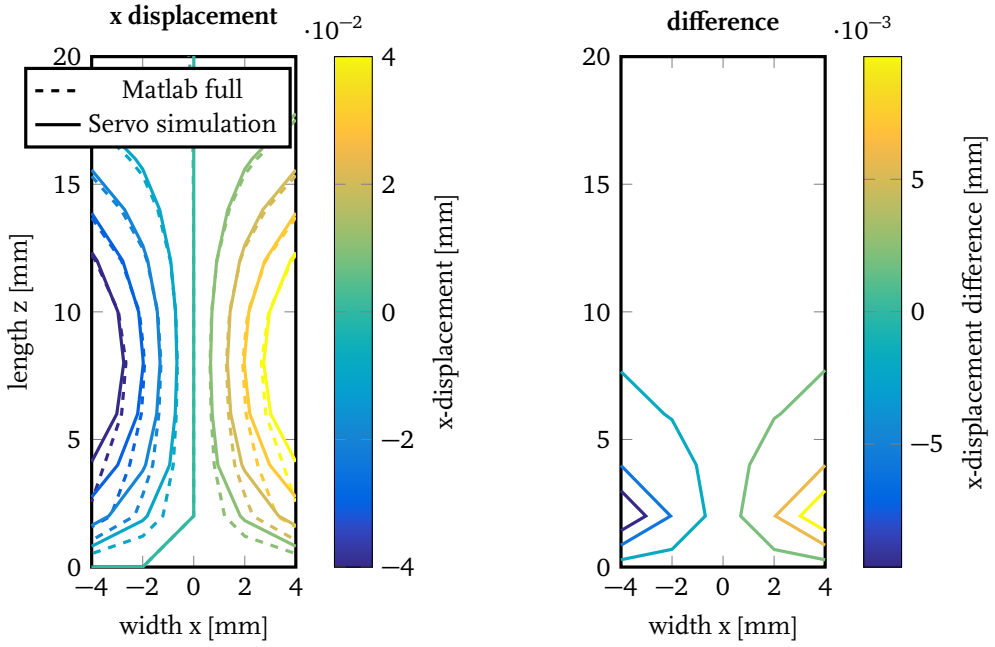

Figure 7.5: Displacement in the x-direction at the bottom of the weatherstrip: full Matlab model and servo simulated results on the left hand side and the difference between these two simulations on the right hand side.

In the other directions, PD controllers are used. A simulation of the force and motion controlled robot interacting with the state-space model of the weatherstrip is performed and the results show that the force controlled robot achieves the desired mounting force.

Chapter 8

Conclusions and Recommendations

8.1 Conclusion

In this project a model of a weatherstrip is made and used in conjunction with a model of a six degrees of freedom robot to design a control law that regulates the motion and application force on the weatherstrip. The goals of the project are stated in Section 1.2.

A literature study is performed to investigate different methods to quantify rubber behavior and gain knowledge about behavior of rubber materials that are not exhibited by other commonly used materials such as metals or ceramics. It is concluded that an *Ogden* hyperelastic model can be used to create a model of the weatherstrip, since this model captures phenomena that are relevant for the sealing task, such as a nonlinear stress-strain relationship, viscoelastic behavior and the Mullins effect. It is found that there is not a good agreement between three material models found in the literature for a simple uniaxial tension test.

A nonlinear finite element model is created and used to investigate how some effects present in rubber may influence the process of weatherstrip assembly. These effects are the nonlinear behavior, relaxation, creep and the Mullins effect. It is found that in the process of weatherstrip application where the loading rate and the stretch rate are relatively low, creep, relaxation and the Mullins effect can be disregarded. The effects of nonlinear behavior cannot be disregarded, since discrepancies are found between results form a tension simulation and a compression simulation that are performed in the scope of this project. For tension, it seems that a linear model can represent the behavior of the weatherstrip accurately enough, while a compression simulation shows that the nonlinear model predicts quite different results than the linear model. Unfortunately, the available models and material data are created from tension experiments reported in literature, so these are less reliable for compression simulations. This suggests that it would be instructive to experimentally verify the material model and its parameters that are used in this project. Preliminary results of such an experimental verification which is carried out in parallel to this project [59], show promising results, however, these results are not integrated in this project because of different time lines between the two projects.

Simulations with the finite element model of the weatherstrip show that a linear model has a good agreement with the nonlinear model with respect to effects of deformation and stress at the bottom of the weatherstrip. This indicates that a linear model can be used to capture the behavior of the weatherstrip during assembly.

The linear finite element model is exported to Matlab, where a linear state-space model is created from this finite element model. A model order reduction is performed on the state-space model to reduce the order of the model from several thousands of states to 250 states. The reduced order

state-space model is validated against the linear finite element model and good agreement is found.

A hybrid impedance force control law for the application force is designed for one degree of freedom. This control law regulates the interaction force between the applicator wheel and the weatherstrip and ensures that the desired mounting force is achieved. Evaluation of this controller shows that the controlled system is robust against parameter variations and is able to track the desired application force.

In Matlab, a six degrees of freedom robot is implemented including inertia properties from CAD data from the robot manufacturer. This robot model is functionally combined with the linear state-space model of the weatherstrip, including a force mapping which models the contact behavior between the applicator wheel and the weatherstrip. A linearizing inverse dynamics controller is implemented and combined with the hybrid impedance force controller designed for the 1DOF system. Time domain servo control simulations show low position and force errors, which implied that the controlled system performs satisfactory; the achieved application pressure and deformation at the bottom of the weatherstrip are within acceptable bounds.

8.2 Recommendations

The models of the robot and weatherstrip that are used in this project are not capable of representing the behavior of the weatherstrip making contact with the substrate. It is therefore recommended that a simulation is performed in a finite element software package as to also simulate the behavior of making contact with the substrate.

The rubber model used in this project is taken from the literature, and may not be a good characterization of the rubber material actually used. Experiments on weatherstrip specimens described in [59] show promising results in matching the adopted rubber model and actual weatherstrip behavior. It is advised that the material parameters extracted from these experiments are used to create a new finite element model and linear state-space model. Also, with these updated models that better describe the experimental behavior of weatherstrips, the control design can be optimized.

It is advised to perform an experiment where the applicator wheel is fitted with a force sensor and pressed onto the weatherstrip. The bottom of the weatherstrip could be mounted on a pressure sensing pad to measure the actual stress at the bottom of the strip. The linear state-space model and the force interaction mapping could be validated in this experiment.

To validate the force controller of the robot, the robot should be fitted with a force sensor between the last link of the robot and the applicator wheel. The robot should follow a predefined motion and force setpoint trajectories over a substrate of a known high stiffness. The results of this experiment could be used to evaluate performance of the robot force control.

In this project the mounting force that is needed for good adhesion of the weatherstrip onto the substrate is taken from the literature. It is not known how accurate this mounting force needs to be achieved for good adhesion, or how the minimum mounting force is influenced by the substrate material. It is recommended that an experiment is carried out to find the minimum force needed to realize a sufficient bonding between the weatherstrip and the substrate.

To mount the weatherstrip onto the substrate it is important to use the desired mounting force, however, it is also important that the weatherstrip is correctly aligned with the edges of the substrate surface. This requires position control of the applicator wheel and weatherstrip, but equally important, it also requires that the orientation of the weatherstrip is controlled such that it follows the (curved) edge of the substrate. Manually, this is achieved by positioning the free end of the weatherstrip along the edge of the weatherstrip, and using a certain tension force to keep the weatherstrip from bending under gravitational loads. A model should be designed which can capture the position and orientation of the weatherstrip under gravity and tension, this model should be validated by experiments and

be used to design a device that can automatically perform the task of orienting the weatherstrip and keeping the right amount of tension.

Lastly, it is recommended that a tool is designed to be used on the robot for mounting the weatherstrip onto a substrate. In addition, a tool has to be designed that supplies the robot with the weatherstrip. In this project it is assumed that the weatherstrip is available on the applicator wheel, but in reality a tool is needed to place it there.

Appendix A

ANSYS APDL Input Listings

A.1 Comparison of Different Nonlinear Models

In section 3.1 a comparison between different rubber material models is performed using a simulation of a uniaxial tension test. The listing below shows the ANSYS APDL code to run these simulations, Table A.1 depicts the used material parameters. The definitions of the material models can be found in Section 2.2.2.

Table A.1: Material parameters

model	parameter	parameter values		
		1	2	3
Arruda-Boyce	μ	3.34×10^{-2}		
Dikmen [22]	λ_L	9.74×10^{-1}		
Mooney-Rivlin	C_{10}	1.22×10^{-1}		
Dikmen [22]	C_{01}	-2.91×10^{-2}		
Ogden	μ	5.24×10^{-2}		
Dikmen [22]	α	5.08		
Ogden	μ_i	7.45×10^{2}	-2.39×10^{2}	-3.03×10^{-1}
Cheng [18]	α_i	-6.73×10^{-2}	-2.13×10^{-1}	-7.27
James-Green-Simpson	C_{10}	9.33×10^{-2}		
Wagner [63]	C_{01}	9.02×10^{-2}		
	C_{20}	6.37×10^{-3}		
	C_{11}	6.23×10^{-3}		
	C_{30}	3.32×10^{-4}		
Ogden	μ_i	4.40×10^{-1}	1.14	3.14
Wang [64]	α_i	2.09×10^{-7}	3.90	3.30×10^{-6}

```
!@ ==============================
!@ ---  Header ---
!@ ==============================
!! Time-stamp: <Thu Jan  8 10:20:50 2015>
!! ANSYS VERSION: 150
!! NOTE: Comparison between different material models for rubber

/COM %%% Element Definitions
```

```
/PREP7
ET,1,solid186                   ! 3d, 20 node

/COM %%% Geometry
Lz=10                           ! Length of specimen
Lx=7.5                          ! Width of specimen
Ly=1.6                          ! Height of specimen
EpMax = 1                       ! Maximum nominal Strain
DzMax = Lz*EpMax                ! Maximum displacement
A0 = Lx*Ly                      ! Original cross sectional area
BLOCK,0,Lx,0,Ly,0,Lz            ! Specimen

/COM %%% Materials
!@@@ -- 1: OGDEN: Cheng & Chen paper --
TB,HYPE,1,1,3,OGDE              ! Ogden material
TBTEMP,0
TBDATA,1,744.9711,-0.0673,-239.0485,-0.2128,-0.3031,-7.2684 !Material data from Cheng & Chen paper

!@@@ -- 2:James-Green-Simpson, Stenti & Wagner papers --
TB,HYPE,2,1,9,Mooney            ! 9-term Mooney-Rivlin material (James-Green-Simpson)
TBTEMP,0
TBDATA,1,0.0932811,0.0902353,0.0063716,0.0062266,0,0.0003316 !Material data from Stenti and Wagner

!@@@ -- 3: 3-term Ogden,Wang & Lee --
TB,HYPE,3,1,3,Ogden             ! 3-term Ogden
TBTEMP,0
TBDATA,1,0.4402,2.093e-5,1.139,3.898,3.1415,3.295e-6        !Material data from Wang, Lee (30% EPDM)

!@@@ -- 4: 2-term Mooney-Rivlin, Dikmen --
TB,HYPE,4,1,2,Mooney
TBTEMP,0
TBDATA,1,0.1220719,-0.029116    ! Material data from Dikmen

!@@@ -- 5: Arruda-Boyce, Dikmen
TB,HYPE,5,1,3,Boyce              ! Arruda-Boyce
TBTEMP,0
TBDATA,1,0.033379,0.9736532     ! Dikmen

!@@@ -- 6: 1-term Ogden, Dikmen
TB,HYPE,6,1,1,Ogden              ! 1-term Ogden
TBTEMP,0
TBDATA,1,0.0524,5.0802          ! Ogden, from Dikmen

/COM %%% Meshing
MSHKEY,1                        ! 1: mapped meshing,2: mapped if possible
MSHAPE,0,3d                     ! 0: quads/hex 1:tri/tets, dimensions: 2d/3d
ElemLength = Ly/3               ! Desired element edge length
ESIZE,ElemLength                ! element edge length
MAT,6                           ! Select material
VMESH,all                       ! Mesh all volumes

/COM %%% Boundary Conditions
NSEL,s,loc,z,0                  ! nodes at z=0
D,all,uz,0                      ! constrain in z-dir
NSEL,r,loc,x,0                  ! nodes at z=0 & x=0
D,all,ux,0                      ! Constrain also in x dir
NSEL,all                        ! Select all nodes
NSEL,s,loc,z,0                  ! select z=0 nodes
NSEL,r,loc,y,0                  ! nodes at z=0 & y=0
D,all,uy,0                      ! Constrain in y dir
NSEL,all
```

```
/COM %%% Displacements
NSEL,s,loc,z,Lz                 ! nodes at z=Lz
D,all,uz,DzMax                  ! Displacement load
NSEL,all

/COM %%% Solution
/SOLU
ALLSEL
SOLCONTROL,on                   ! optimised nonlinear solution defaults
N1=15                           ! No of substeps for the first one
N2=50                           ! maximum No of substeps
N3=10                           ! minimum No of substeps
NSUBST,N1,N2,N3
OUTRES,all,all
ANTYPE,static                   ! static simulation
NLGEOM,on
AUTOTS,on
SOLVE

/COM %%% Output
/POST26
NUMVAR,200                      ! maximum No of variables, 1 is always time

/COM %%% Get nodal results
NSEL,s,loc,z,Lz                 ! Nodes at end
NSEL,r,loc,x,Lx                 ! Nodes at end and side
NSEL,r,loc,y,Ly                 ! Node at top side end
*GET,nodnum,node,,num,max       ! Get number of node at top side end

/COM %%% First order results
NSOL,2,nodnum,U,Z,UZ_edge       ! Z displacement
NSOL,3,nodnum,U,X,UX_edge       ! X displacement
NSOL,4,nodnum,U,Y,UY_edge       ! Y displacement
ANSOL,5,nodnum,S,Z,ZStress      ! Stress in z-direction: Sz

/COM %%% Static Values
FILLDATA,11,,,,Lz               ! orig Z location of node
FILLDATA,12,,,,Lx               ! orig X location of node
FILLDATA,13,,,,Ly               ! orig Y location of node
FILLDATA,14,,,,A0               ! Original Area : A0

/COM %%% First order Calculations
ADD,21,2,11,,Lz2                ! New Z location (length)
ADD,22,3,12,,Lx2                ! New X location (width)
ADD,23,4,13,,Ly2                ! New Y location (height)

/COM %%% Second order Calculations
QUOT,31,21,11,,Stretch          ! Stretch: Lambda=L1/L0
PROD,32,22,23,,AR               ! real Area: A

/COM %%% Third order Calculations
PROD,41,5,32,,ZForceAr          ! Force in Z direction with real Area: FZA

/COM %%% Fourth order Calculations
QUOT,51,41,14,,NomStress        ! Nominal stress (based on orig A0)

/COM %%% PLOTTEN
XVAR,31                         ! Stretch on x-axis
/AXLAB,X,Stretch                ! Set X-axis label
/AXLAB,Y,Nominal Stress         ! Set Y-axis label
PLVAR,51
```

```
/COM %%% Save output to file
*GET,Size,VARI,,NSETS           ! No of datapoints
*DIM,Time,array,Size
*DIM,Stretch,array,Size
*DIM,NomStress,array,Size
VGET,Time(1),1                  ! put time into array
VGET,Stretch(1),31              ! put stretch into array
VGET,NomStress(1),51            ! put Nominal Stress into array
!! - export arrays -
*CREATE,tmp,mac
*CFOPEN,sim,txt
Strg='Time Stretch NomStress'
*VWRITE,Strg
%S
*VWRITE,Time(1), Stretch(1), NomStress(1)
%G %G %G
*CFCLOS
*END
*LIST,tmp,mac
/INPUT,tmp,mac
*LIST,sim,txt
```

A.2 Mullins Effect

The ANSYS APDL listing for the simulation shown in Section 3.1.4 is shown below. A 3-term Ogden model is used, as defined in equation (2.11). The Mullins effect is modeled using the Ogden-Roxburgh model where the damage variable is given by equation (2.27). The material parameters used are given in Table A.2.

Table A.2: Material parameters for 3-term Ogden model with Mullins effect

	parameter values		
parameter	1	2	3
μ_i	7.45×10^{2}	-2.39×10^{2}	-3.03×10^{-1}
α_i	-6.73×10^{-2}	-2.13×10^{-1}	-7.27
m		9.77×10^{-1}	
r		2.06	

The ANSYS APDL input listing for the Mullins effect simulation is almost identical to the listing in Section A.1, only the differences are shown (material and load case definition):

```
/COM %%% Materials
!@@@ -- 1: OGDEN: Cheng & Chen paper --
TB,HYPE,1,1,3,OGDE
TBTEMP,0
TBDATA,,744.9711,-0.0673,-239.0485,-0.2128,-0.3031,-7.2684
TBDATA,,0,0,0,,,
! Mullins effect (pseudo elastic: pse2)
TB,CDM,1,,3,pse2
TBDATA,1,2.062,0.9773,0

/COM %%% Displacement Loads
dz1=5
dz2=10
```

```
dz3=15
dz4=20

/COM %%% Load cases
/COM %%% Load case 1
NSEL,s,loc,z,Lz
D,all,UZ,dz1
NSEL,all
SOLVE

NSEL,s,loc,z,Lz
D,all,UZ,0
NSEL,all
SOLVE

/COM %%% Load case 2
NSEL,s,loc,z,Lz
D,all,UZ,dz2
NSEL,all
SOLVE

NSEL,s,loc,z,Lz
D,all,UZ,0
NSEL,all
SOLVE

/COM %%% Load case 3
NSEL,s,loc,z,Lz
D,all,UZ,dz3
NSEL,all
SOLVE

NSEL,s,loc,z,Lz
D,all,UZ,0
NSEL,all
SOLVE

/COM %%% Load case 4
NSEL,s,loc,z,Lz
D,all,UZ,dz4
NSEL,all
SOLVE

NSEL,s,loc,z,Lz
D,all,UZ,0
NSEL,all
SOLVE
```

A.3 Stretch Rate

The material data for the 3-term Ogden model used in the simulation of the influence of stretch rate is given in Table A.3.

The ANSYS APDL input listing for the stretch rate simulation is almost identical to the listing in Section A.1, the differences are shown below:

```
/COM %%% Materials
!@@@ -- 1: Low Rate: 0.004/s -  OGDEN: Cheng & Chen paper --
```

Table A.3: Material parameters for 3-term Ogden model for low and high stretch rates

		parameter values		
	parameter	1	2	3
low rate	μ_i	7.45×10^{2}	-2.39×10^{2}	-3.03×10^{-1}
$0.004\ s^{-1}$	α_i	-6.73×10^{-2}	-2.13×10^{-1}	-7.27
high rate	μ_i	1.89×10^{2}	-1.06×10^{3}	-4.99×10^{-2}
$3000\ s^{-1}$	α_i	-5.28×10^{-1}	-9.55×10^{-2}	-1.19×10^{1}

```
TB,HYPE,1,1,3,OGDE              !Ogden material
TBTEMP,0
TBDATA,1,744.9711,-0.0673,-239.0485,-0.2128,-0.3031,-7.2684
!@@@ -- 1: High Rate: 3000/s -  OGDEN: Cheng & Chen paper --
TB,HYPE,2,1,3,OGDE
TBTEMP,0
TBDATA,1,188.6373,-0.5281,-1061.0986,-0.09549,-0.049922,-11.9074
```

A.4 Visco-Hyperelastic Model

The material data for the combined 3-term Ogden and 3-term Prony series model used in the relaxation simulation in Section 3.2.2 is given in Table A.4.

Table A.4: Material parameters for the combined 3-term Ogden and 3-term Prony series model for visco-hyperelastic behavior

		parameter values		
	parameter	1	2	3
Ogden	μ_i	7.45×10^{2}	-2.39×10^{2}	-3.03×10^{-1}
	α_i	-6.73×10^{-2}	-2.13×10^{-1}	-7.27
Prony series	τ_i	8×10^{-2}	1×10^{-2}	1×10^{-3}
	α_i	1.47×10^{-1}	1.47×10^{-1}	3.10×10^{-1}

The ANSYS APDL input listing for the relaxation simulation is almost identical to the listing in Section A.1, the differences are shown below:

```
/COM %%% Materials
!@@@ Material parameters
!@@@ -- 1: OGDEN: Cheng & Chen paper --
TB,HYPE,1,1,3,OGDE              ! Ogden material
TBTEMP,0
TBDATA,1,744.9711,-0.0673,-239.0485,-0.2128,-0.3031,-7.2684 !Material data from Cheng & Chen paper

!@@@ -- 2: Visco elastic behavior:
tau1 = 80.0000e-003             ! Time constants
tau2 = 10.0000e-003
tau3 =  1.0000e-003
alpha1 = 146.8744e-003
alpha2 = 147.4608e-003
alpha3 = 310.2230e-003

!@@@ -- 3: Material data input
```

```
!@@@ Prony series, from Olsson paper
TB,PRONY,1,1,3,shear
TBTEMP,0
TBDATA,1,alpha1,tau1,alpha2,tau2,alpha3,tau3
```

A.5 Weatherstrip Simulation

The code listing below shows the ANSYS APDL code used to simulate the weatherstrip assembly process as shown in Chapter 4. In the material definition section it is possible to select linear or nonlinear material by commenting and uncommenting the right parts of the code.

```
/COM %%% File name
fname ='Wheel_Force_Frict'
/FILNAME,fname,on               ! Set jobname

!@@@ -- Units
/UNITS,mpa                      ! indicate unit system

/COM %%% Element Definitions
/PREP7
R,1                             ! Real constant set for rubber
ET,1,solid185                   ! 3d, 8 node

/COM %%% Geometry
!@@@ -- Define constants
Lz = 20                         ! Length of specimen
Lx = 4                          ! Width of specimen
Ly = 4                          ! Height of specimen
R1 = Ly                         ! Radius of circular bulb on top of strip
Rw = 10                         ! Radius wheel
Lw = 2*(Lx+1)                   ! Length wheel (must be longer than strip)
Pxw = Lx+1                      ! Position of wheel in x-direction (width of strip)
Pzw = 2*Lx                      ! Position of wheel in z-direction (length of strip)
Gapw = 0                        ! Gap between strip and wheel
Pyw = Ly+R1+Rw+Gapw             ! Position of wheel in y-direction (height of strip)
Fw = 10                         ! Force on wheel

!@@@ -- 1: Rubber
BLOCK,-Lx,Lx,0,Ly,0,Lz          ! Specimen
CYL4,0,Ly,R1,0,,180,Lz          ! Circular bulb on top of strip
VADD,all                        ! Add all volumes together
VSEL,s,loc,x,0,Lx               ! Select Rubber Block, to create component
CM,RubberStrip,volu             ! Create volume component: RubberStrip
ALLSEL

!@@@ -- 2: Bottom Strip
ASEL,s,loc,y,0                  ! Select bottom of strip
CM,BottomStrip,area             ! Create component
ALLSEL

!@@@@ -- Unify areas on back and front of strip for sweep meshing
ASEL,s,loc,z,0                  ! Select back face of strip
AADD,all                        ! Create single area
*GET,BackAreaNum,area,,num,min  ! Number of area for sweep mesh
ALLSEL
ASEL,s,loc,z,Lz                 ! Select front face of strip
AADD,all                        ! Create single area
```

```
*GET,FrontAreaNum,area,,num,min ! Number of area for sweep mesh
ALLSEL

!@@@ -- Rigid Floor
K,,-Lx-1,0,-1
K,,Lx+1,0,-1
K,,Lx+1,0,Lz+1
K,,-Lx-1,0,Lz+1
*GET,BottomKPnum,kp,,num,max    ! Get maximum Keypoint
A,BottomKPnum-3,BottomKPnum-2,BottomKPnum-1,BottomKPnum ! Generate Area
KSEL,s,kp,,BottomKPnum
LSLK,s,0
ASLL,s,0                        ! Select floor
CM,Floor,area                   ! Create component
ALLSEL

/COM %%% Materials
!@@@ -- 1: Low Rate: 0.004/s -  OGDEN: Cheng & Chen paper --
TB,HYPE,1,1,3,OGDE              ! Ogden material
TBTEMP,0
TBDATA,1,744.9711,-0.0673,-239.0485,-0.2128,-0.3031,-7.2684
MPTEMP,1,0
MPDATA,mu,1,,3.5                ! Static friction coefficient
!! !@@@ -- Linear Material
!! MPTEMP,1,0
!! MPDATA,ex,1,,3.46            ! E-modulus (fit) [N/mm^2]
!! MPDATA,prxy,1,,0.4999        ! Poisson's ratio (incompressible)
!! MPDATA,dens,1,,1.08e-6       ! From Freudenberg EPDM datasheet (1.08 g/cm3)
!! MPDATA,mu,1,,0               ! Static friction coefficient

/COM %%% Meshing
!@@@ -- 1: Rubber strip
MSHKEY,0                        ! 1: mapped meshing,2: mapped if possible
MSHAPE,0,3d                     ! 0: quads/hex 1:tri/tets, dimensions: 2d/3d
ElemLength = Lx/4               ! Desired element edge length
ESIZE,ElemLength                ! element edge length
MAT,1                           ! Select material
REAL,1                          ! Real constant set
CMSEL,s,RubberStrip             ! Select rubber strip
VSWEEP,all,BackAreaNum,FrontAreaNum     ! Mesh all volumes
ALLSEL

/COM %%% Boundary Conditions
NSEL,s,loc,z,0                  ! nodes at z=0
D,all,uz,0                      ! constrain in z-dir
NSEL,s,loc,z,0                  ! select z=0 nodes
NSEL,r,loc,y,0                  ! nodes at z=0 & y=0
D,all,uy,0                      ! Constrain in y dir
NSEL,all
NSEL,s,loc,z,0                  ! Nodes at z=0
NSEL,r,loc,x,0                  ! Nodes at x=0
D,all,ux,0                      ! Constrain in x-dir
ALLSEL

/COM %%% Element Definitions
/PREP7
!@@@ -- Contact
*GET,et,etyp,,num,max           ! get maximum element type
Contact = et+1                  ! Element number for contact
Target = Contact+1              ! Target element number
R,Contact                       ! Real constant set
ET,Contact,conta173             ! 3D Contact element
```

```
ET,Target,targe170              ! 3D Target element
!@@@ -- Keyoptions
KEYOPT,Contact,5,1              ! Set keyopt 5 to close the gap

!@@@ -- Contact 2
Contact2 = Target+1
Target2 = Contact2+1
R,Contact2
ET,Contact2,conta173
ET,Target2,targe170

!@@@@ -- Top area of rubber strip for contact meshing
ASEL,s,loc,y,Ly,Ly+R1           ! Select areas within top part of strip
ASEL,r,loc,z,1e-4,Lz-1e-4       ! Only select top face
CM,TopStrip,area                ! Area component
ALLSEL

!@@@ -- 2: Wheel
WPOFFS,-Pxw
WPROTA,0,0,90                   ! Rotate working plane
CYL4,-Pzw,Pyw,Rw,240,,300,Lw    ! Cylinder (x,y,radius1,theta1,radius2,theta2,length)
VSEL,s,loc,y,Pyw-Rw,Pyw,,1      ! Select wheel only (volumes and below)
ASEL,r,loc,y,Pyw-Rw,Pyw-Rw/1.5  ! Select cylinder faces
CM,Wheel,area                   ! Create Area component: Wheel
ALLSEL
WPCSYS,1,0                      ! Align working plane with global coordinate system

!@@@ -- : Rigid Wheel and contact
MSHAPE,0,2d                     ! 2D quad meshing
ESIZE,ElemLength                ! desired element length
TYPE,Contact                    ! Element type: Contact
REAL,Contact                    ! Real Constant set

!@@@@ -- Contact on rubber strip
CMSEL,s,TopStrip                ! Select top area
NSLA,s,1                        ! Select nodes in area
ESURF                           ! Create surface Contact elements
ALLSEL

!@@@@ -- Target on cylinder surface
TYPE,Target                     ! Set target elements
CMSEL,s,Wheel                   ! Select bottom surface of wheel
MSHKEY,0
TSHAP,quad                      ! Target shape: 4 node quadrilateral
AMESH,all                       ! Mesh surface
ALLSEL

!@@@@ -- Pilot node
TSHAP,pilo                      ! Set Pilot node
CMSEL,s,Wheel                   ! Select wheel
LSLA,s                          ! Select lines in wheel
KSLL,s                          ! Select keypoints on lines
*GET,PilotKP,kp,,num,min        ! Number of a keypoint
KMESH,PilotKP                   ! Mesh pilot node
ALLSEL

!@@@ Bottom strip contact
MSHAPE,0,2d
ESIZE,ElemLength
TYPE,Contact2
REAL,Contact2
!@@@@ Bottom Strip
```

```
CMSEL,s,BottomStrip             ! Select bottom of strip
NSLA,s,1                        ! Select nodes in bottom
ESURF                           ! Create surface contact
ALLSEL
!@@@@ Floor
TYPE,Target2
CMSEL,s,Floor                   ! Select floor area
MSHKEY,0
TSHAP,quad
AMESH,all
NSLA,s,1                        ! Select all nodes within this area
ESLN,s
ESURF,,reverse
ALLSEL

!@@@ Constrain Wheel
KSEL,s,kp,,PilotKP              ! Select pilot keypoint
NSLK,s                          ! Select pilot node
D,all,ux,0,,,,uz,rotx,roty,rotz ! Constrain pilot node
ALLSEL

/COM %%% Solution
/SOLU
ALLSEL
SOLCONTROL,on                   ! optimised nonlinear solution defaults
OUTRES,basic,all                ! Results to write
ANTYPE,static                   ! static simulation
NLGEOM,on                       ! on for hyperelastic, off for linear elastic

!@@@ -- 1: First load step: wheel pressure: Force
KSEL,s,kp,,PilotKP
NSLK,s                          ! Select node connected to pilot node
F,all,FY,-Fw                    ! Compression Force due to wheel
ALLSEL
NSUBST,25,50,10                 ! Substeps
SOLVE
```

A.6 Modal Analysis in ANSYS

In ANSYS a modal analysis can be carried out to find the eigenmodes and eigenvectors of a linear model; a model with linear material parameters and approximately linear (small) displacements. To be able to export the stiffness and mass matrices of a system to a text file, is is needed to set up a model analysis and then export the generated system matrices. In the listing below the APDL code to do this is shown.

```
!@@@@ -- Write out node mapping
CMSEL,s,RubberStrip             ! Select strip only
NSLV,s,1                        ! Select nodes in strip
ESLN,s                          ! Select elements in strip
EWRITE,'Lin_SI_elem','list'     ! output element list
NWRITE,'Lin_SI_node','list'     ! output node list
ALLSEL

!! @ ==============================
!! @ ---  Solution ---
!! @ ==============================
```

```
/COM %%% Solution
!@@@ -- modal analysis: constraint modes and constraint mass and stiffness matrices
/SOLU
ANTYPE,modal
MODOPT,lanb,20,0,1e4            ! method,No of modes,freqB,freqE
MXPAND
SOLVE
FINISH

!@ ==============================
!@ --- Output Frequencies ---
!@ ==============================
/COM %%% Put natural frequencies in file
/POST1                          ! Postprocessor
/OUTPUT,'Lin_SI_Freqlist','txt'
SET,list                        ! Put results in file
/OUTPUT

!@ ==============================
!@ --- Output to MODAL Matrices ---
!@ ==============================
/AUX2
FILE,fname,'full'               ! Set filename of FULL file
HBMAT,'Lin_SI_STIFF_free','matrix',,ASCII,stiff,yes,yes     ! output stiffness matrix and mapping file
HBMAT,'Lin_SI_MASS_free','matrix',,ASCII,mass,yes           ! output mass matrix
FINISH
```

Appendix B

Fitting Viscoelastic Parameters

The authors of [45] performed dynamical experiments on different types of rubber, the results of the experiment on EPDM rubber is shown in Figure B.1. Here the dotted line with the diamond markings represents an experiment with an excitation amplitude of 6.7 %. While the authors of this paper also fitted a material model to this experimental data, this model is unfortunately not usable in this context. Therefore it is needed to create a custom fit for the Prony series described in Section 2.2.4

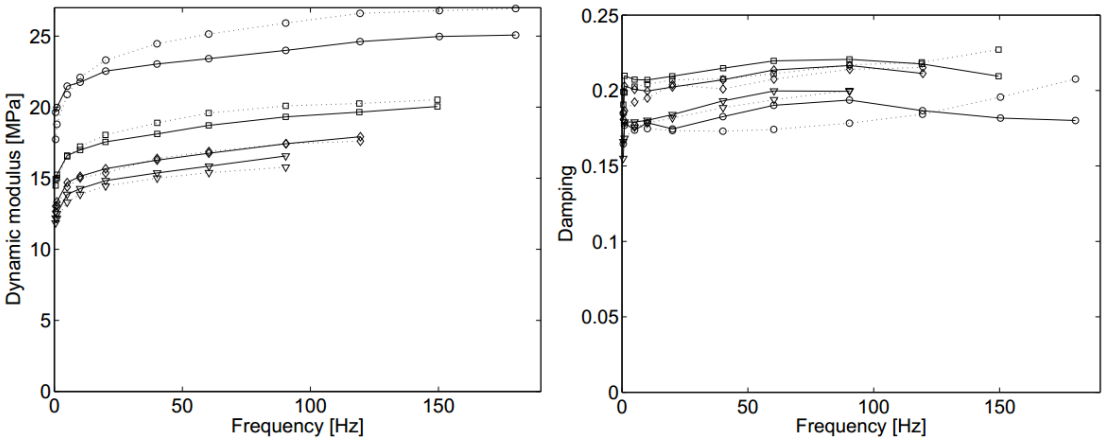

Figure B.1: Dynamic shear modulus and damping for EPDM rubber, the dotted lines depict experimental data and the solid lines depict a material model. The different markings represent data from experiments with different excitation amplitudes [45].

The data from the experiment with an excitation amplitude of 6.7 % is extracted from the figure, to be used for curve fitting. This data is chosen over the other sources because it has the highest excitation amplitude in this set.

The dynamic modulus and damping extracted from Figure B.1 can be used to fit a Prony series viscoelastic model. The general form of a Prony series viscoelastic model is given by Equation 2.18:

$$g(t) = g_\infty + \sum_{i=1}^{m} g_i e^{\frac{-t}{\tau_i}}$$

In this model, time constants τ_i and moduli g_∞ and g_i need to be determined. In this case, this can

be done by using the Laplace transform of the storage and loss modulus [46]:

$$G'(\omega) = G_\infty + \sum_{i=1}^{m} \frac{\omega^2 \tau_i^2 G_i}{\omega^2 \tau_i^2 + 1} \tag{B.1}$$

$$G''(\omega) = \sum_{i=1}^{m} \frac{\omega \tau_i G_i}{\omega^2 \tau_i^2 + 1} \tag{B.2}$$

Where the storage and loss moduli are given by [50]:

$$G^* = G' + iG'' \tag{B.3}$$

$$G^* = G_{\text{dyn}} + e^{i\delta} \tag{B.4}$$

$$d = \sin(\delta) \tag{B.5}$$

Here, the dynamic modulus $G_{\mathbf{dyn}}$ and damping d are extracted from Figure B.1.

Values for G_∞ and G_i in equations (B.1) and (B.2) are fitted to the extracted storage and loss moduli G' and G'' respectively with a nonnegative least-squares procedure. A range of frequencies ω corresponding to Figure B.1, and chosen values for the time constants τ_i are used in this procedure. This results in the parameters shown in Table B.1:

Table B.1: Prony series parameters

time constant τ_i [s]	modulus G_i [MPa]	relative modulus α_i [-]
8.0×10^{-2}	3.383	1.469×10^{-1}
1.0×10^{-2}	3.397	1.475×10^{-1}
1.0×10^{-3}	7.145	3.102×10^{-1}
∞	9.108	3.954×10^{-1}

The row in Table B.1 with a time constant of ∞ corresponds to the equilibrium modulus G_∞. In the third column, the relative moduli α_i are given, they are defined by:

$$\alpha_i = \frac{G_i}{G_0} \tag{B.6}$$

$$G_0 = G_\infty + \sum_{i=1}^{m} G_i \tag{B.7}$$

The resulting curves for the dynamic modulus and damping, depending on frequency are depicted in Figure B.2. From this figure it can be seen that the fitted parameters result in a satisfactory approximation of the measured data.

The parameters for the relative moduli α_i in Table B.1 can be used in ANSYS to create a viscoelastic model or a visco-hyperelastic model. A viscoelastic model in ANSYS is modeled in the same way as the prony series viscoelastic model of Equation (2.18):

$$G(t) = G_0 \left(\alpha_\infty + \sum_{i=1}^{m} \alpha_i e^{\frac{-t}{\tau_i}} \right) \tag{B.8}$$

The visco-hyperelastic model from equation (2.22) can be used together with the α_i values to combine the visco-elastic behavior with a hyperelastic material model:

$$\boldsymbol{P} = \int_0^t \left(\alpha_\infty + \sum_{i=1}^{m} \alpha_i e^{-\frac{t-\tau}{\tau_i}} \right) 2 \frac{\mathrm{d}}{\mathrm{d}\tau} \frac{\partial W}{\partial \boldsymbol{C}} \mathrm{d}\tau$$

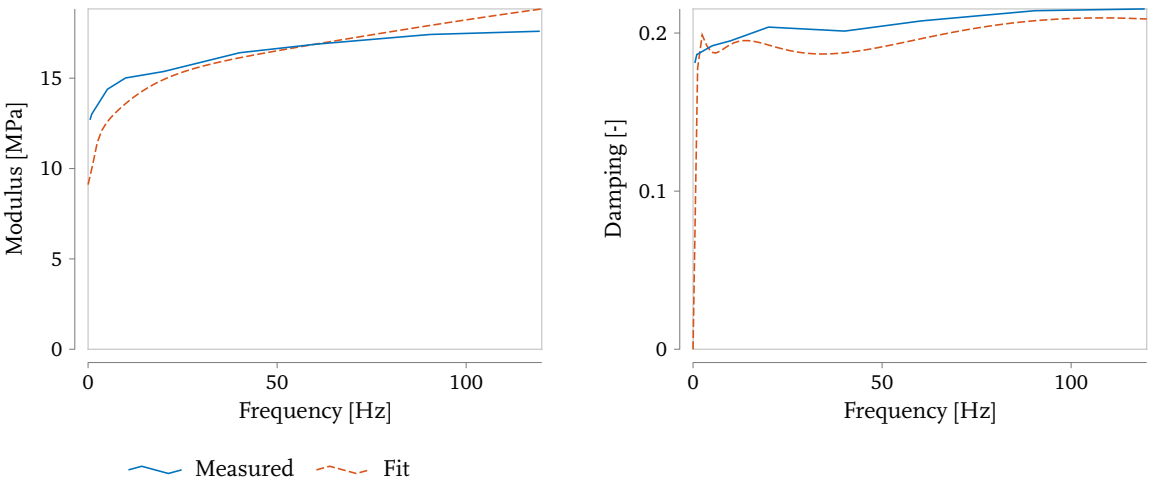

Figure B.2: Dynamic modulus and damping, for measured [45] and fitted data

Appendix C

Friction Simulation

When applying the weatherstrip to the substrate, friction will occur between the bottom of the weatherstrip and the substrate due to normal forces from the applicator wheel. In ANSYS this friction is incorporated with a Coulomb friction model:

$$\tau_{\text{lim}} = \mu P + b \tag{C.1}$$

where τ_{lim} is the maximum shear stress before slippage occurs, μ is the friction coefficient, P is the normal contact pressure and b is a static cohesion which is not used in these simulations. For the friction coefficient between EPDM rubber and glass a value of 3.5[-] is used [51].

Figure C.1 shows the stress in the global y-direction on the bottom of the weatherstrip. This is the stress needed to bond the weatherstrip to the substrate, for a good bond this stress needs to exceed 100 kPa. In the left figure, the results of the simulation with friction are shown, the middle figure shows the results of a simulation without friction and the right figure shows the difference between the two simulations. In both simulations the stress in the bottom is high enough to guarantee a good bond. From the right figure it can be seen that the difference in stress is small in a large area directly under the applicator wheel (around 8 mm in the length direction), and becomes higher near the edges. From these figures the conclusion can be drawn that for the stress on the bottom of the weatherstrip the inclusion of friction in the model does not have an adverse effect, so on the basis of this simulation, it is not needed to include friction in the model.

In Figure C.2 the displacement in global x-direction (width) is shown for a simulation with (left) and without (middle) friction. The right figure shows the difference between the two simulations. The left figure shows that the friction between the weatherstrip and the substrate severely impacts the displacement on the bottom. The simulation with friction predicts a maximum displacement of 6×10^{-4} mm, whereas the simulation without friction shows a maximum displacement of 3×10^{-2} mm. The large difference between the two simulations would indicate that friction is an important phenomenon in this process, however, the total displacement without friction is already so small that it permits disregarding the friction effect altogether.

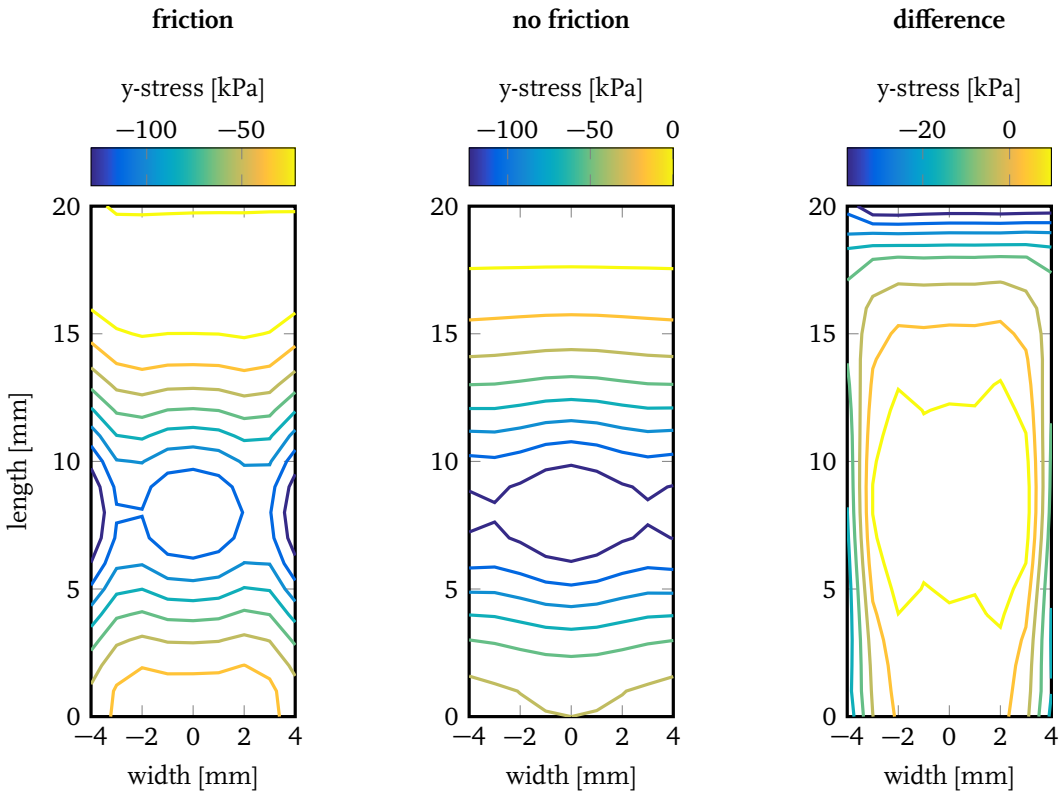

Figure C.1: Stress in global y-direction on bottom of weatherstrip simulated with a hyperelastic material model. Friction between bottom of strip and substrate on the left, no friction in the middle and the difference on the right.

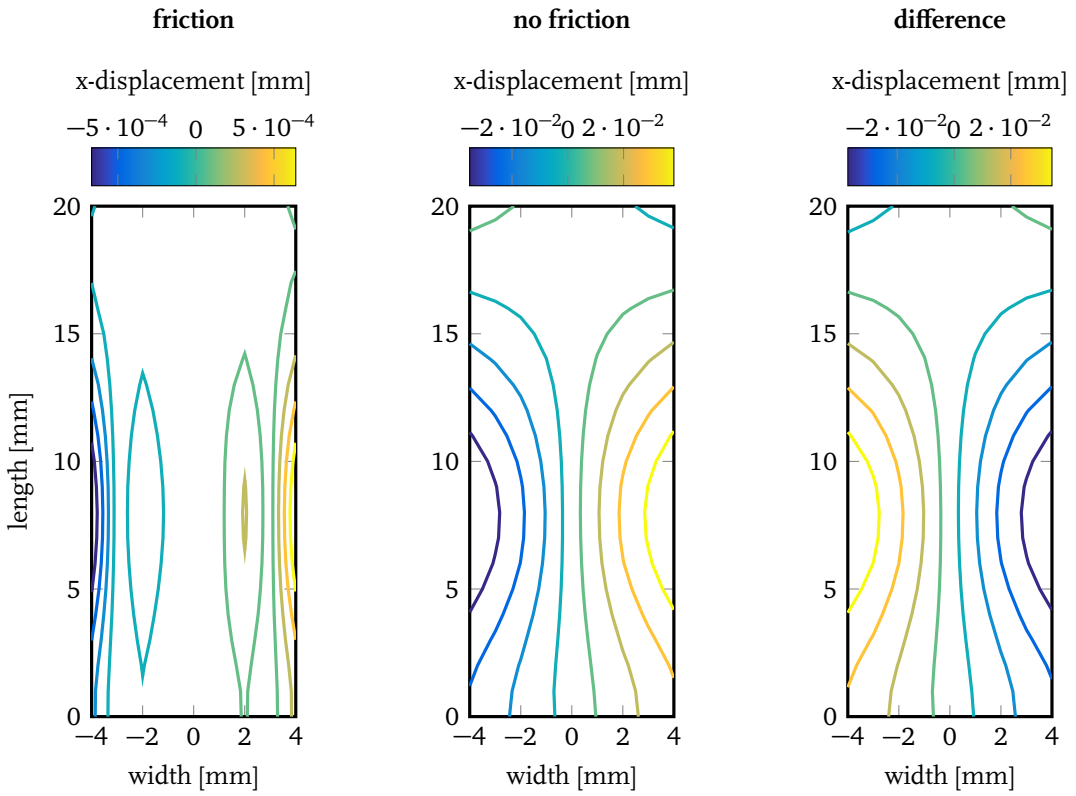

Figure C.2: Displacement in x-direction on bottom of weatherstrip simulated with a hyperelastic material model. Friction between bottom of strip and substrate on the left, no friction in the middle and the difference on the right.

Appendix D

Compare Eigenvalues of Reduction Methods

The natural frequencies of the full model, as described in Section 5.1.6 are compared with the natural frequencies of the Craig-Bampton reduced model (described in Section 5.2) and with the balanced truncation reduced model (described in Section 5.3.1). The results of this comparison can be seen in Table D.1, here the first column shows the mode number, the second column shows the natural frequency of that mode for the full model. The third column shows the relative natural frequency of the Craig-Bampton reduced model with respect to the full model. The last column shows the relative natural frequency of the balanced truncation reduced model with respect to the full model.

It can be concluded from this table that all models show good agreement for modes below 2400 Hz. It can be concluded that these models therefore can be used for servo simulations of the weatherstrip assembly process.

Table D.1: Eigenvalues for different reduced models

mode number	f_i full model [Hz]	full/CB [-]	full/BT [-]
1	42.35	1.000	1.000
2	214.53	1.000	1.000
3	352.82	1.000	1.000
4	456.80	1.000	1.000
5	757.28	1.000	1.000
6	1021.30	0.998	0.998
7	1141.70	0.999	0.999
8	1462.50	0.996	0.996
9	1532.90	0.966	0.966
10	1581.60	0.994	0.994
11	1609.80	0.996	0.996
12	1663.80	0.980	0.980
13	1747.40	0.987	0.987
14	1836.10	0.941	0.941
15	1921.40	0.959	0.959
16	1946.90	0.955	0.955
17	1992.20	0.959	0.959
18	2064.40	0.942	0.942
19	2079.00	0.909	0.909
20	2132.80	0.924	0.924
21	2208.80	0.920	0.920
22	2333.00	0.915	0.915
23	2391.90	0.922	0.922
24	2478.30	0.886	0.886
25	2479.60	0.883	0.883
26	2490.20	0.793	0.793
27	2524.50	0.785	0.785
28	2681.40	0.810	0.810
29	2682.00	0.786	0.786
30	2798.60	0.796	0.796

Appendix E

Robot Parameters

The SimMechanics visualisation of the ABB IRB 2400 robot used in this project is shown in Figure E.1. The inertial parameters of the robot are given in Table E.1

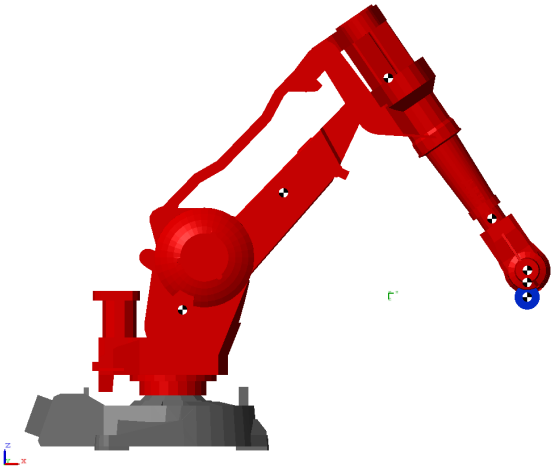

Figure E.1: ABB IRB 2400 Robot

Table E.1: ABB IRB 2400 parameters

link	parameter		parameter values		
1	m	[kg]	150		
	r	[m]	−0.070	0.17	0.019
	I	[kg m^2]	7.6	1.0	0.30
			1.0	5.8	−0.10
			0.30	−0.10	5
2	m	[kg]	47		
	r	[m]	−0.38	0.037	−0.0027
	I	[kg m^2]	0.38	0.094	0.0027
			0.094	2.0	−0.025
			0.0027	−0.025	2.1
3	m	[kg]	40		
	r	[m]	−0.019	0.010	−0.0011
	I	[kg m^2]	0.93	−0.010	−0.053
			−0.010	0.91	0.011
			−0.053	0.011	0.32
4	m	[kg]	18		
	r	[m]	0.000 30	−0.20	0.0010
	I	[kg m^2]	0.52	−0.000 38	-4.3×10^{-5}
			−0.000 38	0.044	−0.0036
			-4.3×10^{-5}	−0.0036	0.51
5	m	[kg]	0.97		
	r	[m]	0.000 96	4×10^{-7}	−0.000 19
	I	[kg m^2]	0.000 85	0	6.9×10^{-6}
			0	0.0014	-2.8×10^{-8}
			6.9×10^{-6}	-2.8×10^{-8}	0.000 91
6	m	[kg]	0.57		
	r	[m]	-9.1×10^{-5}	-9×10^{-7}	−0.047
	I	[kg m^2]	0.000 47	0	10.0×10^{-7}
			0	0.000 47	0
			10.0×10^{-7}	0	6.2×10^{-5}

Bibliography

[1] 3M. *Surface Preparation for 3M VHB Tape Applications*. Apr. 2007. url: http://solutions.3m.com/3MContentRetrievalAPI/BlobServlet?lmd=1257319648000&locale=en_IN&assetType=MMM_Image&assetId=1180621382599&blobAttribute=ImageFile.

[2] A. Stenti, D. Moens, and W. Desmet. *Dynamic modeling of car door weather seals: A first outline*. 2004. url: http://www-04.mech.kuleuven.be/publications/PMA_MOD_publications/ISMA2004/1249_1262.pdf.

[3] ABB. *IRB 2400 CAD - IRB 2400 (Industrial Robots - Robotics) | ABB*. url: http://new.abb.com/products/robotics/industrial-robots/irb-2400/irb-2400-cad.

[4] ANSYS. *ANSYS Mechanical APDL Material Reference*. 2014.

[5] ANSYS. *ANSYS Mechanical APDL Theory Reference*. 2014.

[6] ANSYS. "Advanced Analysis with ANSYS". 2002. url: http://ansys.net/papers/nonlinear/conflong_hyperel.pdf.

[7] A. F. M. S Amin, M. S Alam, and Y Okui. "An improved hyperelasticity relation in modeling viscoelasticity response of natural and high damping rubbers in compression: experiments, parameter identification and numerical verification". In: *Mechanics of Materials* 34.2 (Feb. 2002), pp. 75–95. url: http://www.sciencedirect.com/science/article/pii/S0167663601001028.

[8] A. F. M. S. Amin et al. "Nonlinear dependence of viscosity in modeling the rate-dependent response of natural and high damping rubbers in compression and shear: Experimental identification and numerical verification". In: *International Journal of Plasticity* 22.9 (Sept. 2006), pp. 1610–1657. url: http://www.sciencedirect.com/science/article/pii/S0749641905001658.

[9] "Apparatus of a robot for installing weather stripping in a door or like opening". Pat. 4760636. Stephen Angelo St. Jr. et al. Feb. 8, 1988. url: http://www.freepatentsonline.com/4760636.html.

[10] Ellen M. Arruda and Mary C. Boyce. "A three-dimensional constitutive model for the large stretch behavior of rubber elastic materials". In: *Journal of the Mechanics and Physics of Solids* 41.2 (Feb. 1993), pp. 389–412. url: http://www.sciencedirect.com/science/article/pii/0022509693900136.

[11] Jonathan Baake. *Mechatronics development of a Z-Force Module for die bonding*. Eindhoven, 2014. url: http://www.tue.nl/en/publication/ep/p/d/ep-uid/418039/.

[12] I. Basdogan and E. Dikmen. "Modeling Viscoelastic Response of Vehicle Door Seal". In: *Experimental Techniques* 35.3 (May 1, 2011), pp. 29–35. url: http://onlinelibrary.wiley.com/doi/10.1111/j.1747-1567.2009.00599.x/abstract.

[13] J. S. Bergström and M. C. Boyce. "Constitutive modeling of the large strain time-dependent behavior of elastomers". In: *Journal of the Mechanics and Physics of Solids* 46.5 (May 1998), pp. 931–954. url: http://www.sciencedirect.com/science/article/pii/S0022509697000756.

[14] B. Besselink et al. "A comparison of model reduction techniques from structural dynamics, numerical mathematics and systems and control". In: *Journal of Sound and Vibration* 332.19 (Sept. 16, 2013), pp. 4403–4422. url: http://www.sciencedirect.com/science/article/pii/S0022460X1300285X.

[15] Javier Bonet and Richard D Wood. *Nonlinear continuum mechanics for finite element analysis*. Cambridge; New York, NY, USA: Cambridge University Press, 1997. url: http://researchbooks.org/0521838703.

[16] Jan F. Broenink and Martin L. J. Tiernego. *Peg-in-Hole assembly using Impedance Control with a 6 DOF Robot*. Simulation in Industry. Genoa, Italy: Society for Computer Simulation International (SCS), Oct. 24, 1996. url: http://www.ce.utwente.nl/bnk/papers/ess96.pdf.

[17] S. Cantournet, R. Desmorat, and J. Besson. "Mullins effect and cyclic stress softening of filled elastomers by internal sliding and friction thermodynamics model". In: *International Journal of Solids and Structures* 46.11–12 (June 1, 2009), pp. 2255–2264. url: http://www.sciencedirect.com/science/article/pii/S0020768309000080.

[18] Ming Cheng and Weinong Chen. "Experimental investigation of the stress-stretch behavior of EPDM rubber with loading rate effects". In: *International Journal of Solids and Structures* 40.18 (Sept. 2003), pp. 4749–4768. url: http://www.sciencedirect.com/science/article/pii/S0020768303001823.

[19] A. Dall'Asta and L. Ragni. "Nonlinear behavior of dynamic systems with high damping rubber devices". In: *Engineering Structures* 30.12 (Dec. 2008), pp. 3610–3618. url: http://www.sciencedirect.com/science/article/pii/S0141029608002174.

[20] Julie Diani, Mathias Brieu, and Pierre Gilormini. "Observation and modeling of the anisotropic visco-hyperelastic behavior of a rubberlike material". In: *International Journal of Solids and Structures* 43.10 (May 2006), pp. 3044–3056. url: http://www.sciencedirect.com/science/article/pii/S0020768305003811.

[21] Julie Diani, Bruno Fayolle, and Pierre Gilormini. "A review on the Mullins effect". In: *European Polymer Journal* 45.3 (Mar. 2009), pp. 601–612. url: http://www.sciencedirect.com/science/article/pii/S0014305708006332.

[22] E. Dikmen and I. Basdogan. "Material characteristics of a vehicle door seal and its effect on vehicle vibrations". In: *Vehicle System Dynamics* 46.11 (Aug. 28, 2008), pp. 975–990. url: http://dx.doi.org/10.1080/00423110701689610.

[23] A. Dorfmann and R. W. Ogden. "A constitutive model for the Mullins effect with permanent set in particle-reinforced rubber". In: *International Journal of Solids and Structures* 41.7 (Apr. 2004), pp. 1855–1878. url: http://www.sciencedirect.com/science/article/pii/S0020768303006504.

[24] Fredrik Karlsson and Anders Persson. "Modelling Non-Linear Dynamics of Rubber Bushings - Parameter Identification and Validation". Lund, Sweden: Lund University, Division of Structural Mechanics, 2003. url: http://www.byggmek.lth.se/fileadmin/byggnadsmekanik/publications/tvsm5000/web5119.pdf.

[25] Mir Hamid Reza Ghoreishy. "Determination of the parameters of the Prony series in hyper-viscoelastic material models using the finite element method". In: *Materials & Design*. New Rubber Materials, Test Methods and Processes 35 (Mar. 2012), pp. 791–797. url: http://www.sciencedirect.com/science/article/pii/S0261306911004523.

[26] N. Gil-Negrete, J. Viñolas, and L. Kari. "A simplified methodology to predict the dynamic stiffness of carbon-black filled rubber isolators using a finite element code". In: *Journal of Sound and Vibration* 296.4–5 (Oct. 10, 2006), pp. 757–776. url: http://www.sciencedirect.com/science/article/pii/S0022460X06002732.

[27] Michael R. Hatch. *Vibration Simulation Using MATLAB and ANSYS*. 1 edition. New York: Chapman and Hall/CRC, Sept. 21, 2000.

[28] Impact Engineering. *ANSYS USers Group: Hyperelastic Materials*. url: http://ansys.net/papers/ANSYS_Users_Group_Hyperelastic_Materials.pdf.

[29] John Mortimer. "BMW lifts robot total to 500 at Plant Oxford". In: *Assembly Automation* 28.1 (Feb. 22, 2008), pp. 27–35. url: http://www.emeraldinsight.com.dianus.libr.tue.nl/doi/full/10.1108/01445150810848984.

[30] H. Khajehsaeid et al. "A visco-hyperelastic constitutive model for rubber-like materials: A rate-dependent relaxation time scheme". In: *International Journal of Engineering Science* 79 (June 2014), pp. 44–58. url: http://www.sciencedirect.com/science/article/pii/S0020722514000561.

[31] Beomkeun Kim et al. "A comparison among Neo-Hookean model, Mooney-Rivlin model, and Ogden model for chloroprene rubber". In: *International Journal of Precision Engineering and Manufacturing* 13.5 (May 1, 2012), pp. 759–764. url: http://link.springer.com/article/10.1007/s12541-012-0099-y.

[32] Bram de Kraker and Dick H. van Campen. *Mechanical vibrations*. Maastricht: Shaker, 2001.

[33] A. Lion and C. Kardelky. "The Payne effect in finite viscoelasticity: constitutive modelling based on fractional derivatives and intrinsic time scales". In: *International Journal of Plasticity* 20.7 (July 2004), pp. 1313–1345. url: http://www.sciencedirect.com/science/article/pii/S0749641903001360.

[34] Alexander Lion. "A constitutive model for carbon black filled rubber: Experimental investigations and mathematical representation". In: *Continuum Mechanics and Thermodynamics* 8.3 (June 1, 1996), pp. 153–169. url: http://link.springer.com/article/10.1007/BF01181853.

[35] MATLAB. *Control Systems Toolbox*. Natick, Massachusetts: The Mathworks Inc.

[36] MATLAB. *version 8.5 (R2015a)*. Natick, Massachusetts: The Mathworks Inc.

[37] MSC Software. *Nonlinear Finite Element Analysis of Elastomers*. Nonlinear Finite Element Analysis of Elastomers. url: http://www.mscsoftware.com/sites/default/files/wp_elastomer_ltr_w_0.pdf.

[38] G. Marckmann and E. Verron. "Comparison of Hyperelastic Models for Rubber-Like Materials". In: *Rubber Chemistry and Technology* 79.5 (Nov/Dec 2006), pp. 835–858. url: http://search.proquest.com.dianus.libr.tue.nl/docview/220690872/citation/978104818416460EPQ/1?accountid=27128.

[39] "Method and device for attaching sealing profiles". Pat. US8398808 B2. Klaus Grohmann, Lothar Thommes, and Martin Weinandy. Mar. 19, 2013. url: http://www.google.nl/patents/US8398808.

[40] "Method for fitting a sealing strip to a flange of a sliding-roof opening or similar body openings and device for carrying out such a method." Pat. EP0857599 B1. Helmuth Pöschl and Josef Rehmböck. Oct. 17, 2001. url: http://www.google.nl/patents/EP0857599B1.

[41] "Method of applying weatherstrip to a vehicle body opening". Pat. 4620354. Edward C. Hess and Charles J. Anglewicz. Apr. 11, 1986. url: http://www.freepatentsonline.com/4620354.html.

[42] G. Michalos et al. "Automotive assembly technologies review: challenges and outlook for a flexible and adaptive approach". In: *CIRP Journal of Manufacturing Science and Technology* 2.2 (2010), pp. 81–91. url: http://www.sciencedirect.com/science/article/pii/S1755581709000467.

[43] D. Mundo, P. Mas, and D. Clausi. "Dynamic characterization and numerical modelling of automotive rubber connections". In: *Proceedings of the Institution of Mechanical Engineers, Part D: Journal of Automobile Engineering* 220.4 (Apr. 1, 2006), pp. 425–434. url: http://pid.sagepub.com/content/220/4/425.

[44] R. W. Ogden and D. G. Roxburgh. "A Pseudo-Elastic Model for the Mullins Effect in Filled Rubber". In: *Proceedings: Mathematical, Physical and Engineering Sciences* 455.1988 (Aug. 8, 1999), pp. 2861–2877. url: http://www.jstor.org.dianus.libr.tue.nl/stable/53461.

[45] Anders K. Olsson. "Finite Element Procedures in Modelling the Dynamic Properties of Rubber". In: (2007). url: http://www.lunduniversity.lu.se/lup/publication/548298.

[46] S. W. Park. "Analytical modeling of viscoelastic dampers for structural and vibration control". In: *International Journal of Solids and Structures* 38.44–45 (Nov. 2001), pp. 8065–8092. url: http://www.sciencedirect.com/science/article/pii/S0020768301000269.

[47] Per-Erik Austrell. "Finite Element Analysis of Elastomers". Malmö, Apr. 9, 2014. url: http://www.sgf.se/wp-content/uploads/Finite-Element-Analysis-of-Elastomers.pdf.

[48] "Robot for installing weather stripping in a door or like opening". Pat. US5029381 A. Stephen St Angelo Jr et al. July 9, 1991. url: http://www.google.com/patents/US5029381.

[49] Lynn Rogers. "Operators and Fractional Derivatives for Viscoelastic Constitutive Equations". In: *Journal of Rheology (1978-present)* 27.4 (Aug. 1, 1983), pp. 351–372. url: http://scitation.aip.org.dianus.libr.tue.nl/content/sor/journal/jor2/27/4/10.1122/1.549710.

[50] Schreurs, Piet. *Computational Material Models, lecture notes*. June 16, 2014. url: http://www.mate.tue.nl/~piet/edu/cmm/pdf/cmmsyl1314.pdf.

[51] Schulman. *Coefficients of friction*. url: http://www.apainfo.com/docs/tech-notes/alcryn-coefficient-of-friction.pdf?sfvrsn=12.

[52] Jane Shi and Roland Menassa. "Flexible Robotic Assembly in Dynamic Environments". In: *Proceedings of the 10th Performance Metrics for Intelligent Systems Workshop*. PerMIS '10. New York, NY, USA: ACM, 2010, pp. 271–276. url: http://doi.acm.org/10.1145/2377576.2377626.

[53] J. C. Simo. "On a fully three-dimensional finite-strain viscoelastic damage model: Formulation and computational aspects". In: *Computer Methods in Applied Mechanics and Engineering* 60.2 (Feb. 1987), pp. 153–173. url: http://www.sciencedirect.com/science/article/pii/0045782587901071.

[54] Mark W. Spong, Seth Hutchinson, and M. Vidyasagar. *Robot modeling and control*. Hoboken, NJ: John Wiley & Sons, 2006.

[55] Paul Steinmann, Mokarram Hossain, and Gunnar Possart. "Hyperelastic models for rubber-like materials: consistent tangent operators and suitability for Treloar's data". In: *Archive of Applied Mechanics* 82.9 (Sept. 1, 2012), pp. 1183–1217. url: http://link.springer.com.dianus.libr.tue.nl/article/10.1007/s00419-012-0610-z.

[56] A. Stenti et al. "A three-level non-deterministic modeling methodology for the NVH behavior of rubber connections". In: *Journal of Sound and Vibration* 329.7 (Mar. 29, 2010), pp. 912–930. url: http://www.sciencedirect.com/science/article/pii/S0022460X09008116.

[57] A. Stenti et al. "Low-frequency dynamic analysis of automotive door weather-strip seals". In: *Mechanical Systems and Signal Processing* 22.5 (July 2008), pp. 1248–1260. url: http://www.sciencedirect.com/science/article/pii/S0888327007002579.

[58] Andrea Stenti et al. "Development of a numerical modelling methodology for the NVH behaviour of elastomeric line connections". In: *International Conference on Noise and Vibration Engineering*. 2006. url: http://www.isma-isaac.be/publications/PMA_MOD_publications/ISMA2006/157_168.pdf.

[59] William Thijssen. *Building a Material Model of a Rubber Weatherstrip, internship report*. 2015.

[60] M. J. García Tárrago et al. "Torsion stiffness of a rubber bushing: A simple engineering design formula including the amplitude dependence". In: *The Journal of Strain Analysis for Engineering Design* 42.1 (Jan. 1, 2007), pp. 13–21. url: http://sdj.sagepub.com.dianus.libr.tue.nl/content/42/1/13.

[61] Bertram J. Unger et al. "Comparison of 3-D haptic peg-in-hole tasks in real and virtual environments". In: *Intelligent Robots and Systems, 2001. Proceedings. 2001 IEEE/RSJ International Conference on*. Vol. 3. IEEE, 2001, pp. 1751–1756. url: http://www.msl.ri.cmu.edu/publications/pdfs/iros01_hap.pdf.

[62] Luigi Villani and Joris De Schutter. "Force Control". In: *Springer Handbook of Robotics*. Ed. by Bruno Siciliano Prof and Oussama Khatib Prof. Springer Berlin Heidelberg, Jan. 1, 2008, pp. 161–185. url: http://link.springer.com.dianus.libr.tue.nl/referenceworkentry/10.1007/978-3-540-30301-5_8.

[63] David A. Wagner et al. "Nonlinear analysis of automotive door weatherstrip seals". In: *Finite Elements in Analysis and Design* 28.1 (Dec. 1, 1997), pp. 33–50. url: http://www.sciencedirect.com/science/article/pii/S0168874X97819610.

[64] Jin Jang Wang et al. "An experimental study and finite element analysis of weatherstrip". In: *International Journal of Precision Engineering and Manufacturing* 12.1 (2011), pp. 97–104. url: http://link.springer.com/article/10.1007%2Fs12541-011-0012-0?LI=true.

[65] M. L. Williams. "Structural analysis of viscoelastic materials". In: *AIAA Journal* 2.5 (1964), pp. 785–808. url: http://dx.doi.org/10.2514/3.2447.

[66] Yanchun Xia, Yuehong Yin, and Zhaoneng Chen. "Dynamic analysis for peg-in-hole assembly with contact deformation". In: *The International Journal of Advanced Manufacturing Technology* 30.1-2 (Aug. 1, 2006), pp. 118–128. url: http://link.springer.com/article/10.1007/s00170-005-0047-4.